

# Petrology and Nd–Hf Isotope Geochemistry of the Neoproterozoic Amon Kimberlite Sills, Baffin Island (Canada): Evidence for Deep Mantle Magmatic Activity Linked to Supercontinent Cycles

SEBASTIAN TAPPE<sup>1,2\*</sup>, BRUCE A. KJARSGAARD<sup>3</sup>,  
STEPHAN KURSZLAUKIS<sup>4</sup>, GEOFF M. NOWELL<sup>5</sup> AND  
DAVID PHILLIPS<sup>6</sup>

<sup>1</sup>DE BEERS GROUP EXPLORATION, PRIVATE BAG X01, JOHANNESBURG, GAUTENG 2135, SOUTH AFRICA

<sup>2</sup>SCHOOL OF GEOSCIENCES, UNIVERSITY OF THE WITWATERSRAND, PRIVATE BAG 3, JOHANNESBURG, GAUTENG 2050, SOUTH AFRICA

<sup>3</sup>GEOLOGICAL SURVEY OF CANADA, 601 BOOTH STREET, OTTAWA, ON K1A 0E8, CANADA

<sup>4</sup>DE BEERS CANADA INC., 250 FERRAND DRIVE, SUITE 900, TORONTO, ON M3C 3G8, CANADA

<sup>5</sup>DEPARTMENT OF EARTH SCIENCES, DURHAM UNIVERSITY, SOUTH ROAD, DURHAM DH1 3LE, UK

<sup>6</sup>SCHOOL OF EARTH SCIENCES, UNIVERSITY OF MELBOURNE, CNR SWANSTON–ELGIN STREETS, MCCOY BUILDING, PARKVILLE, VIC. 3010, AUSTRALIA

RECEIVED MARCH 27, 2014; ACCEPTED AUGUST 11, 2014

*The c. 673 Ma (U–Pb rutile) Amon kimberlites located in northern Baffin Island intruded Late Archean basement rocks of the Rae craton as a subhorizontal sill complex. The Amon sills are part of widespread low-volume, volatile-rich ultramafic magmatism that occurred along the northern and eastern margins of Laurentia, demarcating the temporal and spatial breakout from the Rodinia supercontinent during the Late Neoproterozoic. Numerous other known kimberlite occurrences that are related to these rifting events between c. 680 and 540 Ma are located in mainland Nunavut, Ontario, Quebec, Labrador, and West Greenland. The magmas that fed the Amon sills are archetypal Group-I kimberlites, based on groundmass mineralogy (e.g. phlogopite, spinel, ilmenite) and bulk-rock compositions, including moderately depleted Sr–Nd–Hf isotope ratios. However, a wide compositional range, together with observed flowage textures, indicates that some magma differentiation occurred during sill emplacement. The Amon samples that are*

*interpreted as parental kimberlite magma compositions overlap published compositions of experimentally derived, near-solidus partial melts of carbonated peridotite between 5 and 10 GPa; that is, equivalent to an origin from 150 to 300 km depth. Furthermore, the Amon kimberlites are characterized by moderately depleted Nd ( $\epsilon_{Nd(i)} = +1.5$  to  $+3.5$ ) and Hf ( $\epsilon_{Hf(i)} = +1.1$  to  $+8.7$ ) isotope compositions, without pronounced isotope decoupling as known from other kimberlite occurrences worldwide. Among the studied Late Neoproterozoic volatile-rich ultramafic magmatic rocks in Laurentia, the Amon kimberlites have Nd–Hf isotope systematics that are similar to those of a previously identified, carbonate-rich, depleted end-member component. This common component is suggested to represent a widespread near-solidus partial melt of volatile-fluxed fertile peridotite within the uppermost convecting mantle beneath the rifting supercraton. Our preferred model for Late Neoproterozoic kimberlite and related magmatism along the rifted*

\*Corresponding author. Telephone: +27-11-3746618. Fax: +27-11-3093140. E-mail: sebastian.tappe@debeersgroup.com

© The Author 2014. Published by Oxford University Press. All rights reserved. For Permissions, please e-mail: journals.permissions@oup.com

*margins of Laurentia invokes a combination of redox- and decompression-related low-degree partial melting of convecting upper mantle material that flows beneath rugged topography at the base of thick continental lithosphere. Provided that carbonate metasomatism of lower cratonic mantle is ubiquitous on a global scale, we argue that proto-kimberlitic melt is likely to be constantly present beneath the cratonic roots of supercontinents, and that it is most efficiently extracted during fast and changing plate motions, such as during the assembly and break-up of supercontinents. This idea is supported by the known kimberlite emplacement patterns of the Gondwana–Pangea (510 Ma–Recent) and Rodinia (1300–550 Ma) supercontinent cycles, but it remains difficult to test for older kimberlites and related rocks dating back to c. 3 Ga.*

KEY WORDS: kimberlite magma origin; Nd–Hf isotope systematics; plates versus plumes; Rodinia supercontinent break-up; U–Pb rutile geochronology

## INTRODUCTION

The origin of kimberlite magmatism has been explained in many ways (see Mitchell, 1995, for summary) and among the most popular mechanisms are plume-related processes involving deep cratonic mantle melting in response to the passage of continental plates over thermochemical upwellings, or hotspots (Crough *et al.*, 1980; England & Houseman, 1984; Le Roex, 1986; Heaman & Kjarsgaard, 2000; Collerson *et al.*, 2010). More recently, the utilization of comprehensive geochronology databases for regional (Heaman *et al.*, 2004; Jelsma *et al.*, 2004; Moore *et al.*, 2008) and global (Kumar *et al.*, 2007; Jelsma *et al.*, 2009) kimberlite and related magmatism has shown an apparent episodicity of deep-seated melting events, and it has been suggested that this magmatism is related to particular stages in the life cycle of supercontinents (Jelsma *et al.*, 2009) (Fig. 1a). In detail, Jelsma and co-workers demonstrated that during the Phanerozoic narrow kimberlite emplacement windows correspond to periods of fundamental plate reorganization associated with the assembly and break-up of the Gondwana superterrane (see also Torsvik & Cocks, 2013). The ‘Gondwana kimberlite pattern’ was recently extended to include new Cretaceous kimberlite discoveries from East Antarctica, which formed during incipient rifting processes associated with the opening of the proto-Indian Ocean at c. 120 Ma (Yaxley *et al.*, 2013).

Although there now exists a large body of evidence that Phanerozoic kimberlite and related magmatism was to some degree a response to major plate reorganizations, our understanding of the geodynamic conditions under which kimberlite magma formed during the Precambrian is rudimentary at best. The oldest known kimberlitic rocks date back to c. 2 Ga, and potentially there exist examples as old as 3 Ga (e.g. Bizzarro *et al.*, 2002) (Fig. 1a), but it is uncertain whether large continental lithospheric plates

existed by that time (Shirey & Richardson, 2011; Ernst *et al.*, 2013). Moreover, detrital diamonds of mantle derivation are known from Late Archean sedimentary successions (Stachel *et al.*, 2006; Gurney *et al.*, 2010; Kopylova *et al.*, 2011), suggesting that kimberlitic magmatism *sensu lato* occurred as early as the Mesoarchean. However, this inference is difficult to reconcile with the modelled higher ambient mantle temperatures during the Mesoarchean (Herzberg *et al.*, 2010), because in theory a much hotter than present-day thermal regime hampers low-degree, volatile-rich ultramafic melt production (Arndt, 2003).

Commonly, there exists a divide between studies that are devoted to the tectonic significance of kimberlite magmatism and those that aim at unravelling the kimberlite magma source evolution and melt formation using petrological and geochemical data. This general lack of integration of results from various research directions during the study of kimberlite magmatism has resulted in genetic models that consider kimberlites as highly unusual and difficult to explain, irrespective of the fact that over 5000 worldwide kimberlite occurrences are known to date. For example, mantle plume models without active zones of rifting do not account for the extremely low melt volumes that are produced by kimberlite magmatism (e.g. Torsvik *et al.*, 2010). On the other hand, geochemical models that invoke extremely trace element enriched mantle peridotite source regions (e.g. Le Roex *et al.*, 2003) disregard the fact that mineral–melt trace element partitioning in the presence of CO<sub>2</sub> (e.g. Brey *et al.*, 2008; Dasgupta *et al.*, 2009) is capable of producing incompatible element enriched ultramafic melts from ‘normal’ fertile peridotite by volatile fluxing (Tappe *et al.*, 2011, 2013a).

In this study, we report the first results on the geochronology, mineralogy, and geochemistry of the Amon Kimberlite Sill Complex (AKSC) in north-central Baffin Island (Fig. 2). The AKSC formed at the northern margin of the Laurentia supercraton within the Rodinia supercontinent during the Late Neoproterozoic. We use these data to constrain the kimberlite melt source region(s), as well as to unravel the melting process and magma evolution. The petrogenetic model for the c. 673 Ma Amon kimberlites is integrated into an existing petrological framework for the deep-seated, volatile-rich, ultramafic magmatism that occurred across eastern Laurentia (Tappe *et al.*, 2011, and references therein). Late Neoproterozoic kimberlite magmatism, which affected the northern and eastern breakout margins of Laurentia for their almost entire 3000 km combined length (Fig. 2), is utilized to further develop a plate-tectonic model of deep kimberlite magmatism operational since at least the latest Precambrian. This observation from Laurentia, together with the fact that global kimberlite and related magmatic activity increased substantially after Rodinia had reached its maximum stability and extent at c. 900 Ma (Fig. 1b), suggests

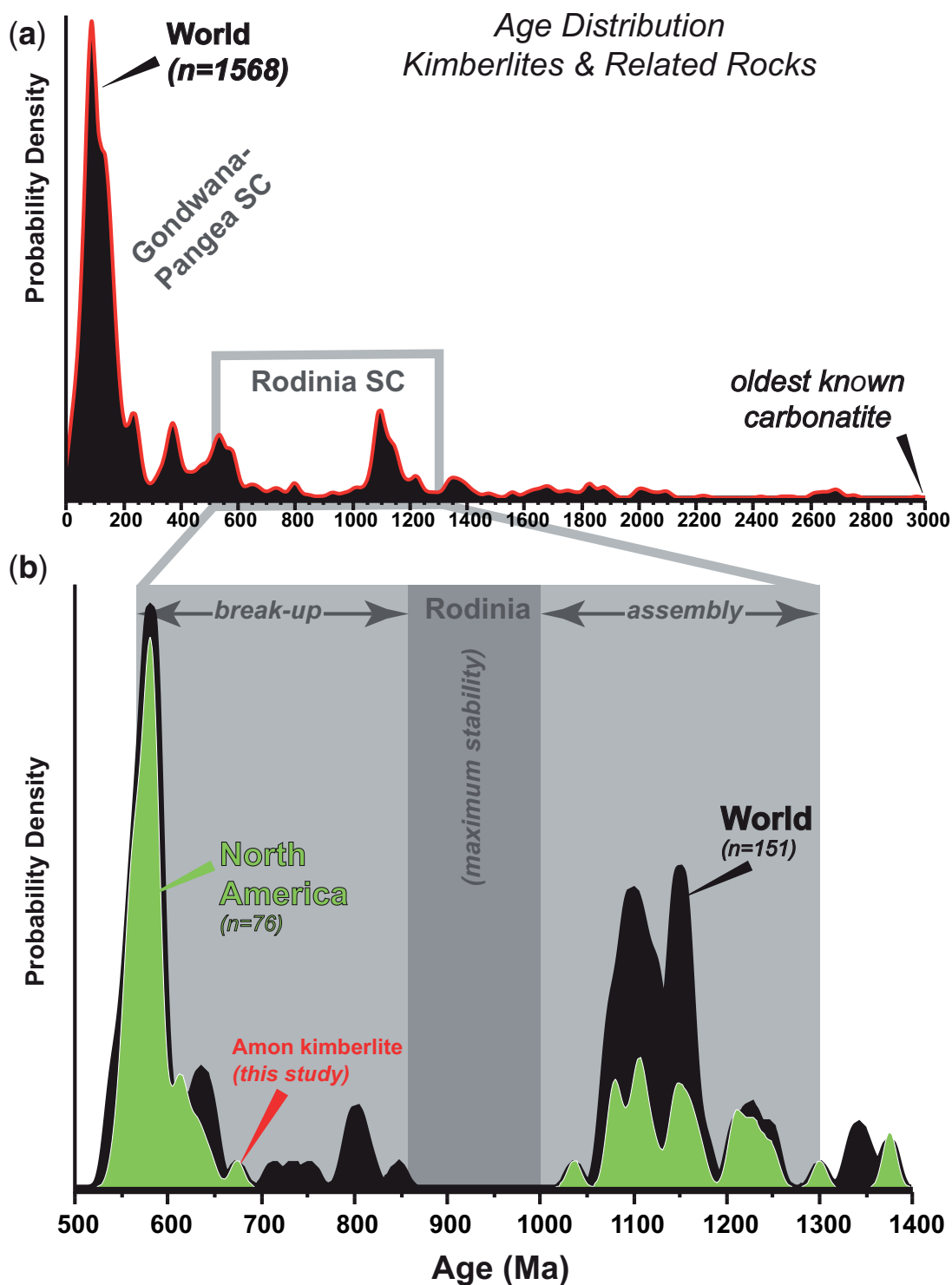


**Fig. 1.** Probability density of emplacement ages for global kimberlite and related rock occurrences (including carbonatites, UMLs, olivine lamproites). Only high-quality U–Pb, Pb–Pb, Ar–Ar, Rb–Sr, and Sm–Nd age determinations with reported  $2\sigma$  uncertainties of  $<50$  Ma were utilized in this compilation. (a) Frequency distribution of global kimberlite and related magmatism. The apparent absence, or lack of preservation, of kimberlite and related magmatism prior to 3 Ga should be noted (oldest entry is the  $\sim 3$  Ga Tupertalik carbonatite of West Greenland; Bizzarro *et al.*, 2002). Also noteworthy is the pronounced kimberlite magmatic activity that was associated with both the

(continued)

that kimberlite magmatism forms an integral part of a supercontinent cycle (see Jelsma *et al.*, 2009). We argue that kimberlite magmatism is an expression of fundamental changes in upper mantle flow patterns around thick cratonic nuclei that float within sizeable continental plates, and that these changes and resultant stresses may ultimately cause continental-scale rupturing of lithospheric plates and possibly supercontinent break-up.

Our results for the Amon kimberlites regarding their geochronology (Tables 1 and 2), mineral chemistry (Tables 3–5), and geochemistry (Tables 6 and 7), including Sr–Nd–Hf isotope compositions, are given in Supplementary Data Appendix A and Appendix B (supplementary data are available for downloading at <http://www.petrology.oxfordjournals.org>). Unless otherwise stated, use of the term kimberlite refers to archetypal, Group-I kimberlite.

## GEOLOGICAL BACKGROUND

### The Rae craton within the Laurentia configuration

The Late Neoproterozoic Amon Kimberlite Sill Complex (Tappe *et al.*, 2012a) is located in north-central Baffin Island and intrudes basement rocks of the northern domain of the Rae craton (Figs 2 and 3). The Rae craton is part of the Canadian–Greenland shield and is considered one of Laurentia's most important building blocks (Hoffman, 1988; Pehrsson *et al.*, 2013). It consists of Mesozoic to Neoproterozoic orthogneisses (3.3–2.6 Ga) and associated komatiite-bearing greenstone belts extending NE from central Northern Canada through Baffin Island into Greenland for almost 2000 km (Fig. 2). The Rae basement and supracrustal belts were intruded by voluminous tonalitic to granitic plutons between *c.* 2.68 and 2.58 Ga. A number of structural and metamorphic events are recorded between 2.56 and 1.75 Ga both within and along the margins of the various constituent blocks of the Rae craton (Berman *et al.*, 2013; Petts *et al.*, 2014). Extension of the Rae lithosphere is widespread and marked by *c.* 2.19–2.15 Ga mafic dyke swarms (Ernst & Bleeker, 2010), and by rift to passive margin sedimentation initiated at *c.* 2.1 Ga (Rainbird *et al.*, 2010). Pehrsson *et al.* (2013) recently proposed that the 2.1 Ga rifting episode recorded on the Rae craton marks the dispersal of a giant landmass

(Nunavutia), prior to the 2.0–1.8 Ga assembly of the supercraton Laurentia (Hoffman, 1988) within the Nuna–Columbia supercontinent configuration (Roberts, 2013). Laurentia assembly involved diachronous collisions between the pre-amalgamated Rae–Hearne craton (Churchill Province) and the Slave craton to the NW (Taltson–Thelon orogeny; 2.0–1.9 Ga), and between the Churchill Province and the Superior craton to the SE (Trans-Hudson orogeny; 1.9–1.8 Ga). The latter event included closure of the intervening Manikewan ocean during northward subduction beneath the Churchill Province, with Superior lithosphere forming the lower collisional plate (Corrigan *et al.*, 2009; St-Onge *et al.*, 2009).

The architecture of the Rae cratonic mantle lithosphere has been poorly studied to date, partially because of the paucity of known kimberlite occurrences that contain suitable mantle-derived xenoliths or xenocrysts. The *c.* 560 Ma Aviat kimberlites on Melville Peninsula, *c.* 300 km south of the Amon kimberlites in north-central Baffin Island (Fig. 2), contain harzburgitic garnets with Cr–Ca systematics that are suggestive of a maximum pressure of equilibration of 5.9 GPa (Armstrong *et al.*, 2008; Snyder & Grütter, 2010). This pressure corresponds to *c.* 190 km depth for an estimated conductive geotherm of 38 mW m<sup>−2</sup> (Snyder & Grütter, 2010), indicating that a thick lithospheric mantle root was present beneath the northern domain of the Rae craton during the Late Neoproterozoic (Peats *et al.*, 2012). Mesozoic kimberlites on Somerset Island, *c.* 500 km NW of the Amon kimberlites, sampled cratonic mantle of the northern Rae domain that had stabilized by *c.* 2.8 Ga (Irvine *et al.*, 2003). However, the oldest Re–Os model ages obtained for Rae peridotite xenoliths by Irvine and co-workers are younger than the >3 Ga Mesoarchean model ages that are recorded from the lithospheric mantle of the neighbouring Slave and North Atlantic cratons (Irvine *et al.*, 2003; Wittig *et al.*, 2010).

Recently, Snyder *et al.* (2013), in a study of earthquake receiver-functions, observed the presence of multiple, gently dipping (6–30°) anisotropic layers between 50 and 150 km depth within the cratonic mantle lithosphere beneath northern Hudson Bay and Baffin Island. They interpreted a regionally persistent discontinuity in the mantle fabric beneath the southeastern Rae craton as resulting from underthrusting of Archean Rae mantle lithosphere

**Fig. 1.** Continued

Gondwana–Pangea (510 Ma–Recent) and Rodinia (1300–550 Ma) supercontinent cycles (SC). For a higher resolution of the global Phanerozoic kimberlite emplacement age distribution the reader is referred to Jelsma *et al.* (2009). (b) Frequency distribution of global kimberlite and related magmatism during the Rodinia supercontinent cycle between 1400 and 500 Ma (the complete age compilation is provided in Supplementary Data Appendix C). Approximately 85% of the age population have 2σ uncertainties of <20 Ma, and this value was assigned as the bandwidth. The pronounced kimberlite magmatic activity during assembly and break-up of Rodinia should be noted, whereas no kimberlites and related rocks are recorded between *c.* 1000 and 850 Ma during maximum stability of the supercontinent configuration (see Li *et al.*, 2008). The *c.* 673 Ma Amon kimberlite of north-central Baffin Island appears to be the earliest manifestation of increased kimberlite magmatic activity in North America that accompanied the stepwise breakout of Laurentia from the Rodinia supercontinent.



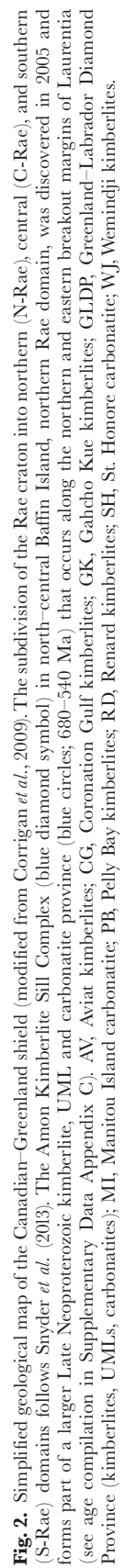


Table 1: ID-TIMS U–Pb results for groundmass rutile from the Amon Kimberlite Sill Complex in north-central Baffin Island, Rae craton, Arctic Canada

Description*	Weight U (μg)	Th (ppm)	Th/U (ppm)	Pb (ppm)	TCPb (pg)	<sup>206</sup> Pb/† <sup>204</sup> Pb	<sup>207</sup> Pb/† <sup>204</sup> Pb	<sup>208</sup> Pb/† <sup>204</sup> Pb	<sup>206</sup> Pb/‡ <sup>238</sup> U	<sup>207</sup> Pb/‡ <sup>235</sup> U	<sup>207</sup> Pb/‡ <sup>206</sup> Pb	Apparent age (Ma)	<sup>206</sup> Pb/ <sup>238</sup> U	<sup>207</sup> Pb/ <sup>238</sup> U
Amon kimberlite sill complex, drillhole BAF-0206-05-003 (42.35–42.50 m depth); N70-697426, W80-215146 (WGS84, decimal degrees)														
B1-1 (rutile), bright orange subhedral grains (80); IF0.8M; 50–100 μm	67 ± 1	20.4	70.4	3.5	9.7	374	43.10	17.39	65.43	0.11013 ± 258	1.0898 ± 1006	0.07177 ± 654	673.5 ± 15.0	748.4 ± 48.2
B1-2 (rutile), orange or yellow fragments (100); IF0.8M; 50–100 μm	101 ± 8	23.9	83.9	3.5	11.8	708	41.30	17.27	63.88	0.10985 ± 266	1.0943 ± 1140	0.07225 ± 740	671.9 ± 15.4	750.6 ± 54.6
													WA 672.7 ± 10.6 (2σ)	

\*Numbers in parentheses are numbers of grains analysed.

†Lead isotope compositions corrected for fractionation (0.105% per a.m.u. Pb), blank (5 pg Pb) and isotopic tracer; uncorrected for initial common Pb.

‡Atomic ratios corrected for fractionation (0.105% per a.m.u. Pb and 0.123% per a.m.u. U), blank (5 pg Pb; 1 pg U), isotopic tracer, and total initial common Pb (TCPb).

Thorium concentrations calculated based on amount of <sup>208</sup>Pb present and <sup>207</sup>Pb/<sup>206</sup>Pb model age; TCPb is estimated total initial common Pb based on the Stacey & Kramers (1975) terrestrial Pb evolution model. WA - weighted average age calculated with Isoplot (Ludwig, 2000). All uncertainties in this table are quoted at 2σ.

beneath the younger Superior margin during the Trans-Hudson orogeny. Furthermore, Snyder *et al.* (2013) were able to show that the northern domain of the Rae craton (i.e. our study area) dips west beneath the central Rae domain (Fig. 2). This geometry is best explained by complex accretion of the north Rae domain to the somewhat younger central Rae domain during the Neoproterozoic (Snyder *et al.*, 2013).

Although the current state of knowledge about the Rae mantle lithosphere is extremely limited compared with other cratons such as the Slave and Kaapvaal examples (Aulbach *et al.*, 2009), there are strong indications that its formation and modification were coupled to the evolution of the overlying crust during assembly and growth of the Laurentia supercraton within the Nuna supercontinent configuration that existed until 1.3 Ga (Roberts, 2013).

### Rodinia supercontinent break-up and increased kimberlite magmatic activity

The Rodinia supercontinent formed by extroversion of its predecessor Nuna between 1.3 and 1.0 Ga (Fig. 1); this process involved only minimal movement between lithospheric plates (Roberts, 2013, and references therein). For this reason the transition was much less dramatic in terms of the frequency and intensity of magmatic activity compared with the subsequent break-up of Rodinia between 750 and 570 Ma (Evans & Mitchell, 2011). Importantly, most paleocontinent reconstructions feature Laurentia at

the centre of Rodinia, which reached maximum stability at *c.* 900 Ma (Fig. 1b), because it is flanked entirely by Neoproterozoic passive margins (Torsvik, 2003; Davidson, 2008; Li *et al.*, 2008).

Rodinia's demise began with strong rifting activity along the western and southern margins of Laurentia at *c.* 750 Ma, which is commonly ascribed to mantle plume activity beneath the large and stagnant continental lid (Li *et al.*, 2008). The 723–712 Ma Franklin large igneous province (LIP) is widespread across the Canadian Arctic and this magmatic event provides strong testimony to increased mantle plume activity along Laurentia's northern breakout margin (Davidson, 2008; Ernst & Bleeker, 2010). For example, a NW–SE-trending giant mafic dyke swarm of the Franklin LIP runs across northern Baffin Island, more than 1000 km distal to the inferred plume centre on Victoria Island (Pehrsson & Buchan, 1999; Denyszyn *et al.*, 2009). Importantly, the *c.* 673 Ma Amon kimberlite sills in north-central Baffin Island (Tappe *et al.*, 2012a; this study) are only marginally younger than the spatially overlapping 723–712 Ma Franklin LIP, which clearly is related to Rodinia supercontinent break-up.

Our compilation of published ages for North American kimberlites and related rocks (Supplementary Data Appendix C) reveals that continuous CO<sub>2</sub>-rich magmatic activity occurred proximal to the northern and eastern breakout margins of Laurentia between 680 and 540 Ma (Fig. 1). The increased activity occurred after a prolonged

Table 2:  $^{40}\text{Ar}/^{39}\text{Ar}$  results for groundmass phlogopite grains from float sample FN5 of the Amon Kimberlite Sill Complex in north-central Baffin Island, Rae craton, Arctic Canada

Grain	Step no.	Cum. % <sup>39</sup> Ar	<sup>40</sup> Ar <sup>1</sup> (× 10 <sup>-13</sup> moles)	±1σ	<sup>39</sup> Ar <sup>1</sup> (× 10 <sup>-14</sup> moles)	±1σ	<sup>38</sup> Ar <sup>1</sup> (× 10 <sup>-16</sup> moles)	±1σ	<sup>37</sup> Ar <sup>1</sup> (× 10 <sup>-16</sup> moles)	±1σ	<sup>36</sup> Ar <sup>1</sup> (× 10 <sup>-16</sup> moles)	±1σ
FN5/1	(1) low- <i>T</i>	100.0	0.06503	0.00018	0.01245	0.00014	0.0022	0.0022	0.185	0.007	0.0134	0.0018
FN5/2	(1) low- <i>T</i>	34.2	0.05904	0.00015	0.01394	0.00002	0.0176	0.0026	1.071	0.015	0.0627	0.0035
	(2) high- <i>T</i> <sup>2</sup>	100.0	0.16534	0.00038	0.02679	0.00016	0.0002	0.0032	0.100	0.009	0.0035	0.0019
FN5/3	(1) low- <i>T</i>	79.3	0.12297	0.00034	0.02344	0.00007	0.0168	0.0027	0.189	0.003	0.0493	0.0031
	(2) high- <i>T</i>	100.0	0.04031	0.00014	0.00612	0.00001	0.0002	0.0010	0.012	0.003	0.0046	0.0008
FN5/4	(1) low- <i>T</i>	28.3	0.06064	0.00016	0.01354	0.00012	0.0129	0.0034	0.346	0.012	0.0628	0.0021
	(2) high- <i>T</i> <sup>2</sup>	100.0	0.20762	0.00051	0.03423	0.00024	0.0011	0.0034	0.087	0.010	0.0129	0.0017
FN5/5	(1) low- <i>T</i>	68.7	0.11577	0.00028	0.02366	0.00016	0.0075	0.0025	2.163	0.024	0.0349	0.0016
	(2) high- <i>T</i> <sup>2</sup>	100.0	0.06609	0.00018	0.01079	0.00003	0.0034	0.0022	0.043	0.003	0.0009	0.0009
FN5/6	(1) low- <i>T</i>	67.2	0.07136	0.00017	0.01506	0.00004	0.0102	0.0018	0.300	0.017	0.0268	0.0038
	(2) high- <i>T</i> <sup>2</sup>	100.0	0.04695	0.00011	0.00735	0.00007	0.0052	0.0009	0.060	0.014	0.0055	0.0022
FN5/7	(1) low- <i>T</i>	58.4	0.16475	0.00053	0.03506	0.00019	0.0196	0.0014	0.411	0.006	0.0679	0.0024
	(2) high- <i>T</i> <sup>2</sup>	88.8	0.10920	0.00028	0.01820	0.00022	0.0030	0.0008	0.035	0.007	0.0051	0.0009
	(3) high- <i>T</i> <sup>2</sup>	100.0	0.04240	0.00013	0.00675	0.00006	0.0039	0.0014	0.038	0.007	0.0063	0.0011
Grain	Ca/K	±1σ	% <sup>40</sup> Ar*	<sup>40</sup> Ar*/ <sup>39</sup> Ar	±1σ	Age <sup>3</sup> (Ma)	±1σ	Age <sup>4</sup> ± 1σ (Ma)				
FN5/1	0.260	0.010	93.9	49.04	0.72	547.1	6.9	551.8 ± 7.0				
FN5/2	1.345	0.019	68.6	29.08	0.75	344.0	8.0	347.2 ± 8.1				
	0.065	0.006	99.4	61.33	0.46	661.6	4.1	667.2 ± 4.1 <sup>2</sup>				
FN5/3	0.141	0.002	88.2	46.24	0.44	519.9	4.3	524.4 ± 4.3				
	0.036	0.009	96.6	63.62	0.48	682.3	4.3	688.0 ± 4.3				
FN5/4	0.447	0.016	69.4	31.10	0.55	365.6	5.8	369.0 ± 5.8				
	0.045	0.005	98.2	59.55	0.46	645.5	4.2	650.9 ± 4.2 <sup>2</sup>				
FN5/5	1.599	0.020	91.1	44.57	0.38	503.5	3.7	507.9 ± 3.7				
	0.069	0.006	99.6	61.01	0.36	658.8	3.3	664.3 ± 3.3 <sup>2</sup>				
FN5/6	0.349	0.020	88.9	42.12	0.76	479.3	7.6	483.5 ± 7.7				
	0.144	0.034	96.5	61.67	1.06	664.8	9.6	670.4 ± 9.7 <sup>2</sup>				
FN5/7	0.205	0.003	87.8	41.27	0.34	470.8	3.4	475.0 ± 3.4				
	0.034	0.007	98.6	59.16	0.74	641.9	6.7	647.3 ± 6.7 <sup>2</sup>				
	0.098	0.019	95.6	60.02	0.74	649.8	6.7	655.3 ± 6.7 <sup>2</sup>				
									WA 660.1 ± 8.6 (2σ; <i>n</i> = 6)			

Kimberlite FN5 (302/616/0001): N70-502048, W80-06288 (WGS84, decimal degrees);  $J$ -value =  $0.007224 \pm 0.000013$ .  $J$ -value calculation based on an age of 98.8 Ma for GA1550 biotite (Renne *et al.*, 1998). Interference corrections:  $(^{36}\text{Ar}/^{37}\text{Ar})_{\text{Ca}} = 2.63(1) \times 10^{-4}$ ;  $(^{39}\text{Ar}/^{37}\text{Ar})_{\text{Ca}} = 6.86(3) \times 10^{-4}$ ;  $(^{40}\text{Ar}/^{39}\text{Ar})_{\text{K}} = 1.5 \times 10^{-3}$ . WA, weighted average age calculated with Isoplot (Ludwig, 2000).

<sup>1</sup>Data are corrected for mass spectrometer backgrounds, discrimination, and radioactive decay, but not for isotopic interferences.

<sup>2</sup>Preferred laser heating step for age calculation (see main text for discussion).

<sup>3</sup>Age calculated based on decay constants of Steiger & Jäger (1977) and an age of 98.8 Ma for GA1550 biotite (Renne *et al.*, 1998).

<sup>4</sup>Age calculated using the decay constants and standard ages of Renne *et al.* (2010, 2011).

*Table 3: Representative groundmass phlogopite compositions of the Amon Kimberlite Sill Complex in north-central Baffin Island, Rae craton, Arctic Canada*

Sample no.:	A1 gm core1	A1 gm core2	A1 gm core3	A1 gm core4	A1 gm core5	A2 gm core1	A2 gm core2	A2 gm core3	A2 gm core4
SiO <sub>2</sub>	38.70	38.21	35.79	35.72	35.54	31.16	31.38	31.56	30.99
TiO <sub>2</sub>	3.91	3.58	3.61	3.39	3.32	1.06	0.85	0.83	1.06
Al <sub>2</sub> O <sub>3</sub>	13.18	13.48	16.20	16.24	16.05	18.84	18.64	18.11	18.40
Cr <sub>2</sub> O <sub>3</sub>	1.61	1.67	0.15	0.09	0.03	0.00	0.00	0.00	0.00
FeO	4.94	4.71	5.65	5.52	5.65	3.01	2.94	2.86	3.03
MnO	0.08	0.05	0.01	0.05	0.07	0.11	0.09	0.10	0.10
MgO	21.88	21.53	21.48	21.46	21.75	24.19	24.40	24.31	23.62
CaO	0.02	0.01	0.02	0.03	0.05	0.05	0.04	0.07	0.07
BaO	0.19	0.18	1.15	1.31	1.22	7.27	7.16	6.35	7.05
Na <sub>2</sub> O	0.24	0.21	0.17	0.20	0.11	0.08	0.07	0.07	0.09
K <sub>2</sub> O	9.96	9.80	9.52	9.60	9.14	7.50	7.77	7.78	7.43
F	0.54	0.52	0.40	0.53	0.21	0.83	0.79	0.89	0.97
Cl	0.03	0.05	0.03	0.00	0.01	0.02	0.00	0.00	0.03
O = F	-0.23	-0.22	-0.17	-0.22	-0.09	-0.35	-0.33	-0.37	-0.41
Total	95.05	93.78	94.00	93.91	93.06	93.78	93.79	92.54	92.43

Sample no.:	A4 gm core1	A4 gm core2	A4 gm core3	A4 gm core4	A8 gm core1	A8 gm core2	A8 gm rim1
SiO <sub>2</sub>	34.16	34.10	33.93	33.46	35.49	35.62	35.84
TiO <sub>2</sub>	2.88	2.84	1.57	0.93	3.21	0.77	0.79
Al <sub>2</sub> O <sub>3</sub>	17.02	17.18	17.83	18.26	16.14	17.12	17.78
Cr <sub>2</sub> O <sub>3</sub>	0.00	0.01	0.00	0.01	0.04	0.02	0.02
FeO	4.64	4.53	4.97	3.86	4.93	3.94	3.90
MnO	0.07	0.03	0.08	0.10	0.01	0.12	0.11
MgO	22.86	22.62	23.12	23.34	23.88	24.17	24.07
CaO	0.11	0.13	0.14	0.09	0.19	0.12	0.06
BaO	1.48	1.75	2.83	4.04	1.29	3.63	4.28
Na <sub>2</sub> O	0.19	0.22	0.13	0.11	0.17	0.09	0.08
K <sub>2</sub> O	8.32	8.64	8.18	8.20	7.04	7.77	8.81
F	0.35	0.43	0.45	0.64	0.61	0.63	0.61
Cl	0.02	0.05	0.00	0.03	0.05	0.01	0.00
O = F	-0.15	-0.18	-0.19	-0.27	-0.26	-0.26	-0.25
Total	91.95	92.36	93.04	92.79	92.80	93.74	96.09

(continued)



Table 3: Continued

Sample no.:	A11	A11	A11	A11	A11	B5	B5	B5
	gm	gm	gm	gm	gm	gm	gm	gm
	core1	core2	core3	core4	core5	core1	core2	core3
SiO <sub>2</sub>	35.97	35.37	34.91	33.70	35.09	32.82	32.93	33.44
TiO <sub>2</sub>	3.13	3.16	3.06	2.99	1.78	0.62	0.62	0.44
Al <sub>2</sub> O <sub>3</sub>	15.77	15.93	15.97	16.39	17.52	18.93	19.18	18.74
Cr <sub>2</sub> O <sub>3</sub>	0.09	0.05	0.01	0.02	0.07	0.00	0.02	0.00
FeO	6.09	6.28	6.37	6.99	4.74	2.55	2.65	2.72
MnO	0.07	0.08	0.05	0.05	0.06	0.04	0.06	0.05
MgO	22.87	23.06	23.20	23.30	23.46	24.08	24.16	24.15
CaO	0.06	0.06	0.06	0.08	0.04	0.02	0.03	0.04
BaO	1.06	1.18	1.31	1.66	3.00	9.00	8.93	8.25
Na <sub>2</sub> O	0.18	0.18	0.15	0.06	0.11	0.07	0.04	0.08
K <sub>2</sub> O	8.36	8.11	7.80	7.39	8.56	7.07	7.01	7.33
F	0.50	0.45	0.41	0.60	0.51	0.74	0.68	0.82
Cl	0.01	0.02	0.02	0.01	0.00	0.00	0.00	0.02
O = F	-0.21	-0.19	-0.17	-0.25	-0.21	-0.31	-0.29	-0.34
Total	93.94	93.74	93.16	92.98	94.72	95.62	96.02	95.72

Sample no.:	B6	B6	B6	B6	B6	B6	B6
	gm	gm	gm	gm	gm	gm	gm
	core1	core2	core3	rim1	rim2	rim3	rim4
SiO <sub>2</sub>	36.56	36.26	36.10	36.53	36.89	35.49	35.59
TiO <sub>2</sub>	3.29	3.22	3.55	3.50	3.24	0.74	0.87
Al <sub>2</sub> O <sub>3</sub>	15.29	15.01	15.87	15.75	14.99	16.08	17.57
Cr <sub>2</sub> O <sub>3</sub>	0.13	0.26	0.03	0.07	0.05	0.01	0.06
FeO	5.69	5.85	5.47	5.67	5.61	5.78	3.70
MnO	0.06	0.04	0.04	0.07	0.10	0.08	0.08
MgO	23.36	23.32	22.52	23.30	23.60	24.93	23.61
CaO	0.12	0.11	0.10	0.17	0.13	0.16	0.18
BaO	0.98	0.82	1.30	1.48	1.19	2.70	4.01
Na <sub>2</sub> O	0.20	0.19	0.14	0.13	0.16	0.06	0.08
K <sub>2</sub> O	7.01	6.79	8.28	7.97	7.19	6.75	8.09
F	0.55	0.44	0.58	0.51	0.31	0.64	0.69
Cl	0.01	0.03	0.02	0.03	0.02	0.02	0.00
O = F	-0.23	-0.18	-0.24	-0.21	-0.13	-0.27	-0.29
Total	93.03	92.16	93.75	94.95	93.36	93.17	94.24

gm, groundmass.

'shutdown' of deep-seated CO<sub>2</sub>-rich magmatism that coincides with maximum stability of the Rodinia supercontinent configuration between *c.* 1000 and 850 Ma (Li *et al.*, 2008). It therefore appears that the prolonged break-up process of Rodinia was accompanied by sublithospheric kimberlite melt production beneath the rifting

supercontinent, which is particularly well recorded along the northern and eastern margins of Laurentia (present-day cratonic North America and Greenland) (Fig. 2). Similar connections have been made to reconcile the apparent spatial and temporal relationships between Gondwana superterrane break-up and coeval kimberlite and related

Table 4: Representative spinel compositions (macrocrysts and groundmass), Amon Kimberlite Sill Complex, north-central Baffin Island, Rae craton, Arctic Canada

Sample no.:	Cr-Spl A1 gm1 core	Cr-Spl A1 gm1 rim	Mag A1 gm26 core	Mag A1 gm26 core	Cr-Spl A2 gm19 core	Cr-Spl A2 gm19 core	Cr-Spl A3 gm7 core	Cr-Spl A3 gm7 core	Cr-Spl A4 gm25 core	Cr-Spl A4 gm25 core
TiO <sub>2</sub>	5.51	7.33	0.07	0.10	1.03	1.02	5.74	7.30	7.05	9.88
Al <sub>2</sub> O <sub>3</sub>	6.92	5.59	0.02	0.01	11.14	10.92	5.97	5.93	5.68	7.07
Cr <sub>2</sub> O <sub>3</sub>	47.62	42.01	0.08	0.08	52.50	52.74	46.31	40.20	45.84	33.47
V <sub>2</sub> O <sub>3</sub>	0.30	0.34	0.16	0.15	0.33	0.33	0.32	0.33	0.31	0.30
FeO*	26.36	29.21	88.76	88.46	20.73	20.94	27.06	30.61	26.87	32.50
MnO	0.00	0.33	0.61	0.09	0.40	0.38	0.00	0.03	0.00	0.32
NiO	0.14	0.13	0.00	0.01	0.04	0.05	0.11	0.12	0.11	0.14
MgO	12.46	12.73	0.20	0.45	11.74	11.93	12.56	12.57	10.07	10.87
Total	99.31	97.68	89.90	89.34	97.90	98.30	98.07	97.08	95.93	94.55
Sample no.:	Mag A6 gm2 core	Cr-Spl A9 gm8 core	Cr-Spl A9 gm8 core	Cr-Spl A9 gm12 core	Mag A12 gm7 core	Mag A12 gm7 core	Ti-Mag A12 gm8 core	Ti-Mag A12 gm8 core	Cr-Spl A12 gm14 core	Cr-Spl A12 gm14 core
TiO <sub>2</sub>	1.84	11.82	13.00	13.07	0.18	0.18	4.75	4.71	5.83	5.73
Al <sub>2</sub> O <sub>3</sub>	0.00	7.92	7.34	6.96	0.17	0.15	4.58	4.58	5.02	5.11
Cr <sub>2</sub> O <sub>3</sub>	0.11	23.68	24.70	14.07	0.53	0.48	0.04	0.03	44.71	44.44
V <sub>2</sub> O <sub>3</sub>	0.04	0.26	0.35	0.24	0.24	0.26	0.14	0.15	0.29	0.34
FeO*	89.38	40.75	39.30	44.86	89.55	88.90	71.95	72.07	29.46	29.38
MnO	1.15	0.58	1.04	1.13	0.59	0.67	1.35	1.39	0.29	0.26
NiO	0.01	0.10	0.18	0.12	0.05	0.07	0.02	0.03	0.12	0.12
MgO	1.89	12.92	13.63	11.59	1.75	1.46	10.69	10.47	11.98	12.04
Total	94.41	98.02	99.53	92.04	93.06	92.17	93.51	93.43	97.69	97.42
Sample no.:	Cr-Spl B2 gm8 core	Cr-Spl B2 gm8 core	Cr-Spl B2 gm8 rim	Cr-Spl B2 gm10 core	Cr-Spl B2 gm10 core	Cr-Spl B2 gm10 core	Cr-Spl B4 gm7 core	Cr-Spl B4 gm7 core	Cr-Spl B4 gm7 core	Ti-Mag B5 gm6 core
TiO <sub>2</sub>	6.25	6.22	7.39	8.58	9.05	10.05	6.36	6.94	8.80	27.36
Al <sub>2</sub> O <sub>3</sub>	4.91	4.85	5.71	6.23	6.57	7.26	4.80	5.39	6.96	7.35
Cr <sub>2</sub> O <sub>3</sub>	44.84	44.91	38.85	34.55	32.16	27.20	45.55	41.79	31.52	2.16
V <sub>2</sub> O <sub>3</sub>	0.35	0.37	0.34	0.32	0.32	0.30	0.29	0.27	0.22	0.25
FeO*	29.17	28.72	31.82	33.85	34.76	37.43	27.90	29.71	35.49	39.53
MnO	1.05	1.10	1.32	1.61	1.41	1.74	0.74	1.00	0.55	1.01
NiO	0.12	0.12	0.13	0.15	0.12	0.11	0.11	0.12	0.14	0.20
MgO	12.30	12.30	12.82	13.34	13.68	14.14	12.34	12.71	13.18	17.90
Total	98.99	98.60	98.38	98.63	98.07	98.23	98.08	97.93	96.86	95.76

(continued)

Table 4: Continued

Sample no.:	Mag	Mag	Cr-Spl	Cr-Spl	Cr-Spl	Cr-Spl	Ti-Mag	Ti-Mag	Ti-Mag
	B6	B6	B6	B6	B6	B6	A7	A7	A7
	gm6	gm6	gm7	gm7	gm7	gm16	mc1	mc1	mc1
	core	core	core	core	core	core	core	core	rim
TiO <sub>2</sub>	0.26	0.26	6.33	6.49	6.40	6.65	15.71	16.15	17.12
Al <sub>2</sub> O <sub>3</sub>	0.28	0.27	6.24	5.93	6.14	5.85	0.41	0.46	0.80
Cr <sub>2</sub> O <sub>3</sub>	0.07	0.04	47.77	47.11	47.94	43.16	0.13	0.17	0.14
V <sub>2</sub> O <sub>3</sub>	0.30	0.31	0.38	0.39	0.33	0.31	0.45	0.52	0.46
FeO*	87.70	87.35	26.13	26.60	26.08	28.55	74.60	74.08	72.02
MnO	0.91	0.73	0.70	0.80	0.56	0.19	2.48	1.98	2.43
NiO	0.05	0.05	0.16	0.14	0.15	0.14	0.00	0.01	0.04
MgO	0.36	0.28	9.57	8.74	8.84	10.39	0.01	0.03	0.04
Total	89.92	89.28	97.28	96.20	96.44	95.24	93.80	93.40	93.04

Sample no.:	Mag	Mag	Mag	Mag	Mag	Mag	Mag	Mag	Mag
	A11	A11	A11	B3	B3	B3	B6	B6	B6
	mc1	mc1	mc1	mc1	mc1	mc1	mc10	mc10	mc10
	core	core	rim	core	core	rim	core	core	rim
TiO <sub>2</sub>	0.06	0.09	0.23	0.02	0.04	0.03	0.46	0.42	1.35
Al <sub>2</sub> O <sub>3</sub>	0.29	0.25	0.26	0.06	0.04	0.04	0.44	0.49	0.56
Cr <sub>2</sub> O <sub>3</sub>	0.22	0.23	0.19	0.03	0.02	0.03	0.67	0.65	0.68
V <sub>2</sub> O <sub>3</sub>	0.37	0.41	0.36	0.28	0.19	0.25	0.72	0.67	0.71
FeO*	91.81	90.99	90.47	92.78	92.97	93.09	86.69	86.30	84.29
MnO	0.35	0.78	1.19	1.84	0.87	1.60	0.97	1.13	0.86
NiO	0.00	0.00	0.01	0.00	0.01	0.01	0.03	0.01	0.05
MgO	0.13	0.11	0.52	0.04	0.06	0.04	0.31	0.54	1.23
Total	93.24	92.87	93.24	95.05	94.19	95.09	90.28	90.21	89.72

Cr-Spl, chromian spinel; Ti-Mag, titanomagnetite; Mag, magnetite; mc, macrocryst; gm, groundmass.

\*Total Fe given as FeO.

magmatism along the southern and central Atlantic margins (Marsh, 1973; Jelsma *et al.*, 2004, 2009; Moore *et al.*, 2008).

Presently known Late Neoproterozoic kimberlite and associated rock types that are believed to be associated with the stepwise breakout of Laurentia from the Rodinia supercontinent between 680 and 540 Ma are shown in Fig. 2. The following occurrences are discussed here in conjunction with the petrogenesis of the Amon kimberlites from north-central Baffin Island, Nunavut: *c.* 629 Ma Wemindji kimberlites (Quebec), *c.* 632 Ma Renard kimberlites (Quebec), *c.* 560 Ma Aviat kimberlites (Nunavut), *c.* 540 Ma Pelly Bay kimberlites (Nunavut), *c.* 613 Ma Coronation Gulf kimberlites (Nunavut), and the 610–550 Ma Greenland–Labrador Diamond Province [Majuagaa–Maniitsoq–Sarfartoq

kimberlites and ultramafic lamprophyres (UMLs), Torngat kimberlites and UMLs, Aillik Bay UMLs].

## AMON KIMBERLITE SILL COMPLEX (AKSC)

### Size and geometry

Several thin, flat-lying hypabyssal kimberlite sheets were discovered in the Nina Bang Lake area (70°8667'N, 79°4000'W) of north-central Baffin Island by De Beers Canada Inc. during exploration drilling in 2005 (Fig. 3). The so-called Amon kimberlite was further delineated during drilling in 2006, and an additional kimberlite sheet ('Aliguja', meaning diamond in Inuktitut) was

Table 5: Representative ilmenite compositions (macrocrysts and groundmass), as well as rutile and titanomagnetite overgrowths, Amon Kimberlite Sill Complex, north-central Baffin Island, Rae craton, Arctic Canada

Sample no.:	Ilm A6 mc3 core	Ilm A6 mc3 core	Ilm A6 mc3 rim	Ilm A6 mc4 core	Rt A6 mc4 rim	Ilm A6 mc6 core	Ilm A6 mc6 core	Ilm A6 mc6 core	Ilm A6 mc6 core	Rt A6 mc6 rim
TiO <sub>2</sub>	52.61	52.26	53.71	53.22	91.48	52.12	52.30	53.36	54.14	95.04
Al <sub>2</sub> O <sub>3</sub>	0.86	0.92	0.53	0.53	0.01	0.69	0.76	0.77	0.56	0.01
Cr <sub>2</sub> O <sub>3</sub>	1.94	1.82	3.15	3.67	0.60	0.68	0.67	0.69	1.88	1.46
V <sub>2</sub> O <sub>3</sub>	0.67	0.69	0.49	0.55	0.46	0.51	0.55	0.52	0.56	0.50
FeO*	26.54	26.14	22.40	23.11	2.83	31.29	30.91	28.95	24.95	1.77
MnO	1.22	1.82	1.07	0.96	1.69	1.08	0.56	0.90	0.85	0.74
NiO	0.14	0.14	0.11	0.11	0.02	0.11	0.14	0.12	0.13	0.00
MgO	16.31	16.14	18.31	18.42	0.03	14.34	14.60	15.42	17.56	0.04
Total	100.29	99.92	99.76	100.57	97.12	100.82	100.48	100.73	100.64	99.56
Sample no.:	Rt A6 mc6 rim	Rt A6 mc6 rim	Ilm A11 gm12 core	Ilm A11 gm12 core	Ilm A11 gm12 core	Ilm A11 gm12 rim	Ilm A11 gm12 rim	Rt A11 gm12 rim	Rt A11 gm12 rim	Rt A11 gm12 rim
TiO <sub>2</sub>	95.79	95.96	53.22	52.65	53.07	52.47	51.90	95.17	94.11	93.70
Al <sub>2</sub> O <sub>3</sub>	0.02	0.02	0.37	0.36	0.40	0.45	0.38	0.00	0.03	0.07
Cr <sub>2</sub> O <sub>3</sub>	0.87	0.89	2.91	3.80	2.95	3.04	4.24	1.00	0.66	0.51
V <sub>2</sub> O <sub>3</sub>	0.57	0.53	0.49	0.42	0.52	0.49	0.47	0.52	0.50	0.50
FeO*	1.74	1.77	25.99	25.70	26.45	26.20	25.70	0.85	1.79	1.81
MnO	0.75	0.35	1.32	1.10	0.94	0.99	1.28	1.23	0.75	0.47
NiO	0.00	0.01	0.06	0.07	0.10	0.05	0.09	0.00	0.02	0.00
MgO	0.03	0.06	15.77	15.84	15.88	15.94	15.62	0.04	0.15	0.03
Total	99.77	99.60	100.13	99.95	100.31	99.63	99.68	98.79	98.00	97.09
Sample no.:	Ilm A12 mc1 core	Ilm A12 mc1 core	Ilm A12 mc1 core	Ilm A12 mc1 core	Ilm A12 mc1 rim	Ilm A12 mc1 rim	Ilm A12 mc1 rim	Ilm A12 mc1 rim	Rt A12 mc1 rim	Rt A12 mc1 rim
TiO <sub>2</sub>	51.63	51.38	51.42	51.42	52.66	53.20	51.73	96.37	94.42	
Al <sub>2</sub> O <sub>3</sub>	0.61	0.56	0.54	0.55	0.55	0.46	0.56	0.01	0.01	
Cr <sub>2</sub> O <sub>3</sub>	0.66	0.66	0.66	0.64	0.66	1.16	0.69	0.94	1.20	
V <sub>2</sub> O <sub>3</sub>	0.58	0.58	0.61	0.61	0.59	0.54	0.63	0.46	0.50	
FeO*	31.98	32.52	32.59	32.52	29.77	28.89	31.57	0.86	1.32	
MnO	0.56	0.72	0.78	0.48	0.46	0.48	0.30	0.16	0.07	
NiO	0.11	0.10	0.11	0.10	0.11	0.11	0.10	0.00	0.02	
MgO	13.73	13.58	13.45	13.64	14.91	15.33	14.32	0.03	0.00	
Total	99.87	100.10	100.14	99.96	99.72	100.16	99.90	98.82	97.54	

(continued)

Table 5: Continued

Sample no.:	Ilm B1 mc1 core	Ilm B1 mc1 core	Ilm B1 mc1 rim	Ilm B1 mc5 core	Ilm B1 mc5 core	Ilm B1 mc5 rim	Rt B1 mc5 rim	Ilm B1 gm25 core	Ilm B1 gm25 core
TiO <sub>2</sub>	52.14	52.20	54.30	51.70	51.67	51.66	97.44	51.26	51.55
Al <sub>2</sub> O <sub>3</sub>	0.58	0.60	0.64	0.60	0.58	0.57	0.01	0.90	0.89
Cr <sub>2</sub> O <sub>3</sub>	1.38	1.36	2.31	0.39	0.41	0.39	0.52	1.05	1.02
V <sub>2</sub> O <sub>3</sub>	0.46	0.49	0.48	0.55	0.60	0.61	0.46	0.63	0.62
FeO*	30.95	30.26	24.59	34.08	33.97	33.10	0.52	31.09	31.01
MnO	0.79	0.70	0.69	0.98	0.93	1.01	0.82	0.76	0.82
NiO	0.12	0.13	0.13	0.09	0.11	0.08	0.00	0.13	0.11
MgO	13.34	13.59	16.96	12.17	12.27	12.66	0.04	14.18	14.36
Total	99.76	99.31	100.10	100.56	100.54	100.08	99.80	99.99	100.38
Sample no.:	Ilm B1 gm25 rim	Rt B1 gm25 rim	Rt B1 gm25 rim	Rt B1 gm25 rim	Ilm B3 mc1 core	Ilm B3 mc1 rim	Rt B3 mc1 rim	Rt B3 mc1 rim	Rt B3 mc1 rim
TiO <sub>2</sub>	51.39	96.13	96.23	97.35	51.79	50.81	96.11	96.49	96.81
Al <sub>2</sub> O <sub>3</sub>	0.89	0.03	0.03	0.01	0.59	0.58	0.01	0.00	0.01
Cr <sub>2</sub> O <sub>3</sub>	1.00	0.53	0.65	0.12	0.45	0.41	0.25	0.15	0.39
V <sub>2</sub> O <sub>3</sub>	0.64	0.52	0.49	0.48	0.50	0.62	0.70	0.52	0.45
FeO*	30.96	1.68	1.66	0.99	34.15	33.80	1.72	1.49	1.00
MnO	0.83	0.75	0.48	0.99	0.00	1.60	1.44	0.74	1.55
NiO	0.12	0.02	0.01	0.00	0.11	0.11	0.00	0.00	0.03
MgO	14.07	0.04	0.12	0.04	11.98	12.13	0.01	0.02	0.03
Total	99.90	99.69	99.68	99.98	99.56	100.06	100.24	99.41	100.25
Sample no.:	Ilm B3 mc2 core	Ilm B3 mc2 rim	Rt B3 mc2 rim	Rt B3 mc2 rim	Ilm B5 gm6 core	Ti-Mag B5 gm6 core	Ilm B5 gm6 core	Ilm B5 mc6 core	Ilm B5 mc6 core
TiO <sub>2</sub>	49.53	50.39	93.26	97.39	48.64	27.36	51.29	53.00	53.15
Al <sub>2</sub> O <sub>3</sub>	0.52	0.70	0.08	0.01	1.23	7.35	0.50	0.72	0.74
Cr <sub>2</sub> O <sub>3</sub>	1.07	1.16	0.75	0.13	2.97	2.16	2.55	0.97	0.99
V <sub>2</sub> O <sub>3</sub>	0.52	0.64	0.56	0.46	0.37	0.25	0.43	0.59	0.62
FeO*	34.92	32.41	3.33	1.50	27.56	39.53	31.51	29.23	29.01
MnO	1.11	0.93	1.68	0.81	0.77	1.01	1.03	0.93	0.96
NiO	0.14	0.13	0.00	0.00	0.07	0.20	0.07	0.16	0.12
MgO	12.98	14.35	0.08	0.02	17.78	17.90	13.51	15.15	15.32
Total	100.79	100.70	99.74	100.32	99.39	95.76	100.89	100.75	100.92

Ilm, ilmenite; Rt, rutile; Ti-Mag, titanomagnetite; mc, macrocryst; gm, groundmass.

\*Total Fe given as FeO.



Table 6: Major (wt %) and trace element (ppm) concentrations of the Amon kimberlite sills in north-central Baffin Island, Rae craton, Arctic Canada

Sample no.	Drillhole (depth in meters) (vertical and inclined)	Kimberlite sheet	SiO <sub>2</sub>	TiO <sub>2</sub>	Al <sub>2</sub> O <sub>3</sub>	Fe <sub>2</sub> O <sub>3</sub> <sup>T</sup>	MnO	MgO	CaO	Na <sub>2</sub> O	K <sub>2</sub> O	P <sub>2</sub> O <sub>5</sub>	LOI	CO <sub>2</sub>	Total				
A10	AMON06-005c (25-16-25-24 m)	Amon	34.8	2.17	2.92	6.76	0.12	22.0	11.86	0.11	0.46	0.87	16.8	12.7	98.9				
A8	AMON06-005c (28-60-28-72 m)	Amon	23.2	1.90	2.24	9.69	0.17	24.3	13.20	0.06	0.56	0.85	23.5	18.0	99.7				
A4	AMON06-005c (29-30-29-48 m)	Amon	22.6	2.97	3.00	9.23	0.17	23.6	12.89	0.09	0.64	1.39	22.5	16.2	99.0				
A6	AMON06-005c (33-81-33-94 m)	Amon	30.3	3.46	2.60	7.65	0.12	27.1	8.34	0.04	0.16	0.45	19.4	10.8	99.6				
A7	AMON06-007c (29-67-29-82 m)	Amon	13.2	2.08	2.79	8.46	0.26	15.0	27.19	0.06	0.57	1.06	28.9	24.6	99.5				
A2	AMON06-007c (33-74-33-89 m)	Amon	36.5	2.49	3.32	9.38	0.12	23.0	9.85	0.10	0.72	0.98	12.7	8.9	99.1				
A5	AMON06-007c (36-28-36-44 m)	Amon	30.3	2.42	2.46	4.58	0.18	24.8	11.19	0.05	0.29	0.68	22.6	15.2	99.6				
A1	AMON06-008c (33-50-33-71 m)	Amon	29.9	2.43	3.57	4.88	0.15	20.4	16.38	0.17	1.42	0.75	18.9	15.0	98.9				
A11	AMON06-008c (34-18-34-30 m)	Amon	20.3	2.96	2.90	3.93	0.21	16.2	25.12	0.17	0.54	1.36	25.7	20.9	99.4				
A3	AMON06-009c (45-10-45-25 m)	Amon	39.3	2.95	3.29	15.27	0.14	23.0	4.08	0.19	0.73	1.00	9.2	3.7	99.2				
A9	AMON06-009c (45-77-46-01 m)	Amon	28.9	2.83	3.80	10.93	0.15	25.0	8.90	0.09	0.93	1.21	16.3	9.4	99.0				
A12	AMON06-012c (20-92-21-01 m)	Amon	25.3	2.54	2.53	7.81	0.14	21.8	16.98	0.10	0.43	0.85	20.6	12.9	99.1				
B5	BAF-0206-05-003 (41-95-42-15 m)	Amon	32.5	1.87	1.68	9.63	0.13	33.0	4.27	0.02	0.07	0.09	16.7	6.2	100.0				
B1	BAF-0206-05-003 (42-35-42-50 m)	Amon	37.9	2.15	1.82	6.49	0.10	29.0	5.40	0.15	0.10	0.35	16.4	6.8	99.9				
B2	BAF-0206-05-003 (84-10-84-15 m)	Amon	37.4	2.27	3.75	5.03	0.10	22.0	13.12	0.18	0.55	0.71	14.7	7.8	99.7				
B3	BAF-0206-05-004 (65-48-65-61 m)	Amon	29.6	2.66	4.02	6.11	0.13	19.4	16.65	0.09	0.06	0.35	20.7	12.2	99.8				
B4	BAF-0206-05-004 (72-40-72-49 m)	Amon	29.3	2.79	2.43	9.14	0.17	23.8	12.54	0.04	0.28	0.54	17.7	9.3	98.7				
B7	BAF-0340-06-001c (22-46-22-61 m)	Aliguja	29.1	2.47	3.68	10.17	0.13	20.7	10.91	0.09	0.85	0.45	20.8	15.1	99.4				
B6	BAF-0340-06-002c (25-29-25-43 m)	Aliguja	23.6	2.81	3.96	7.28	0.13	22.3	13.84	0.10	1.30	1.01	23.2	18.7	99.5				
Sample no.	Cs	Rb	Ba	Sr	Th	U	Nb	Ta	Pb	Zr	Hf	Y	La	Ce	Pr	Nd	Sm	Eu	Gd
A10	0.55	33.1	827	157	30.0	9.0	301	15.0	15	169	4.3	21.8	142.5	247.0	25.2	82.7	12.25	3.35	11.45
A8	0.83	47.4	1450	136	20.9	12.5	259	12.6	9	150	3.8	17.3	129.5	174.0	20.4	66.8	10.55	2.94	9.60
A4	0.73	59.0	3540	224	35.1	14.1	277	16.6	9	246	6.0	24.9	214.0	360.0	37.6	125.0	17.75	4.75	15.65
A6	0.33	15.6	604	147	26.5	3.3	223	18.1	4	159	4.2	11.7	108.5	198.5	20.8	66.9	9.54	2.27	8.25
A7	0.62	49.8	1125	230	33.6	9.8	165	5.6	14	174	4.2	31.0	177.0	285.0	29.8	99.0	15.65	3.96	14.15
A2	0.74	61.2	2690	161	27.0	12.5	345	17.0	16	206	5.1	21.9	150.5	227.0	24.5	79.0	12.45	3.40	11.55
A5	0.38	27.3	1020	140	53.8	10.0	268	16.8	4	151	3.9	14.0	126.0	245.0	24.5	78.8	10.85	2.76	9.95
A1	1.01	105.5	3110	194	63.2	21.4	294	15.6	4	188	4.5	19.4	189.5	324.0	32.1	104.5	13.40	3.36	11.95
A11	1.15	58.9	4040	272	105.5	25.0	291	16.0	3	253	5.9	19.8	202.0	333.0	33.3	111.0	15.40	3.91	13.30
A3	1.04	55.2	1420	150	155.0	29.2	425	21.6	9	255	6.1	21.9	243.0	391.0	39.4	127.0	16.75	4.12	14.95
A9	1.42	70.5	2050	214	75.4	29.8	331	17.9	16	240	5.1	15.9	212.0	360.0	35.4	111.0	14.35	3.61	13.15
A12	0.56	37.0	1290	159	129.5	10.8	333	18.3	4	168	5.7	33.0	237.0	424.0	42.8	135.0	17.75	4.09	16.55
B5	0.15	4.1	258	37	24.8	1.9	129	10.9	3	118	3.0	3.4	49.3	92.9	9.5	29.8	3.94	0.91	3.29
B1	0.21	6.4	135	76	35.9	3.3	155	13.6	5	118	2.9	5.0	88.6	161.5	16.7	53.5	6.30	1.41	5.64
B2	0.55	43.7	797	203	56.6	22.1	334	18.1	12	163	3.7	14.0	217.0	366.0	37.7	121.0	15.85	3.22	13.35
B3	0.29	4.8	107	205	43.1	12.0	238	16.2	6	132	3.5	8.6	153.5	266.0	26.7	82.9	9.32	1.87	8.27
B4	0.67	26.1	2740	214	81.9	24.4	396	21.9	4	176	6.5	14.0	332.0	601.0	63.4	210.0	24.00	5.35	19.70
B7	1.29	72.5	2980	146	37.0	22.6	308	17.3	7	202	5.0	20.6	178.5	288.0	31.5	101.0	13.80	3.62	13.00
B6	1.24	101.5	2620	187	74.5	58.4	304	16.6	8	245	5.6	32.8	212.0	392.0	38.4	126.0	17.15	4.37	15.80

(continued)

Table 6: Continued

Sample no.	Tb	Dy	Ho	Er	Tm	Yb	Lu	Cr	Co	Ni	V	Cu	Zn
A10	1.30	4.95	0.80	2.10	0.20	1.12	0.16	890	33.6	317	127	35	49
A8	1.09	4.07	0.68	1.71	0.16	0.87	0.12	710	32.0	363	122	24	43
A4	1.63	5.82	0.94	2.56	0.22	1.24	0.18	980	36.0	446	204	12	59
A6	0.82	3.00	0.45	1.25	0.11	0.69	0.10	1590	105.5	894	216	126	39
A7	1.59	6.52	1.08	2.86	0.28	1.50	0.23	880	27.6	294	147	33	52
A2	1.33	5.28	0.85	2.17	0.20	1.14	0.16	890	36.9	390	189	37	53
A5	1.02	3.45	0.55	1.51	0.13	0.84	0.12	1390	117.5	679	200	28	28
A1	1.25	4.45	0.73	2.12	0.22	1.27	0.18	1040	79.0	605	216	82	54
A11	1.41	5.05	0.84	2.19	0.21	1.16	0.16	1250	44.4	342	222	b.d.	37
A3	1.56	5.79	0.93	2.67	0.28	1.50	0.23	1120	31.0	710	183	26	88
A9	1.29	4.38	0.67	1.97	0.19	1.13	0.15	1200	80.1	578	267	219	72
A12	1.74	6.53	1.13	3.28	0.35	2.15	0.32	1110	130.0	647	180	67	50
B5	0.31	0.98	0.15	0.43	0.04	0.25	0.03	1230	102.0	1130	147	104	28
B1	0.53	1.50	0.22	0.64	0.04	0.34	0.04	1210	134.5	1230	165	27	25
B2	1.22	3.47	0.52	1.46	0.09	0.63	0.08	1050	109.5	381	166	7	45
B3	0.72	2.21	0.35	1.06	0.08	0.46	0.06	1610	241.0	968	149	29	47
B4	1.75	4.34	0.58	2.02	0.12	0.69	0.09	1480	171.0	946	228	31	63
B7	1.36	4.53	0.81	2.30	0.21	1.50	0.21	1010	33.7	465	225	24	51
B6	1.67	6.62	1.21	3.64	0.45	2.89	0.45	1440	41.0	430	222	24	48

Geographical coordinates and further sample information are given in Table 7 and Supplementary Data Appendix A. Major element concentrations are XRF data determined on fused lithium borate discs at ALS Chemex Laboratories (Vancouver). Trace element concentrations are ICP-MS data determined at ALS Chemex Laboratories (Vancouver). Loss on ignition (LOI) was determined by gravimetric analysis at 1000°C. CO<sub>2</sub> was liberated from the powders by reaction with HClO<sub>4</sub> and subsequently determined by photo-coulometry (lower limit of detection is 0.2 wt % CO<sub>2</sub>). Fe<sub>2</sub>O<sub>3</sub><sup>T</sup> is total Fe given as ferric iron. b.d., below detection.

discovered ~2 km to the east of Amon (Fig. 3). The kimberlite sheets were intersected by several shallow drillholes (<150 m depth) over an area of 2 km × 2 km, 25 km SW of Nina Bang Lake; here we collectively refer to these occurrences as the Amon Kimberlite Sill Complex (AKSC, Fig. 3). For our petrological and geochemical investigation of the AKSC, we recovered 19 kimberlite samples from nine drillholes (Fig. 4), two of which represent the Aliguja sill. It is important to note that no outcropping kimberlite was located in the area, but that some 400 occurrences of kimberlite float in glacial sediments were discovered during the 2006 field season alone.

All of the numerous kimberlite sheets of the subhorizontal AKSC are hosted in Neoproterozoic basement rocks that are composed of granitic gneisses with minor amphibolite rafts (images of kimberlite intersections in drillcore are shown in Supplementary Data Appendix D). The individual kimberlite sheets range in thickness between 0.2 and 1 m. Although the exact geometry of the AKSC remains unknown, modelling of the drillhole data, combined with results from shallow seismic surveys, suggests that at least two main discrete sills are present ~20–50 m beneath the

present-day land surface (Fig. 4). These kimberlite sills and associated stringers have a highly irregular shape owing to pinch-and-swell structures. However, structural modelling indicates that the undulating AKSC dips between 4 and 12° in a northerly to easterly direction (Fig. 4).

### Petrography of studied samples

The thin kimberlite sheets typically show evidence for multiple injections of magma, with fine-grained aphanitic kimberlite forming the chilled margins (<5% olivine macrocrysts; Fig. 5a) and macrocrystic varieties occupying the interior portions (>15% macrocrysts; Fig. 5d) [textural terminology follows Clement *et al.* (1984)]. These observations, along with flow alignment of prismatic minerals (Fig. 5d), point to the possibility that some of the kimberlite magma was affected by flowage differentiation and/or filter-pressing (see Kjarsgaard, 2007) (Fig. 6). A few kimberlite drillcore intersections reveal millimetre- to centimetre-sized, elongate to round segregations of carbonate (Fig. 5b; Supplementary Data Appendix D); these are similar to the carbonate 'diapirs' that have been described from the Benfontein kimberlite sills in South Africa

Table 7: *Sr–Nd–Hf isotope compositions of the Amon kimberlite sills in north-central Baffin Island, Rae craton, Arctic Canada*

Sample no.	Age (Ma)	Longitude	Latitude	$^{87}\text{Sr}/^{86}\text{Sr}_m$	$^{87}\text{Sr}/^{86}\text{Sr}_i^*$	$^{143}\text{Nd}/^{144}\text{Nd}_m$	$^{143}\text{Nd}/^{144}\text{Nd}_i^*$	$(\epsilon_{\text{Nd}})_i^\dagger$	$^{176}\text{Hf}/^{177}\text{Hf}_m$	$^{176}\text{Hf}/^{177}\text{Hf}_i^*$	$(\epsilon_{\text{Hf}})_i^\ddagger$	$\Delta\epsilon_{\text{Hf}}^i$
A10	673	-80-217009	70-697465	0.713195(13)	0.70732	0.512244(9)	0.51185	1.6	0.282533(4) <sup>1</sup>	0.282468	3.8	0.0
A8	673	-80-217009	70-697465	0.713993(19)	0.70454	0.512337(3)	0.51191	2.9	0.282518(13)	0.282463	3.6	-2.3
A4	673	-80-217009	70-697465	0.712681(19)	0.70554	0.512321(6)	0.51194	3.4	0.282568(12)	0.282515	5.5	-1.3
A6	673	-80-217009	70-697465	0.709148(26)	0.70627	0.512272(3)	0.51189	2.4	0.282594(6) <sup>1</sup>	0.282552	6.8	1.6
A7	673	-80-217009	70-697465	n.a.		n.a.			n.a.			
A2	673	-80-217009	70-697465	n.a.		0.512264(7)	0.51184	1.5	0.282565(5) <sup>1</sup>	0.282510	5.3	1.6
A5	673	-80-217009	70-697465	0.711846(16)	0.70654	0.512305(3)	0.51194	3.3	0.282628(9) <sup>1</sup>	0.282574	7.6	1.0
A1	673	-80-212375	70-697428	0.719489(20)	0.70474	0.512286(5)	0.51194	3.5	0.282531(7) <sup>1</sup>	0.282461	3.5	-3.2
A11	673	-80-212375	70-697428	0.712683(20)	0.70681	0.512307(6)	0.51194	3.3	0.282654(12)	0.282606	8.7	2.1
A3	673	-80-212375	70-697428	0.713980(19)	0.70400	0.512275(4)	0.51192	3.1	0.282496(5) <sup>1</sup>	0.282430	2.5	-3.7
A9	673	-80-212375	70-697428	0.712511(21)	0.70358	0.512277(2)	0.51193	3.2	0.282504(9) <sup>1</sup>	0.282452	3.3	-3.2
A12	673	-80-212338	70-695616	0.712030(17)	0.70572	0.512223(3)	0.51187	2.1	0.282549(14)	0.282450	3.2	-1.4
B5	673	-80-215146	70-697426	0.707456(23)	0.70443	0.512250(4)	0.51190	2.5	0.282606(5) <sup>1</sup>	0.282588	8.1	2.7
B1	673	-80-215146	70-697426	0.706159(18)	0.70386	0.512165(4)	0.51185	1.7	0.282561(4) <sup>1</sup>	0.282537	6.2	2.3
B2	673	-80-215146	70-697426	0.709459(17)	0.70362	0.512246(6)	0.51190	2.5	0.282429(4) <sup>1</sup>	0.282391	1.1	-4.2
B3	673	-80-215141	70-69744	0.704684(21)	0.70405	0.512209(4)	0.51191	2.8	0.282541(7) <sup>1</sup>	0.282511	5.3	-0.4
B4	673	-80-215141	70-69744	0.711056(24)	0.70775	0.512226(6)	0.51192	3.0	0.282586(11)	0.282562	7.1	1.0
B7	673	-80-157989	70-698917	0.718698(16)	0.70519	0.512299(3)	0.51193	3.3	0.282562(10)	0.282488	4.5	-3.1
B6	673	-80-157989	70-698917	0.719626(19)	0.70487	0.512247(2)	0.51188	2.3	0.282608(8) <sup>1</sup>	0.282467	3.8	-1.1

Sr isotope compositions were determined by TIMS, and Nd and Hf isotope compositions were determined by MC-ICP-MS at the University of Alberta, except for Hf isotope data with superscript '1' (Durham University). Measured Sr, Nd, and Hf isotope ratios are normalized to the following standard values: NBS987 =  $^{87}\text{Sr}/^{86}\text{Sr}$  value of 0.710243 (Thirlwall, 1991); ALFA =  $^{143}\text{Nd}/^{144}\text{Nd}$  value of 0.512265, equivalent to the La Jolla  $^{143}\text{Nd}/^{144}\text{Nd}$  value of 0.51185; JMC475 =  $^{176}\text{Hf}/^{177}\text{Hf}$  value of 0.28216 (Blichert-Toft *et al.*, 1997). Average standard values obtained during this study are: NBS987 =  $^{87}\text{Sr}/^{86}\text{Sr}$  value of  $0.710233 \pm 8$  (2SD;  $n=57$ ); ALFA =  $^{143}\text{Nd}/^{144}\text{Nd}$  value of  $0.512284 \pm 23$  (2SD;  $n=17$ ); JMC475 =  $^{176}\text{Hf}/^{177}\text{Hf}$  value of  $0.282157 \pm 8$  (2SD;  $n=3$ ; Alberta) and  $0.282156 \pm 6$  (2SD;  $n=8$ ; Durham); JNdi-1 =  $^{143}\text{Nd}/^{144}\text{Nd}$  value of  $0.512091 \pm 8$  (2SD;  $n=5$ ); BHVO-1 =  $^{143}\text{Nd}/^{144}\text{Nd}$  value of  $0.512984 \pm 11$  (2SD;  $n=3$ ) and  $^{176}\text{Hf}/^{177}\text{Hf}$  value of  $0.283104 \pm 8$  (2SD;  $n=6$ ).  $\Delta\epsilon_{\text{Hf}}$  is defined as  $\epsilon_{\text{Hf}} - (1.59\epsilon_{\text{Nd}} + 1.28)$ , such that samples with negative values fall by definition below the mantle Nd–Hf isotope array of Chauvel *et al.* (2008). Numbers in parentheses are  $2\sigma$  of the mean uncertainties for single isotope ratio measurements; Geographic coordinates are in decimal degrees using WGS84 datum. n.a., not analyzed.

\*Initial isotope ratios calculated for the emplacement age of 673 Ma of the Amon kimberlite sills (this study).

<sup>†</sup>Initial  $\epsilon_{\text{Nd}}$  values were calculated using  $^{147}\text{Sm}$  decay constant of  $6.54 \times 10^{-12} \text{ a}^{-1}$  (Lugmair & Marti, 1978);  $(^{143}\text{Nd}/^{144}\text{Nd})_{\text{CHUR}} = 0.512630$  and  $(^{147}\text{Sm}/^{144}\text{Nd})_{\text{CHUR}} = 0.1960$  (Bouvier *et al.*, 2008).

<sup>‡</sup>Initial  $\epsilon_{\text{Hf}}$  values were calculated using  $^{176}\text{Lu}$  decay constant of  $1.865 \times 10^{-11} \text{ a}^{-1}$  (Scherer *et al.*, 2001);  $(^{176}\text{Hf}/^{177}\text{Hf})_{\text{CHUR}} = 0.282785$  and  $(^{176}\text{Lu}/^{177}\text{Hf})_{\text{CHUR}} = 0.0336$  (Bouvier *et al.*, 2008).

(Dawson & Hawthorne, 1973). The carbonate segregations resemble experimentally produced immiscibility textures (Brooker & Kjarsgaard, 2011).

Common macrocryst phases are olivine, phlogopite, pyrope-rich garnet, and picro-ilmenite (listed in order of decreasing abundance) that rarely exceed 5 mm in the longest dimension (Figs 5a, d and 6a). Olivine is the most abundant phenocryst phase and typically forms euhedral prisms up to 2 mm in length (Fig. 6b and c). The olivine is completely replaced by carbonate and serpentine or iddingsite (Figs 5c, d and 6a–c). The kimberlite groundmass consists of phlogopite, spinel, ilmenite, and apatite

microphenocrysts (<100  $\mu\text{m}$ ) in a matrix of calcite, with rare serpentine plus secondary quartz. Rutile is a common primary groundmass phase and has also been found replacing ilmenite (Fig. 6d), and possibly perovskite. In general, rutile is more stable than perovskite in  $\text{CO}_2$ -rich systems (Mitchell & Chakhmouradian, 1998), which explains its predominance over and reaction relationship with other titanates in the very carbonate-rich Amon kimberlites. Rutile furthermore forms overgrowths on ilmenite macrocrysts (Fig. 6d) and groundmass spinels. Monticellite, clinopyroxene, and perovskite are conspicuously absent in the Amon kimberlite groundmass, as also

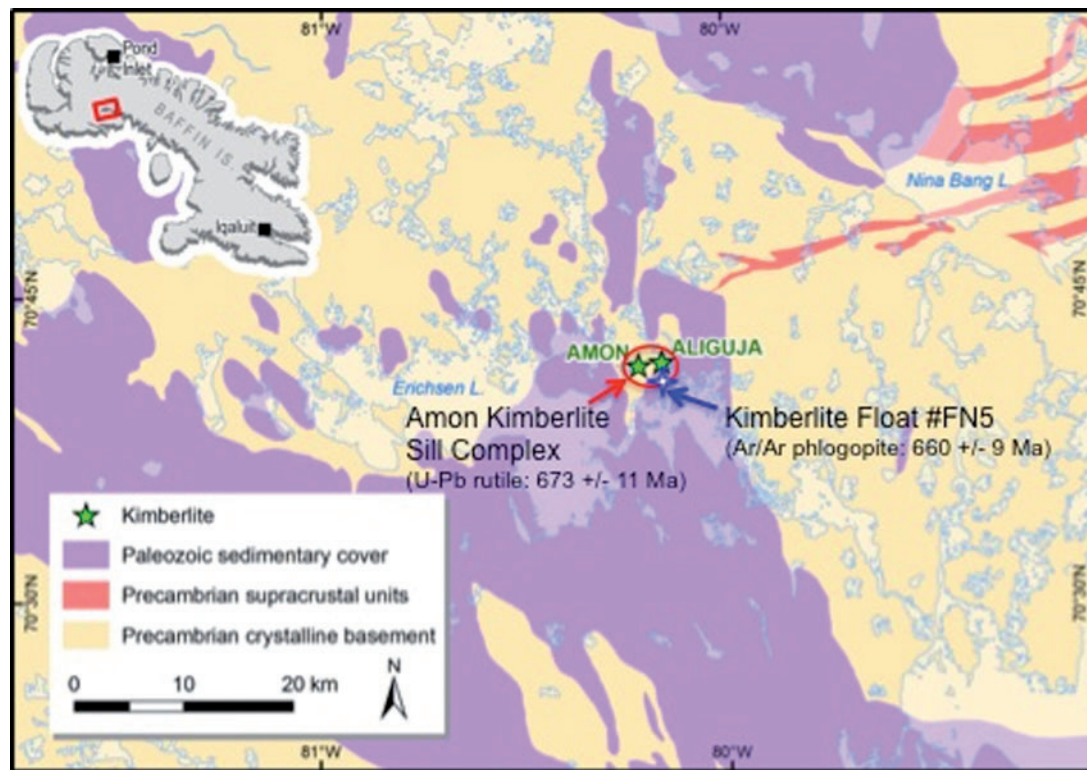


**Fig. 3.** Geological map of the barren vicinity of the Amon Kimberlite Sill Complex (AKSC) in north-central Baffin Island, Rae craton, Canadian–Greenland shield. The U–Pb rutile age data for an *in situ* kimberlite sheet of the AKSC are provided in Table 1. The location of kimberlite float sample FN5, *c.* 2 km down ice flow direction from the AKSC, is shown, and the  $^{40}\text{Ar}/^{39}\text{Ar}$  phlogopite age results are provided in Table 2.

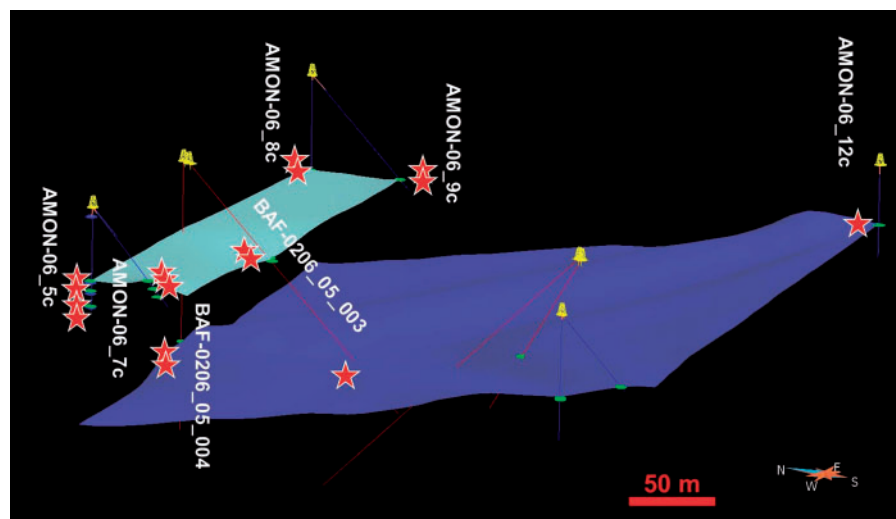


**Fig. 4.** Geological model of the Amon Kimberlite Sill Complex (without the Aliguja sill segment ~2 km to the east; see Fig. 3) based on the surfaces of kimberlite intersections in drillholes (highlighted in green). The modelling results show that at least two main discrete kimberlite sheets are present ~20–50 m beneath the present-day land surface, and structural data indicate that the undulating sill complex dips between 4 and 12° towards a northerly to easterly direction. The approximate positions of kimberlite samples investigated during this study are indicated with red stars at the respective drillholes (note that the two samples derived from one drillhole in the Aliguja sill segment are not shown).



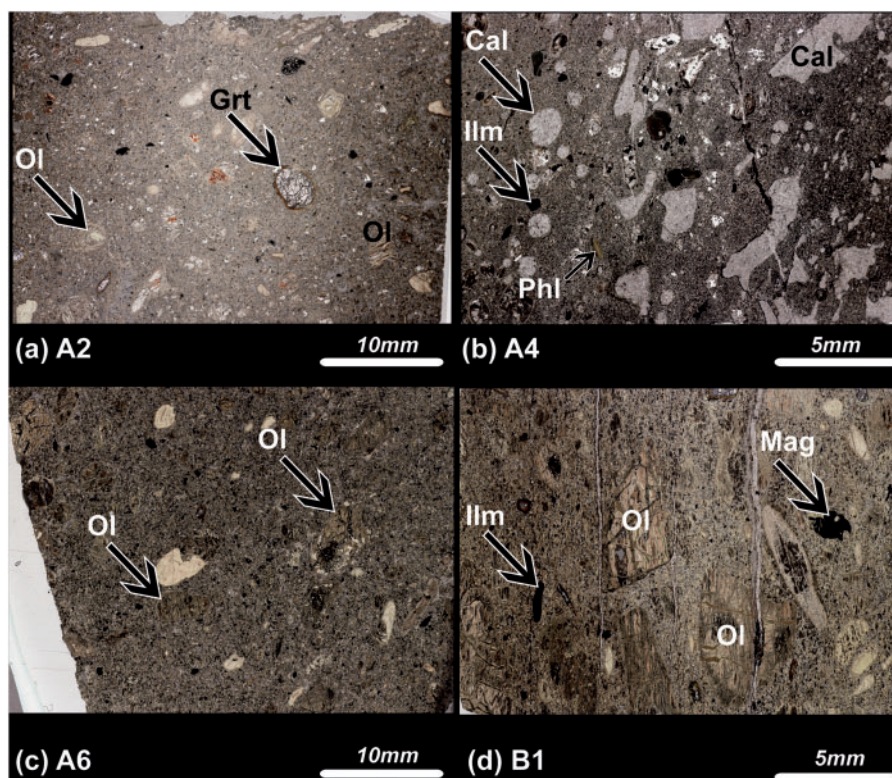


**Fig. 5.** Photomicrographs of representative kimberlite samples from the Amon sills. Detailed drillhole and sample information is provided in Tables 6 and 7 and Fig. 4. Mineral abbreviations are according to the scheme of Kretz (1983). (a) Sample A2 from drillhole AMON-06-007C shows an aphanitic to weakly macrocrystic texture with less than 10 vol. % serpentinized olivine macrocrysts. The partially kelyphitized garnet macrocryst (arrow) should also be noted. (b) Sample A4 from drillhole AMON-06-005C shows millimetre-sized elongate to round calcite segregations in an otherwise aphanitic to weakly macrocrystic kimberlite sheet. The rare phlogopite macrocryst in the bottom left corner of the image (arrow) should be noted. (c) Sample A6 from drillhole AMON-06-005C shows a relatively homogeneous, weakly macrocrystic texture with less than 15 vol. % subangular to subrounded serpentinized olivine macrocrysts (arrows). (d) Sample B1 from drillhole BAF-0206-05-003 shows a macrocrystic texture with abundant subangular to subrounded serpentinized olivine macrocrysts. The preferential alignment of elongate olivine and ilmenite macrocrysts (arrow) should be noted; this suggests that flow differentiation had occurred during subhorizontal kimberlite magma emplacement.

described from the hypabyssal facies of numerous other kimberlite occurrences worldwide (Clement *et al.*, 1984; Mitchell, 1995).

## ANALYTICAL TECHNIQUES

### Geochronology

#### *U–Pb rutile*

A hand specimen of kimberlite sheet B1, intersected in drillhole BAF-0206-05-003 between 42.35 and 42.50 m depth (Fig. 4), was processed through standard crushing and mineral separation procedures (e.g. Wilfley table, methylene iodide, Frantz isodynamic separator) at the University of Alberta. These procedures are identical to the steps typically employed during liberation and concentration of groundmass perovskite from kimberlite samples as outlined by Heaman & Kjarsgaard (2000) and Tappe *et al.* (2012b). In the mesh range between 20 and 200  $\mu\text{m}$ , two fresh but visually distinct rutile populations

of similar grain size between 50 and 100  $\mu\text{m}$  were observed. Approximately 80 (B1-1) and 100 (B1-2) grains without visible inclusions were collected from these two populations as morphologic fractions, which yielded  $67 \pm 1$  and  $101 \pm 8$   $\mu\text{g}$  rutile aliquots (Table 1). Fraction B1-1 comprised bright orange euhedral to subhedral rutile grains, whereas B1-2 consisted of orange to yellow fragments of a coarser rutile population that was most probably comminuted during sample treatment (e.g. Fig. 6d).

The collected rutile grains were washed repeatedly in warm 2N  $\text{HNO}_3$  and Milli-Q water and then weighed on an ultra-microbalance prior to transfer into 5 ml Savillex vials. Prior to sample dissolution in a 1:1 mixture of concentrated HF and  $\text{HNO}_3$  on a hotplate at *c.* 160°C for 5 days,  $^{235}\text{U}$ – $^{205}\text{Pb}$  tracer solution was added to the rutile–acid mix to determine U and Pb concentrations by isotope dilution. Thorium concentrations were calculated based on the amount of common lead corrected  $^{208}\text{Pb}$  present and the  $^{207}\text{Pb}/^{206}\text{Pb}$  model age.



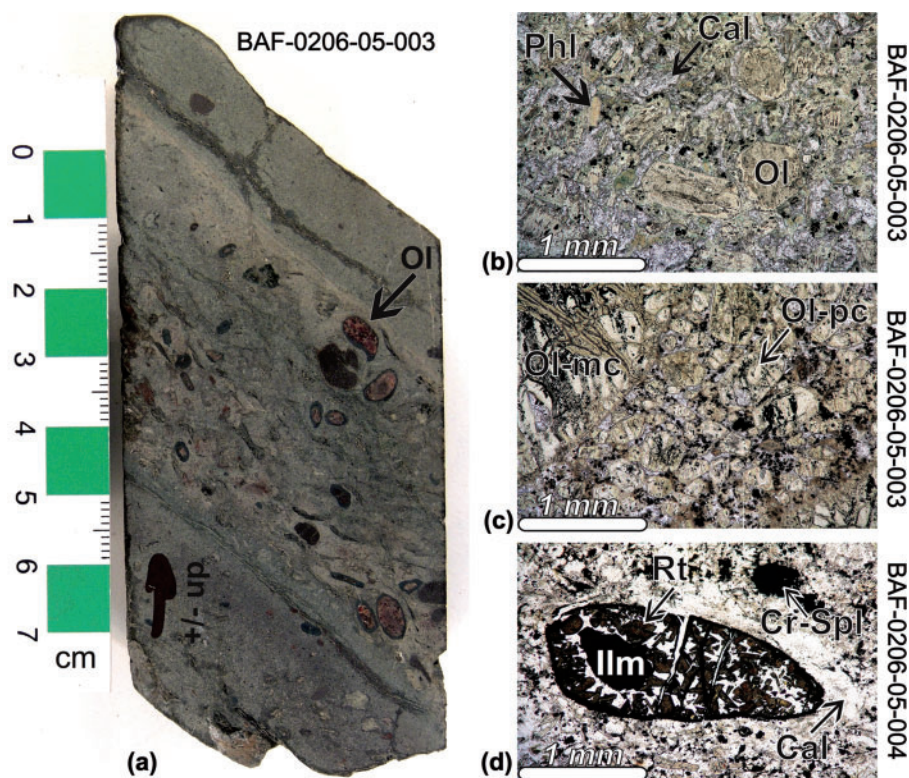


**Fig. 6.** Polished rock slab (a) and detailed photomicrographs (b–d) of representative kimberlite samples from the Amon sills. Drillhole and sample information is provided in Tables 6, 7 and Fig. 4. Mineral abbreviations are according to the scheme of Kretz (1983). (a) Polished slab sample from drillhole BAF-0206-05-003 in an approximately upright orientation. The sample is characterized by an upper and lower aphanitic kimberlite variety, whereas a weakly macrocrystic kimberlite variety with less than 10 vol. % serpentinized and iddingsitized olivine macrocrysts (black arrow) occupies the central portion. (b) Thin section photomicrograph (plane-polarized light; PPL) of Amon kimberlite from drillhole BAF-0206-05-003. Euhedral to subhedral serpentinized olivine phenocrysts and microphenocrysts are set in a matrix of calcite, phlogopite, and fine-grained spinel. (c) Thin section photomicrograph (PPL) of Amon kimberlite from drillhole BAF-0206-05-003. The sample is derived from the same kimberlite sheet as in (b) but exhibits significantly higher modal abundances of phenocrystic and macrocrystic olivine. The primary carbonate–phlogopite matrix (residual melt?) has largely been removed by filter-pressing. (d) Thin section photomicrograph (PPL) of Amon kimberlite from drillhole BAF-0206-05-004. A picro-ilmenite macrocryst is almost completely replaced by groundmass rutile and calcite, whereas an adjacent Cr-spinel microphenocryst is intact; that is, it does not show any reaction relationship with residual melt, or groundmass.

Uranium and Pb were isolated from the rutile sample solutions using HBr anion exchange chromatography (Bio-Rad AG 1-X8). The isotopic compositions of these elements were measured on a VG354 thermal ionization mass spectrometer using a Daly detector operated in analog mode. All isotopic data reported in Table 1 were corrected for mass discrimination (0.105% per a.m.u. Pb and 0.123% per a.m.u. U; determined using the long-term reproducibility of NBS 981 and NBS U500, respectively), tracer, and blank contribution ( $5 \pm 0.5$  pg Pb and  $1.0 \pm 0.1$  pg U). The presence of an ~56–58% proportion of common lead was corrected using the terrestrial lead evolution model of Stacey & Kramers (1975).

For the rutile fractions analysed during this study we report the  $^{206}\text{Pb}/^{238}\text{U}$  ages, because they are less sensitive to the initial common lead correction compared with  $^{207}\text{Pb}/^{206}\text{Pb}$  and  $^{207}\text{Pb}/^{235}\text{U}$  ages (Davis, 1997; Li *et al.*, 2003; Zack *et al.*, 2011). The age calculations were

performed with the Isoplot software (Ludwig, 2000) utilizing the recommended decay constants of  $9.8485 \times 10^{-10} \text{ a}^{-1}$  for  $^{235}\text{U}$  and  $1.55125 \times 10^{-10} \text{ a}^{-1}$  for  $^{238}\text{U}$  (Steiger & Jäger, 1977). All uncertainties are quoted at the  $2\sigma$  level throughout the text.

#### $^{40}\text{Ar}/^{39}\text{Ar}$ phlogopite

A hand specimen of kimberlite boulder FN5 (302/616/0001), which was discovered by De Beers Canada Inc. during early exploration in 2002 *c.* 2 km south of the now confirmed AKSC occurrence (i.e. down ice flow; Fig. 3), was processed through standard crushing and mineral separation procedures at the University of Melbourne. A phlogopite mineral separate was washed in deionized water and acetone prior to being shipped for irradiation. The grains were wrapped in an aluminium packet and placed into an aluminium irradiation canister together with aliquots of the flux monitor GA1550 (age =  $98.8 \pm 0.5$

Ma; Renne *et al.*, 1998). Packets containing  $\text{K}_2\text{SO}_4$  were placed at either end of the canister to monitor  $^{40}\text{Ar}$  production from potassium. The irradiation canister was irradiated in position 5C of the McMaster reactor, Hamilton, Ontario, Canada. After irradiation, the phlogopite grains were removed from their packaging and loaded into a copper sample holder. The grains were then each step-heated using a CW Nd:YAG laser at the University of Melbourne.  $^{40}\text{Ar}/^{39}\text{Ar}$  analyses were carried out on a MM5400 mass spectrometer using a Daly detector [for details see Phillips & Harris (2009)]. Mass discrimination was monitored by analyses of standard air volumes. Correction factors for interfering reactions are as follows:  $(^{36}\text{Ar}/^{37}\text{Ar})_{\text{Ca}} = 2.63 (\pm 0.01) \times 10^{-4}$ ;  $(^{39}\text{Ar}/^{37}\text{Ar})_{\text{Ca}} = 6.86 (\pm 0.03) \times 10^{-4}$ ;  $(^{40}\text{Ar}/^{39}\text{Ar})_{\text{K}} = 0.0015 (\pm 0.007)$ . The Ca/K ratios were calculated according to the relation  $1.9 \times ^{39}\text{Ar}/^{37}\text{Ar}$ .

The reported data in Table 2 have been corrected for system backgrounds, mass discrimination, fluence gradients, and atmospheric contamination. The analytical uncertainties associated with the argon age determinations exclude uncertainties in the J-value, age of the fluence monitor GA1550, and the decay constants.  $^{40}\text{Ar}/^{39}\text{Ar}$  ages have been calculated using two sets of decay constants and standards: those of Steiger & Jäger (1977) and Renne *et al.* (1998), and those of Renne *et al.* (2010, 2011). In general,  $^{40}\text{Ar}/^{39}\text{Ar}$  ages calculated using the constants and standard values that are recommended by Renne *et al.* (2010, 2011) are considered to be most consistent with U–Pb age systematics.

### Mineral compositions

Major element mineral compositional data were obtained using a JEOL JXA 8900 electron microprobe at the University of Alberta, Canada [for details see Tappe *et al.* (2009)]. Operating voltage for oxide mineral analysis was 20 kV with a beam current of 20 nA, and for phlogopite analysis 15 kV and 15 nA, respectively. Counting time varied between 30 and 50 s on the peak and a beam diameter between 2 and 5  $\mu\text{m}$  was adjusted. International standards of natural materials were used for calibration and all data reported in Tables 3–5 were reduced with a CITZAF procedure.

### Bulk-rock major and trace element compositions

Each sample powder (<20  $\mu\text{m}$  grain size) was prepared in an agate mill at the University of Alberta from ~500 g of hand-selected rock chips (i.e. the freshest kimberlite drill-core material available from the various intersections of the AKSC; Fig. 4; Supplementary Data Appendix D). The powders were supplied for analyses to the ALS Chemex Laboratory Group at their Vancouver facility in Canada [for details see Tappe *et al.* (2011)]. Major element concentrations were determined by X-ray fluorescence (XRF)

on fused glass discs ( $\text{Li}_2\text{B}_4\text{O}_7$ – $\text{LiBO}_2$  flux), with a lower limit of detection <0.01 wt % for all elements analyzed. Rare earth elements (REE) and other trace elements (e.g. Nb, Th, U) were analysed by inductively coupled plasma mass spectrometry (ICP-MS) after  $\text{LiBO}_2$  fusion and dissolution in mixed  $\text{HNO}_3$ – $\text{HCl}$ . Volatiles were determined by a combination of loss on ignition (corrected for the conversion of  $\text{FeO}$  to  $\text{Fe}_2\text{O}_3$ ) and analyses of  $\text{CO}_2$  that was liberated from the powders by reaction with  $\text{HClO}_4$  and subsequently determined by photo-coulometry (lower limit of detection is 0.2 wt %  $\text{CO}_2$ ) (Table 6).

### Bulk-rock Sr–Nd–Hf isotope compositions

Isotope compositions (Table 7) were determined on the same bulk-rock powders as the major and trace element concentrations (Table 6). Powders were digested in a  $\text{HF}$ – $\text{HNO}_3$  mixture in Savillex beakers on a hotplate for 5 days. Subsequently, the  $\text{HF}$ – $\text{HNO}_3$  mixture was gently evaporated to incipient sample dryness. The sample material was then taken up in 6N  $\text{HCl}$  and heated again until a clear solution was obtained (i.e. for 2–4 days). Sample digestion tests on kimberlitic and carbonatitic material were previously conducted in both Savillex beakers and Teflon bombs, and duplicate Hf isotope analyses from these tests have been given by Tappe *et al.* (2007, 2008). These tests demonstrate that complete sample dissolution is also achieved by the powder digestion procedure using Savillex beakers, because the measured Hf isotope compositions of duplicate pairs are identical within analytical uncertainty. In general, reproducibilities from replicate dissolutions of kimberlites analysed by Nowell *et al.* (2004) and Tappe *et al.* (2013a) are better than 0.7 epsilon Hf units. At the University of Alberta, Sr–Nd–Hf cuts were separated using a combination of cation and anion exchange resins (Schmidberger *et al.*, 2007; Tappe & Simonetti, 2012). The cuts were measured for their isotope compositions using both thermal ionization mass spectrometry (TIMS) (Sr) and multicollector (MC)-ICP-MS (Nd and Hf) techniques in Alberta. A subset of sample powders ( $n=12$ ) was analyzed for Hf isotope compositions at Durham University following the procedures outlined by Nowell *et al.* (2004) and Tappe *et al.* (2013a).

Strontium isotopic analyses were performed by TIMS using a Micromass Sector-54 system operating in static mode (single Re filaments). The reported  $^{87}\text{Sr}/^{86}\text{Sr}$  values in Table 7 consist of at least 240 isotope ratio measurements corrected for mass fractionation using an exponential law and  $^{86}\text{Sr}/^{88}\text{Sr} = 0.1194$ . NIST SRM 987 yielded an average value for  $^{87}\text{Sr}/^{86}\text{Sr}$  of  $0.710233 \pm 8$  ( $2\sigma$  SD for 57 measurements) during the measurement period (November 2009 to December 2010) and all measured Sr isotopic ratios are reported relative to a value of 0.710243 for NIST SRM 987 (Thirlwall, 1991).

The Nd isotopic compositions were analysed by MC-ICP-MS on a Nu Plasma instrument in static mode and

all isotope ratios were corrected with an exponential fractionation law using  $^{146}\text{Nd}/^{144}\text{Nd} = 0.7219$ . The reported  $^{143}\text{Nd}/^{144}\text{Nd}$  values in Table 7 consist of 60 isotope ratio measurements. The in-house Alfa Nd isotope standard (200 ppb solution) was run repeatedly during the analytical sessions with an average  $^{143}\text{Nd}/^{144}\text{Nd}$  value of  $0.512284 \pm 23$  ( $2\sigma$  SD for 17 measurements). This value overlaps with the 7 year average of  $0.512255 \pm 48$  ( $2\sigma$  SD for 394 measurements). All measured Nd isotopic ratios are reported relative to a value of 0.512265 for the Alfa standard. The mean average  $^{143}\text{Nd}/^{144}\text{Nd}$  for the Shin Etsu Nd standard (JNdi-1), which was run as a secondary standard, yielded  $0.512091 \pm 8$  ( $2\sigma$  SD for five measurements). This is in agreement with the 1 year average of  $0.512104 \pm 27$  ( $2\sigma$  SD for 22 measurements) and with the recommended value of 0.512107 (Tanaka *et al.*, 2000).

In Alberta, the Hf isotopic compositions were analysed by MC-ICP-MS on a Nu Plasma instrument in static mode, and all isotope ratios were corrected with an exponential fractionation law using  $^{179}\text{Hf}/^{177}\text{Hf} = 0.7325$ . The reported  $^{176}\text{Hf}/^{177}\text{Hf}$  values in Table 7 consist of 60 isotope ratio measurements. A 50 ppb solution of the JMC-475 standard was run repeatedly during the analytical session with an average  $^{176}\text{Hf}/^{177}\text{Hf}$  value of  $0.282157 \pm 8$  ( $2\sigma$  SD for three measurements). In Durham, Hf samples were taken up in 0.5 ml 3%  $\text{HNO}_3$ –1N HF and were introduced into a Thermo Fisher Neptune MC-ICP-MS instrument using an ESI PFA50 nebulizer together with a Cetac Aridus desolvator. Instrumental mass bias was corrected for using a  $^{179}\text{Hf}/^{177}\text{Hf}$  ratio of 0.7325 and an exponential law. Corrections for the isobaric interferences from Yb and Lu on  $^{176}\text{Hf}$  were made by monitoring  $^{172-173}\text{Yb}$  and  $^{175}\text{Lu}$ . In practice, the average  $^{176}\text{Yb}/^{177}\text{Hf}$  and  $^{176}\text{Lu}/^{177}\text{Hf}$  ratios obtained on the samples were 0.0002 and 0.000005, respectively, so the necessary corrections were negligible. The samples were analyzed in a single session during which the JMC-475 standard gave an average value of  $0.282156 \pm 6$  ( $2\sigma$  SD for eight measurements). All sample data (Alberta and Durham) are reported relative to the accepted value of 0.282160 for JMC-475 (Blichert-Toft *et al.*, 1997).

Procedural blanks of <60 pg Sr, <30 pg Nd, and <15 pg Hf are considered negligible given the elevated concentrations of these elements in the samples analysed (Table 6). The initial Sr, Nd, and Hf isotopic compositions of the Amon kimberlite samples were calculated for an emplacement age of 673 Ma (see Tables 1 and 7) applying Rb/Sr, Sm/Nd, and Lu/Hf ratios that were obtained from ICP-MS trace element analyses. The following decay constants were used for age corrections of tracer isotope ratios:  $^{87}\text{Rb}$   $1.42 \times 10^{-11} \text{ a}^{-1}$  (Steiger & Jäger, 1977);  $^{147}\text{Sm}$   $6.54 \times 10^{-12} \text{ a}^{-1}$  (Lugmair & Marti, 1978);  $^{176}\text{Lu}$   $1.865 \times 10^{-11} \text{ a}^{-1}$  (Scherer *et al.*, 2001).

## RESULTS

Our results for the Amon kimberlites regarding their geochronology (Tables 1 and 2), mineral chemistry (Tables 3–5), and geochemistry (Tables 6 and 7), including Sr–Nd–Hf isotope compositions, are fully available online in Supplementary Data Appendix A (all Tables) and Appendix B (extended microprobe dataset for phlogopite, spinel, and ilmenite–rutile).

### Amon kimberlite emplacement ages

#### U–Pb rutile

Two translucent, orange to yellow rutile fractions from an ~0.2 m thick kimberlite sheet (BAF-0206-05-003; 42.35–42.50 m depth; Fig. 4) were analyzed by conventional isotope dilution (ID)-TIMS (Table 1). These multi-grain fractions yielded indistinguishable  $^{206}\text{Pb}/^{238}\text{U}$  ages of  $673.5 \pm 15.0$  Ma and  $671.9 \pm 15.4$  Ma, which allowed calculation of a weighted average age of  $672.7 \pm 10.6$  Ma ( $2\sigma$ ). Based on textural observations (e.g. Fig. 6d), we interpret the analyzed rutile as a primary phase and the determined U–Pb age of  $c. 673 \pm 11$  Ma is considered here the currently best estimate of kimberlite magma emplacement in north-central Baffin Island. This interpretation is supported by rutile compositional data such as elevated Fe content (Table 5) and high Th/U ratios of ~3.5 (Table 1), which are indicative of elevated (i.e. magmatic) crystallization temperatures (Zack *et al.*, 2011). The unusually high Th/U of the kimberlitic rutile also points to a complete absence of coexisting perovskite during magmatic crystallization, because the latter phase would have preferentially incorporated the available Th into its lattice [compare Klemme *et al.* (2005) with Beyer *et al.* (2013)]. This inference is supported by the growing database of kimberlitic perovskite compositions, which shows that the vast majority have high Th/U ratios between two and 200 [see compilation by Wu *et al.* (2010)].

#### $^{40}\text{Ar}/^{39}\text{Ar}$ phlogopite

A total of seven groundmass phlogopite grains were analysed from sample FN5 (302/616/0001; Fig. 3). Grain FN5/1 was fused in a single step, whereas the remaining grains were step-heated in two to three increments (Table 2). Calculated apparent ages range from  $347 \pm 8$  Ma to  $688 \pm 4$  Ma [decay constants and standard ages after Renne *et al.* (2010, 2011)]. In all instances the lowest temperature steps yielded younger ages ( $347 \pm 8$  Ma to  $552 \pm 7$  Ma) than the high-temperature fusion experiments owing to alteration-induced  $^{40}\text{Ar}$  loss (i.e. minor chlorite alteration was observed along fractures and the rims of phlogopite grains). The high-temperature steps are reasonably concordant, with a weighted average age of  $666 \pm 12$  Ma ( $2\sigma$ ; MSWD = 8.1;  $n = 7$ ). Exclusion of the oldest apparent age from grain FN5/3 gives a more precise weighted



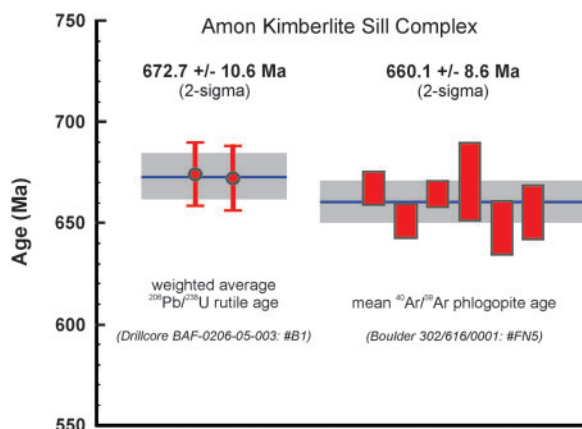


**Fig. 7.** Summary of the radiometric age determinations for the Amon Kimberlite Sill Complex (AKSC) in north-central Baffin Island (data are listed in Tables 1 and 2). The U–Pb rutile age of  $672.7 \pm 10.6$  Ma that was determined on a piece of kimberlite drillcore is our best estimate of the timing of kimberlite magma emplacement in north-central Baffin Island. This U–Pb age is identical within analytical uncertainty to the  $^{40}\text{Ar}/^{39}\text{Ar}$  phlogopite age of  $660.1 \pm 8.6$  Ma that was determined for a kimberlite boulder recovered 2 km to the south (i.e. down the ice flow direction) of the now confirmed AKSC occurrence (Fig. 3).

average age of  $660.1 \pm 8.6$  Ma ( $2\sigma$ ; MSWD = 2.9;  $n = 6$ ) (Fig. 7).

The  $^{40}\text{Ar}/^{39}\text{Ar}$  groundmass phlogopite age of  $660.1 \pm 8.6$  Ma ( $2\sigma$ ) for the kimberlite float is in good agreement with the U–Pb rutile age of  $672.7 \pm 10.6$  Ma ( $2\sigma$ ) (Fig. 7). The U–Pb rutile age was determined on a piece of drillcore of *in situ* kimberlite and appears to be more robust than the  $^{40}\text{Ar}/^{39}\text{Ar}$  phlogopite age derived from the float sample. Hence,  $673 \pm 11$  Ma is considered here the currently best estimate of kimberlite magma emplacement in north-central Baffin Island. However, the possibility of a wider age span of Late Neoproterozoic kimberlite magmatic activity in northern Baffin Island (i.e. up to 50 Myr duration as in West Greenland; Tappe *et al.*, 2012b) cannot be ruled out based on the limited geochronology data reported herein.

## Amon kimberlite mineralogy

### Phlogopite

Rare phlogopite macrocrysts are typically chloritized such that high-quality microprobe analysis was not possible. Groundmass phlogopite compositions of the Amon kimberlites show strong  $\text{Al}_2\text{O}_3$  and BaO enrichment (up to 20 and 9 wt %, respectively), and  $\text{TiO}_2$  depletion (down to 0.4 wt %) toward the rims (Fig. 8). Furthermore, the groundmass phlogopites have core compositions that are characterized by low to moderate  $\text{TiO}_2$  (0.4–4.0 wt %) and elevated  $\text{Cr}_2\text{O}_3$  contents (up to 1.6 wt %). The F content of groundmass phlogopite is slightly elevated and ranges between 0.2 and 0.8 wt % in the cores, and up to 1.4 wt % F in Ba-rich rims (Table 3). These features,

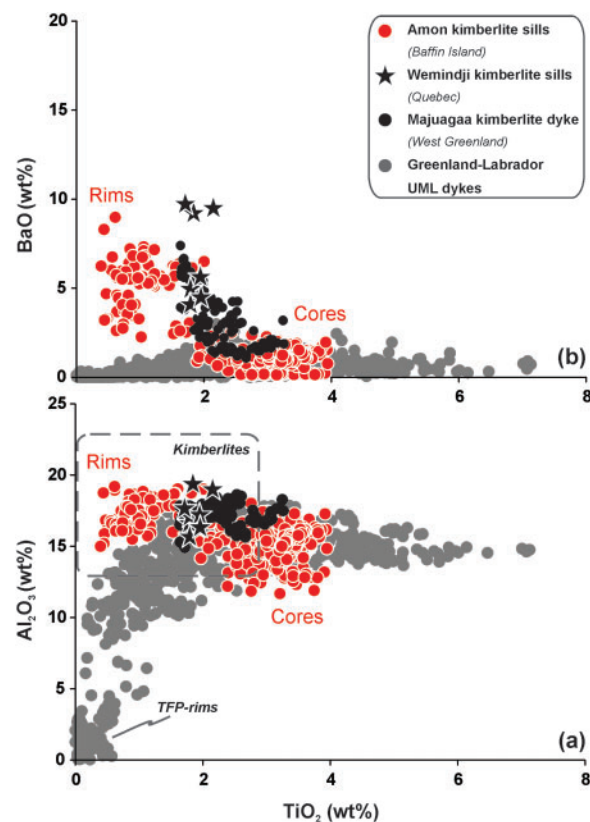


**Fig. 8.** Groundmass phlogopite compositions from the Amon kimberlites in north-central Baffin Island compared with their analogs from various Late Neoproterozoic kimberlites and related rocks of eastern Laurentia (see Fig. 2). (a)  $\text{Al}_2\text{O}_3$  vs  $\text{TiO}_2$  (wt %) variation of groundmass phlogopite. It should be noted that despite slightly elevated  $\text{TiO}_2$  concentration levels in some phlogopite cores, the overall evolutionary trend is toward Ti depletion and Al enrichment, which is typical for Group-I kimberlites. Also noteworthy is the absence of zoning trends toward tetraferriphlogopite (TFP) compositions, which are diagnostic for UMLs and Group-II kimberlites or orangite–lamproites (Mitchell, 1995; Tappe *et al.*, 2005). (b) BaO vs  $\text{TiO}_2$  (wt %) variation in groundmass phlogopite. The pronounced Ba enrichment in phlogopite rims from the Amon kimberlites, which is diagnostic for Group-I kimberlites but uncommon in UMLs and lamproites, should be noted (Mitchell, 1995; Tappe *et al.*, 2005). Data from the Wemindji kimberlite sills (Zurevinski & Mitchell, 2011) and Majuagaa calcite kimberlite dyke (Nielsen & Sand, 2008), as well as the ‘kimberlite box’ (Mitchell, 1995), are shown for comparison. The phlogopite compositional range of Late Neoproterozoic Greenland–Labrador UML dykes was compiled from data given by Tappe *et al.* (2004, 2006, 2008) and Nielsen *et al.* (2009). TFP, tetraferriphlogopite.

together with the conspicuous absence of tetraferriphlogopite rims (Fig. 8), are diagnostic for archetypal or Group-I kimberlites worldwide (Mitchell, 1995; Tappe *et al.*, 2005). Groundmass phlogopite compositions of the Amon kimberlites resemble their analogs from other Late Neoproterozoic kimberlites of Laurentia (Fig. 2) such as the Wemindji sills in Quebec (Zurevinski & Mitchell, 2011) and the Majuagaa dyke in West Greenland (Nielsen & Sand, 2008). Importantly, the Amon phlogopite compositions follow evolutionary trends that are distinctively

different from those observed in groundmass phlogopites of UMLs (aillikites) and associated carbonatites of the neighbouring 610–550 Ma Greenland–Labrador Diamond Province (Fig. 8) (Tappe *et al.*, 2004, 2006, 2008; Nielsen *et al.*, 2009).

### Spinel group

Groundmass spinel (<100 µm) comprises Cr-rich varieties and almost pure magnetite end-member compositions, the latter of which are not further considered here, because they are most probably of late fluid-related, or secondary origin. The Cr-spinel grains are largely unzoned (Table 4) similar to those from the Benfontein calcite kimberlite sills in South Africa (Boctor & Boyd, 1981). This feature suggests slow crystallization and/or a long residence time at relatively high temperatures that facilitated compositional homogenization in a solid state (Roeder & Schulze, 2008), as is expected to occur in slowly cooling sills.

The Cr-spinel grains are MgO-rich (up to 15 wt %) and have elevated to high Cr/(Cr + Al) ratios predominantly between 0.72 and 0.86. These characteristics resemble spinel compositions from worldwide Group-I kimberlites and evolved calcite kimberlites (Mitchell, 1995; Nielsen & Sand, 2008; Roeder & Schulze, 2008). However, Amon kimberlite Cr-spinel compositions are at slightly lower Mg# compared with ‘typical’ kimberlite compositions (Fig. 9), but they are similar to those from flow differentiated kimberlite sills at Wemindji in Quebec (Zurevinski & Mitchell, 2011). The Amon kimberlite groundmass spinels display a rather restricted Ti/(Ti + Cr + Al) range within the evolutionary spectrum typically shown by kimberlitic spinels (Fig. 9). Most importantly, they fall between the ‘magnesian ulvöspinel’ (Kimberlite Trend 1) and ‘titanomagnetite’ (Kimberlite Trend 2) domains on the projected front face of the reduced spinel prism (Fig. 9). Although on a worldwide basis this feature is rather unusual for Group-I kimberlites, it has been described from numerous hypabyssal kimberlites of the Superior craton in eastern Canada (e.g. Renard kimberlites; Birkett *et al.*, 2004), as well as from carbonate-rich UML dykes (aillikites) of the Greenland–Labrador Diamond Province (Tappe *et al.*, 2006, 2009; Nielsen *et al.*, 2009) (Fig. 9).

### Ilmenite and rutile

Ilmenite macrocrysts (12.0–18.4 wt % MgO; 0.4–3.7 wt % Cr<sub>2</sub>O<sub>3</sub>) and groundmass laths (14–19 wt % MgO; 0.8–4.2 wt % Cr<sub>2</sub>O<sub>3</sub>) have overlapping major element compositions that are typical for kimberlitic ilmenites (Fig. 10) (Mitchell, 1995; Wyatt *et al.*, 2004). The groundmass ilmenite laths of the Amon sills contain elevated MnO concentration levels between 0.5 and 1.8 wt % (Table 5), which is typical of kimberlitic groundmass ilmenite (Mitchell, 1995) but much lower than the high MnO contents that are frequently reported for ilmenites from orangeites (formerly Group-II kimberlites), UMLs and associated

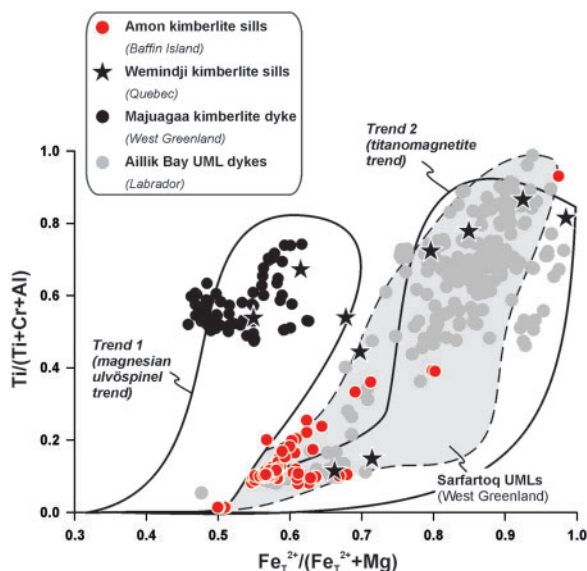


**Fig. 9.** Atomic Ti/(Ti + Cr + Al) vs  $\text{Fe}^{2+}/(\text{Fe}^{2+} + \text{Mg})$  of groundmass spinels from the Amon kimberlites in north-central Baffin Island. The primary spinel grains of the Amon kimberlites show an evolutionary trend that is between the ‘magnesian ulvöspinel’ (diagnostic for Group-I kimberlites; see Mitchell, 1986; Roeder & Schulze, 2008) and ‘titanomagnetite’ trends (diagnostic for Group-II kimberlites and UMLs, and observed rarely in some Group-I kimberlites; see Tappe *et al.*, 2005; Roeder & Schulze, 2008). Data from the Wemindji kimberlite sills (Zurevinski & Mitchell, 2011) and Majuagaa calcite kimberlite dyke (Nielsen & Sand, 2008) are shown for comparison. The groundmass spinel compositional range of Late Neoproterozoic Greenland–Labrador UML dykes (grey-shaded) is compiled from data given by Tappe *et al.* (2004, 2006) and Nielsen *et al.* (2009). (For location of the various Late Neoproterozoic kimberlites and related rocks from eastern Laurentia that are used for comparisons see the map in Fig. 2.)

carbonatites (up to 10 wt % MnO) (Gaspar & Wyllie, 1984; Mitchell, 1995; Tappe *et al.*, 2006).

The fairly abundant rutile grains in the groundmass of the Amon kimberlites have slightly elevated FeO and MnO contents (up to 3 and 2 wt %, respectively). The Cr<sub>2</sub>O<sub>3</sub> concentration levels are typically below 0.5 wt %, except for the rutile rims on ilmenite macrocrysts, where Cr<sub>2</sub>O<sub>3</sub> approaches 1.5 wt % (Table 5; Fig. 6d). The primary groundmass rutile described here is compositionally similar to rutile from the Benfontein calcite kimberlite sills in South Africa (Boctor & Boyd, 1981) and from the Wemindji kimberlite sills in Quebec (Zurevinski & Mitchell, 2011). It is important to note that groundmass rutile appears to be absent from orangeites (Mitchell, 1995), but has also been reported from carbonate-rich UML dykes of the 610–550 Ma Greenland–Labrador Diamond Province (Tappe *et al.*, 2004, 2006).

## Amon kimberlite bulk-rock geochemistry

### Major and trace element compositions

The Amon kimberlite sills display a wide range in major and trace element compositions (Table 6; Fig. 11), which is



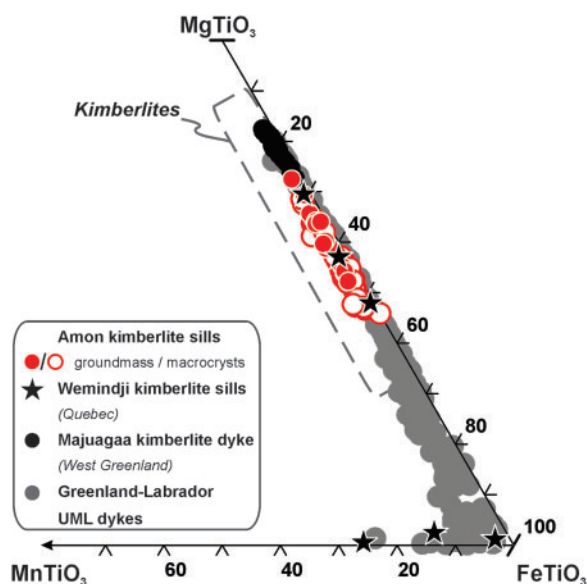


**Fig. 10.** Ilmenite compositions (mol %) from the Amon kimberlites of north-central Baffin Island plotted in the ternary system  $\text{FeTiO}_3$  (ilmenite)– $\text{MgTiO}_3$  (geikielite)– $\text{MnTiO}_3$  (pyrophanite). The overlap between groundmass and macrocryst compositions of the Amon kimberlite sills (Zurevinski & Mitchell, 2011) and Majuagaa calcite kimberlite dyke (Nielsen & Sand, 2008), as well as the 'kimberlite box' (Mitchell, 1995), are shown for comparison. The groundmass ilmenite compositional range of Late Neoproterozoic Greenland–Labrador UML dykes is compiled from data given by Tappe *et al.* (2004, 2006, 2008) and Nielsen *et al.* (2009). (For location of the various Late Neoproterozoic kimberlites and related rocks from eastern Laurentia that are used for comparisons see the map in Fig. 2.)

most probably a function of internal differentiation processes such as filter-pressing and flowage segregation that occurred at emplacement level (see Kjarsgaard, 2007; Zurevinski & Mitchell, 2011) (Fig. 6a–c). In general, the sills have high  $\text{MgO}$  (15–33 wt %),  $\text{TiO}_2$  (1.9–3.5 wt %),  $\text{Ni}$  (294–1230 ppm), and  $\text{Cr}$  (710–1610 ppm) contents, and they are relatively poor in  $\text{SiO}_2$  (13–39 wt %),  $\text{Al}_2\text{O}_3$  (1.7–4.0 wt %),  $\text{K}_2\text{O}$  (0.1–1.4 wt %), and  $\text{Na}_2\text{O}$  (0.02–0.2 wt %), resembling the range of values for archetypal Group-I kimberlites from southern Africa (Smith *et al.*, 1985; Le Roex *et al.*, 2003; Becker & Le Roex, 2006).

Relative to the compositional spectrum of worldwide hypabyssal Group-I kimberlites [see compilation by Kjarsgaard *et al.* (2009)], the Amon kimberlite sills tend to fall at the lower end in terms of  $\text{MgO}$ ,  $\text{K}_2\text{O}$ , and  $\text{Na}_2\text{O}$  contents, whereas their  $\text{TiO}_2$  content falls at the upper end (Fig. 11). The  $\text{SiO}_2$ ,  $\text{Al}_2\text{O}_3$ ,  $\text{CaO}$ , and  $\text{CO}_2$  contents of the Amon kimberlites span the entire compositional range of worldwide hypabyssal Group-I kimberlites. Samples A7 and A11 have exceptionally low  $\text{SiO}_2$  but high  $\text{CaO}$  and  $\text{CO}_2$  contents compared with worldwide hypabyssal Group-I kimberlites (Table 6). These samples are characterized by abundant modal carbonate and resemble evolved calcite kimberlites and carbonate-rich UMLs

from regional Late Neoproterozoic dyke swarms that cut across West Greenland and northern Labrador (Fig. 11). The Amon kimberlite sills appear generally more evolved (e.g. lower  $\text{MgO}$ , higher  $\text{Al}_2\text{O}_3$  and  $\text{CO}_2$ ) compared with other Late Neoproterozoic hypabyssal kimberlites from eastern Laurentia such as the Renard intrusive bodies in Quebec (Birkett *et al.*, 2004) and the Majuagaa dyke in West Greenland (Nielsen *et al.*, 2009; Tappe *et al.*, 2011) (Fig. 2). However, their generally lower  $\text{TiO}_2$  (<3.5 vs up to 10 wt %) and alkali contents (<1.4 vs up to 4 wt %  $\text{K}_2\text{O}$ ) distinguish the Amon sills from regional Greenland–Labrador UML dyke swarms (Fig. 12) (Nielsen *et al.*, 2009; Tappe *et al.*, 2006, 2008, 2011), and the Amon occurrence is best described as an evolved kimberlite sill complex. Despite the lack of published bulk-rock compositions for the 629 Ma Wemindji kimberlite sills in Quebec (Fig. 2), the petrographic descriptions and mineralogical data provided by Zurevinski & Mitchell (2011), as summarized here in Figs 8–10, indicate a strong compositional resemblance between the Wemindji and Amon kimberlite sill complexes of eastern Laurentia.

The primitive mantle normalized incompatible element abundance patterns in Fig. 13 demonstrate the strong trace element enrichment of the Amon kimberlites. Barium, Th, U, Nb, Ta, and light rare earth element (LREE) concentrations typically exceed 100 times primitive mantle. Pronounced relative depletions are apparent for Cs–Rb, K, Pb, Sr, Zr–Hf, and the heavy rare earth elements (HREE), for which concentrations drop to below 50 times primitive mantle. Although the Amon kimberlite incompatible element distribution patterns resemble those for South African Group-I kimberlites (Fig. 13), the Amon sills have much higher Th–U and much lower Sr–P concentration levels, which point to residual apatite in their mantle source region. Furthermore, it appears that the concentrations of moderately incompatible elements (La to Lu in Fig. 13; except for Sr) in the Amon sills are higher than in the Renard and Majuagaa hypabyssal kimberlites. The Amon kimberlite sills approach the elevated trace element concentration levels that are typical for the Late Neoproterozoic Greenland–Labrador UML dykes (Fig. 13a). This mainly reflects their generally lower content of olivine macrocrysts (i.e. less dilution by refractory cratonic mantle material; Figs 5a–c and 6a, b) and, thus, points to the flow differentiated nature of the kimberlite magma that formed the sill complex.

Although much more enriched in highly incompatible elements than ocean island basalt (OIB), the Amon kimberlites have Nb/U ( $25 \pm 9$ ) ratios that are more similar to plume-related intraplate oceanic magmas (Nb/U =  $47 \pm 10$ ; Hofmann *et al.*, 1986) than to subduction-influenced mafic alkaline magmas such as orogenic lamproites (Nb/U <10; Prelevic *et al.*, 2008). Other ratios of relatively

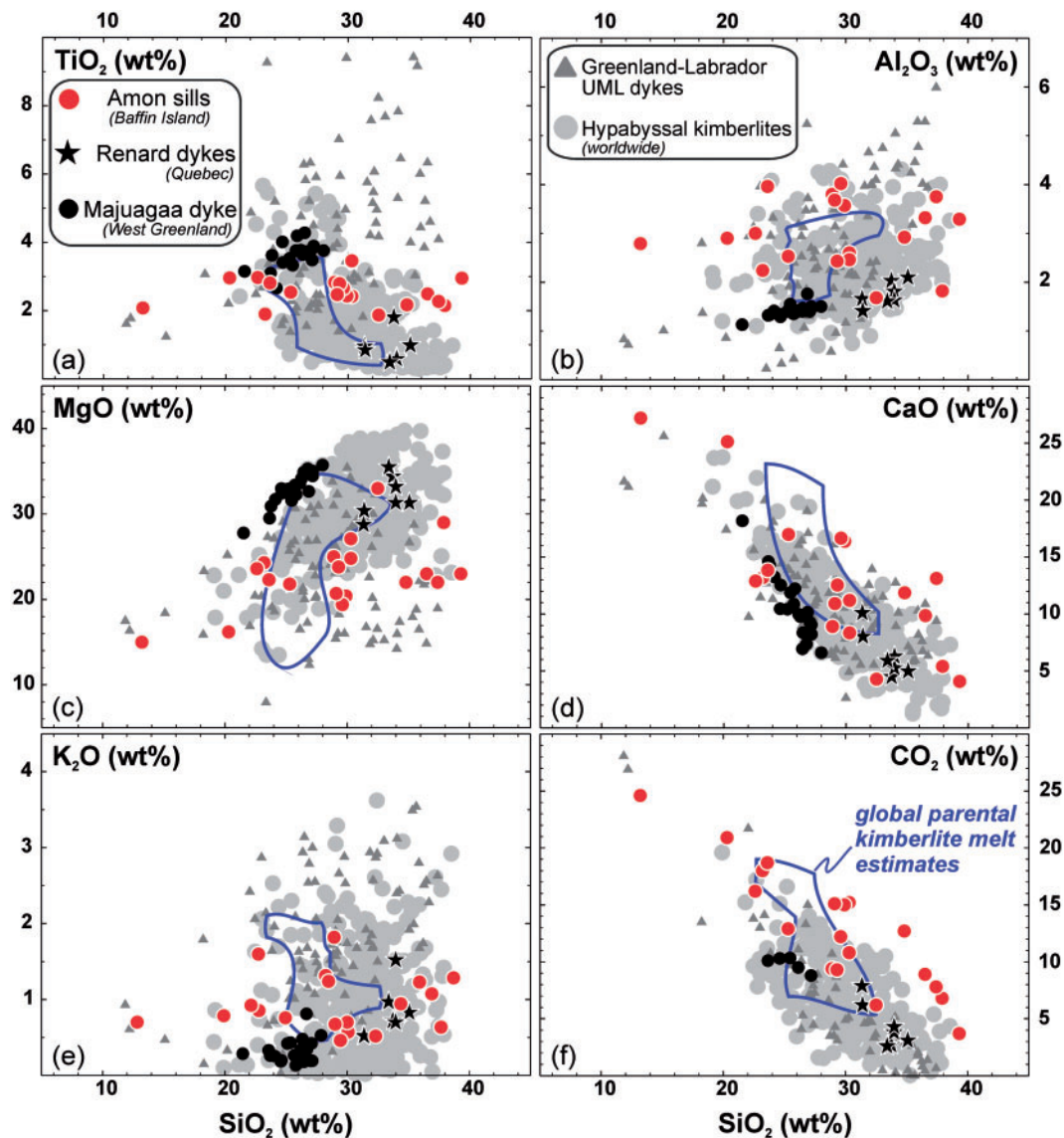


**Fig. 11.** Variations of major element oxides vs  $\text{SiO}_2$  (wt %) for the Amon kimberlite sills, north-central Baffin Island. The wide range in major element compositions of the Amon kimberlites, which partially overlaps the compositional field for estimates of global parental kimberlite melts, should be noted. The major element compositional diversity of the Amon sills is most probably a direct function of the presence of crystal-rich, cumulitic parts and residual carbonate melt-rich parts in the sill complex; that is, owing to flow differentiation and/or filter-pressing. Data for other Late Neoproterozoic kimberlites and UMLs from eastern Laurentia are shown for comparison: Renard hypabyssal kimberlites (Birkett *et al.*, 2004); Majuagaa kimberlite dyke (Nielsen *et al.*, 2009; Tappe *et al.*, 2011); Greenland-Labrador UML dykes (Tappe *et al.*, 2006, 2008, 2011; Nielsen *et al.*, 2009). The compilation of high-quality data for hypabyssal kimberlites from worldwide occurrences is taken from Kjarsgaard *et al.* (2009). The blue outlines mark the compositional space occupied by reconstructed parental kimberlite melts from various cratons worldwide (data sources: Le Roex *et al.*, 2003; Harris *et al.*, 2004; Becker & Le Roex, 2006; Kamenetsky *et al.*, 2007; Kopylova *et al.*, 2007; Kjarsgaard *et al.*, 2009; Patterson *et al.*, 2009, except for  $\text{Al}_2\text{O}_3$ ).

immobile trace elements such as Ba/Nb and La/Nb demonstrate the Group-I kimberlite affinity of the Amon sills; that is, they overlap with archetypal South African kimberlites (Fig. 14). The Ba/Nb vs La/Nb systematics of the Amon sills (Fig. 14) also overlap with the Renard and Majuagaa hypabyssal kimberlites of eastern Laurentia. However, the trace element systematics suggest that the more evolved nature of the Amon sills, as apparent

from their major element compositions (Figs 11 and 12), is of a different origin (e.g. flow differentiation) compared with the apparently evolved nature of the Greenland-Labrador UML magmas (Fig. 13a). The latter evolved toward elevated La/Nb at constant and low Ba/Nb, which is in contrast to the high Ba/Nb evolution that is characteristic for the mineralogically similar South African orangeites (Fig. 14). This suggests magma

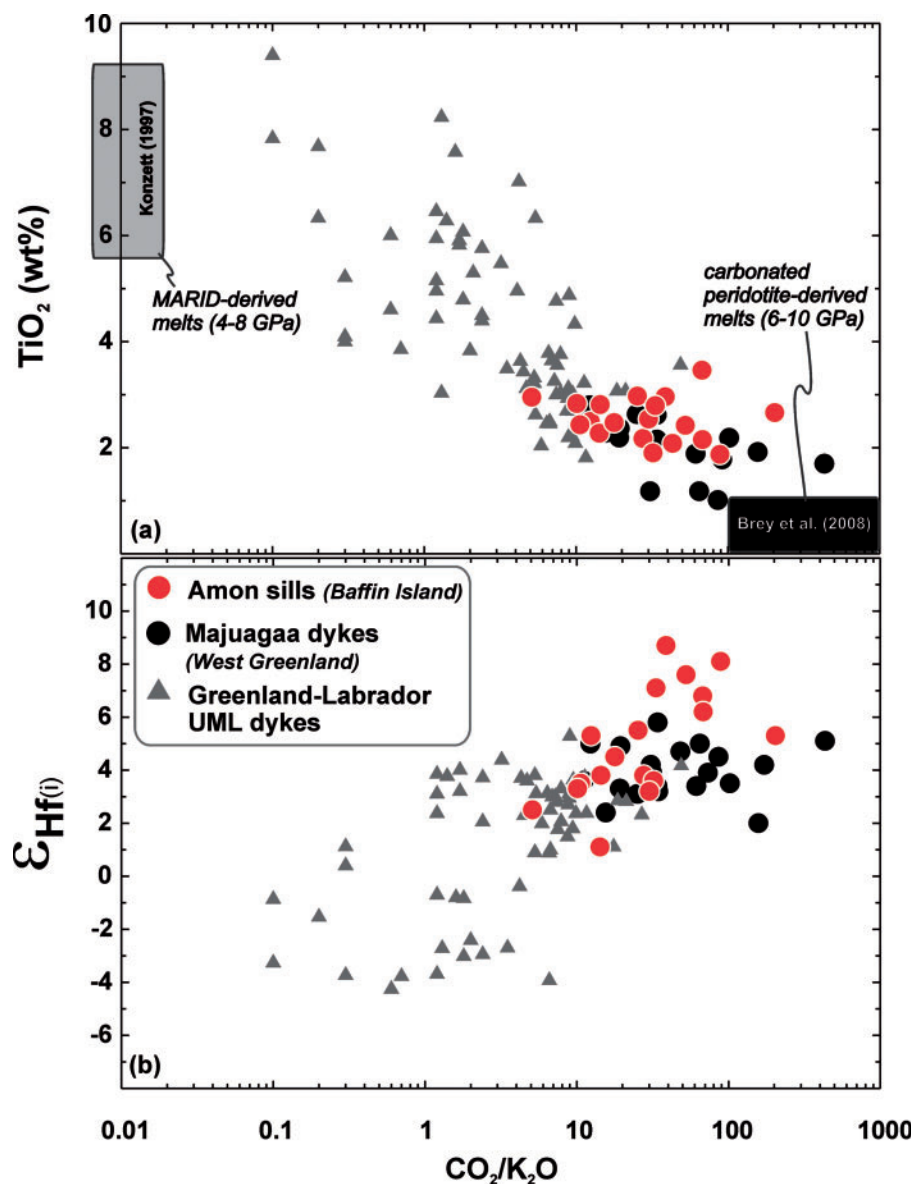


**Fig. 12.** Variation of bulk-rock  $\text{TiO}_2$  (a) and  $\epsilon_{\text{Hf}(i)}$  (b) vs  $\text{CO}_2/\text{K}_2\text{O}$  for the Amon kimberlites, north-central Baffin Island. The grey and black fields for experimentally derived melt compositions in (a) are from Konzett (1997) and Brey *et al.* (2008), respectively. It should be noted that ilmenite macrocryst-rich samples (i.e. elevated  $\text{TiO}_2$  contents) from the Majuagaa kimberlite dyke are not plotted because they do not represent melt compositions. Data for the Majuagaa–Maniitsoq kimberlite dykes (Tappe *et al.*, 2011) and Greenland–Labrador UML dykes (Tappe *et al.*, 2007, 2008, 2011) are shown for comparison.

derivation from distinctly different metasomatic assemblages in the upper mantle source regions for the UMLs and orangeites (see Tappe *et al.*, 2008), whereas we argue that the Amon magma evolved from typical Group-I kimberlite melt by a shallow-level flow differentiation process (see Figs 5 and 6; Supplementary Data Appendix D). Flow differentiation including filter-pressing has also been proposed to be the main mechanism by which the Late Neoproterozoic Wemindji kimberlite sills of Quebec evolved (Zurevinski & Mitchell, 2011).

#### *Sr–Nd–Hf isotope compositions*

The initial Sr, Nd, and Hf isotope compositions of the Amon kimberlites were calculated for an emplacement age of 673 Ma as determined in this study (see footnote to Table 7 for relevant parameters). We also determined initial  $\Delta\epsilon_{\text{Hf}}$  values according to Johnson & Beard (1993), and these values are reported relative to the Nd–Hf isotope mantle array of Chauvel *et al.* (2008).

The initial Sr isotope compositions of the Amon kimberlites range between  $^{87}\text{Sr}/^{86}\text{Sr}_{(i)}$  of 0.70358 and 0.70775.

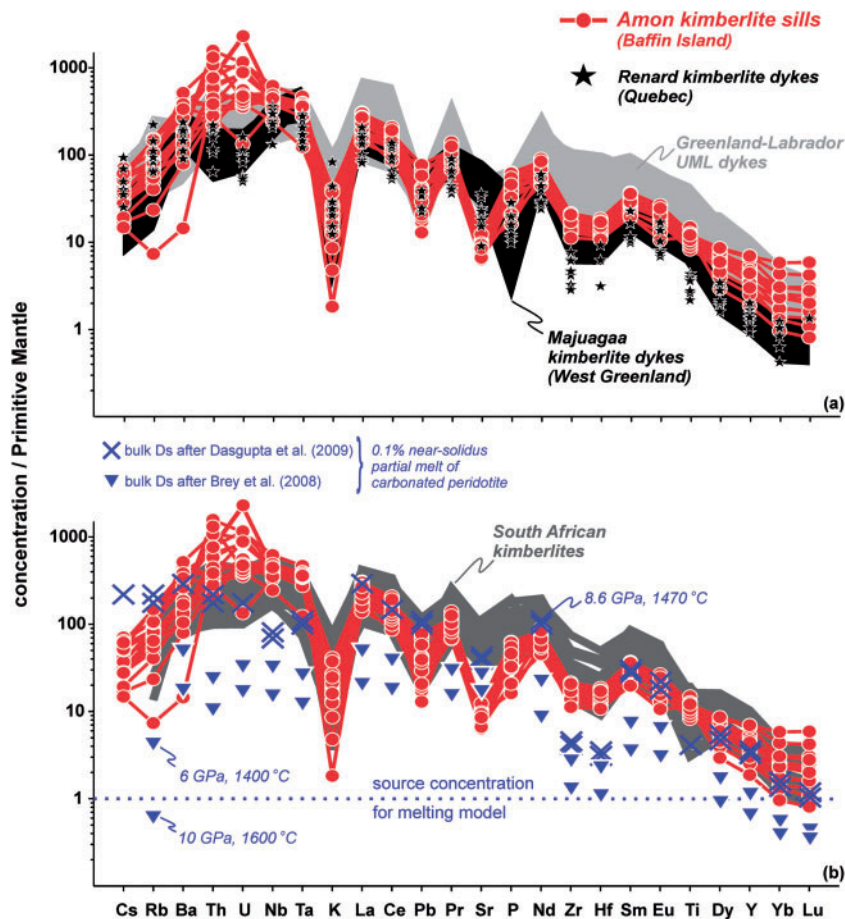


**Fig. 13.** Primitive mantle normalized incompatible element patterns for Amon kimberlite sill samples. (a) Comparison with incompatible element patterns of other Late Neoproterozoic kimberlite and UML dyke occurrences across eastern Laurentia (Renard kimberlites, Birkett *et al.*, 2004; Majuagaa kimberlites, Nielsen *et al.*, 2009; Tappe *et al.*, 2011; Greenland-Labrador UMLs, Tappe *et al.*, 2006, 2008, 2011; Nielsen *et al.*, 2009). (b) Comparison of the incompatible element patterns of the Amon kimberlites with various carbonate-rich ultramafic melts that serve as experimentally derived analogs for high-pressure, mantle-derived, low-volume melts. The calculated trace element patterns for near-solidus partial melts of carbonated peridotite at 6 and 10 GPa (Brey *et al.*, 2008), as well as at 8.6 GPa (Dasgupta *et al.*, 2009) utilize experimentally determined bulk peridotite/melt partition coefficients and a 0.1% batch partial melting model with primitive mantle trace element starting concentrations (i.e. a relatively fertile mantle source). Patterns for South African kimberlites are from Le Roex *et al.* (2003) and Becker & Le Roex (2006). Primitive mantle values are from Palme & O'Neill (2003).

This relatively wide range is in contrast to the narrow range of moderately depleted initial Nd isotope compositions between  $\epsilon_{\text{Nd}(i)}$  of +1.5 and +3.5. Although some workers have interpreted such near-horizontal arrays defined by volatile-rich ultramafic magmas in Sr–Nd isotope space (Fig. 15a) to be produced by enhanced radiogenic Sr in-growth owing to locally enriched abundances of phlogopite (i.e. a high Rb/Sr phase) within a cratonic mantle source region (e.g. Andronikov & Foley, 2001), these trends are readily explained by low-*T* alteration of a slowly cooling volatile-rich magmatic system (e.g. Becker & Le Roex, 2006). The latter interpretation is in good agreement with findings from a groundmass perovskite study on Greenland kimberlites and related rocks, where it was demonstrated that hydrothermal overprinting does not affect bulk kimberlite Nd isotope compositions (Tappe

*et al.*, 2012b), whereas it significantly elevates  $^{87}\text{Sr}/^{86}\text{Sr}$ , even in fresh kimberlite material (Woodhead *et al.*, 2009; Malarkey *et al.*, 2010; Tappe *et al.*, 2011).

Although the initial Hf isotope compositions of the Amon kimberlites are also moderately depleted, they show a much wider range ( $\epsilon_{\text{Hf}(i)} = +1.1$  to +8.7) than the corresponding Nd isotope compositions (Fig. 15b). In Sr–Nd–Hf isotope space, the most pristine Amon kimberlite samples fall within the mildly depleted sector of the mantle array defined by oceanic basalts (Fig. 15). They partly overlap the fields for South African kimberlites and have initial  $\Delta\epsilon_{\text{Hf}}$  values between –4.2 and +2.7, with ‘negative’ samples falling by definition below the mantle Nd–Hf isotope regression line of Chauvel *et al.* (2008). Samples that depart by more than five epsilon Hf units from this regression line are identified as lying outside the



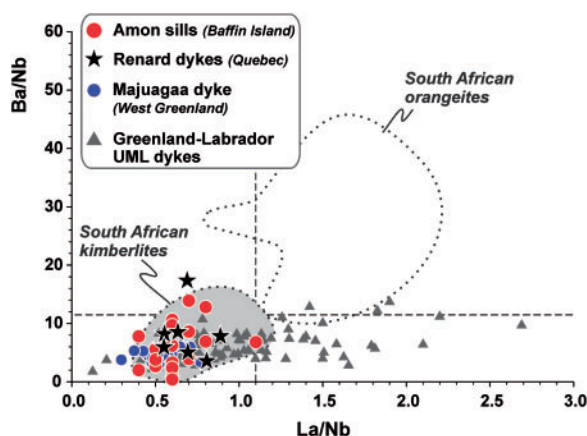


**Fig. 14.** Variation of bulk-rock Ba/Nb vs La/Nb for the Amon Kimberlite Sill Complex, north-central Baffin Island. Fields for South African kimberlites (i.e. Group-I) and orangeites (formerly Group-II kimberlites), as well as the dashed dividing lines that broadly separate the two kimberlite groups, are adopted from Becker & Le Roex (2006). Data for other Late Neoproterozoic kimberlites and UMLs from eastern Laurentia are shown for comparison: Renard hypabyssal kimberlites (Birkett *et al.*, 2004); Majuagaa kimberlite dyke (Nielsen *et al.*, 2009; Tappe *et al.*, 2011); Greenland-Labrador UML dykes (Tappe *et al.*, 2006, 2008, 2011; Nielsen *et al.*, 2009). The evolution of the eastern Laurentian volatile-rich ultramafic magmas toward elevated La/Nb at constant, low Ba/Nb, which is in contrast to the high Ba/Nb evolution that is characteristic for the mineralogically similar South African orangeites, should be noted.

mantle array; that is, they are isotopically ‘anomalous’ (e.g. Johnson & Beard, 1993). However, all of the studied Amon kimberlite samples fall within the Nd–Hf isotope mantle array ( $\Delta\epsilon_{\text{Hf}} = +5$  to  $-5$ ; Fig. 15b), which is in contrast to a large number of kimberlite samples from southern Africa (initial  $\Delta\epsilon_{\text{Hf}}$  down to  $-10$ ; Nowell *et al.*, 2004) and the central Slave province in Canada (initial  $\Delta\epsilon_{\text{Hf}}$  down to  $-6.6$ ; Tappe *et al.*, 2013a). These kimberlites show pronounced Nd–Hf isotope decoupling for which various petrogenetic explanations have been proposed, and will be discussed in further detail below.

Considering the Amon kimberlite Nd–Hf isotope systematics within the framework of the Late Neoproterozoic Greenland–Labrador Diamond Province (Tappe *et al.*, 2011), it becomes clear that there is significant compositional overlap with the Majuagaa–Maniitsoq kimberlite dykes of West Greenland ( $\epsilon_{\text{Nd}(i)} = +1.9$  to  $+3.6$ ;  $\epsilon_{\text{Hf}(i)} = +2.0$  to  $+5.8$ ; Fig. 15b). The calcite kimberlite dykes of the Maniitsoq region, together with the most carbonate-rich UML dykes of northern Labrador, are suggested to represent a common carbonate-rich convecting upper mantle-derived component that was widespread beneath eastern Laurentia (Tappe *et al.*, 2011, 2012b). This carbonate-rich component is also suggested to have significantly contributed to the 673 Ma Amon kimberlite magmatism beneath north-central Baffin Island, and it variably interacted with cratonic metasomes across eastern

Laurentia to produce trace element and isotopically enriched UML magmas (Tappe *et al.*, 2008, 2011; Nielsen *et al.*, 2009; Figs 13 and 15).

## PETROGENESIS OF THE AMON KIMBERLITES

### Crustal contamination and flow differentiation

To assess the potential effects of crustal contamination and alteration we apply the criteria established by Clement (1982) and further developed by Le Roex *et al.* (2003). The Amon kimberlite samples have Contamination Index values ( $\text{C.I.} = (\text{SiO}_2 + \text{Al}_2\text{O}_3 + \text{Na}_2\text{O}/\text{MgO} + 2\text{K}_2\text{O}) / (\text{Clement, 1982; see also Mitchell, 1986})$  between 1.0 and 1.8, which indicates that assimilation of continental crustal material is absent to insignificant. For example, Taylor *et al.* (1994) worked with kimberlite major element analyses from West African localities that have C.I. values of up to 2.2. Paton *et al.* (2009) rejected isotope analyses of Indian kimberlite samples with C.I. values  $>1.5$  following recommendations by Mitchell (1986). However, Kjarsgaard *et al.* (2009) demonstrated for a hypabyssal kimberlite dataset from the central Slave craton of Canada that the combined effects of crustal contamination and entrainment of mantle-derived material cancel each other out in terms of C.I. values, which highlights a potential risk concerning the reliability of C.I. values. Provided that the majority of Amon kimberlite samples contain only small amounts of olivine macrocrysts and hardly any mantle fragments (Figs 5 and 6), we conclude that their C.I. values may be a realistic indication that little to no crustal contamination has occurred (although the effects of kimberlite magma differentiation on C.I. are still relatively unexplored). This observation is further augmented by the negative Pb anomalies relative to neighbouring LREE in primitive mantle normalized multi-element patterns (Fig. 13). In contrast, the shallowing of the HREE slopes in Fig. 13 may be caused by minor crustal contamination (see Le Roex *et al.*, 2003), but in the absence of additional evidence, the cause of this signature remains ambiguous. The Amon kimberlite data do not show any correlation between radiogenic isotope ratios and C.I. values, Pb and HREE contents (not shown), which indicates that the incompatible element based isotope systems (i.e. Sm–Nd and Lu–Hf) were buffered against possible minor additions of these elements from crustal material. It should be noted, however, that the elevated Sr isotope ratios of the Amon kimberlites were largely caused by hydrothermal overprinting (not crustal contamination; see Malarkey *et al.*, 2010), a process that does not appear to affect the Nd and Hf isotope systematics.

Despite the absence of significant assimilation of crustal material, the major element compositions of the Amon



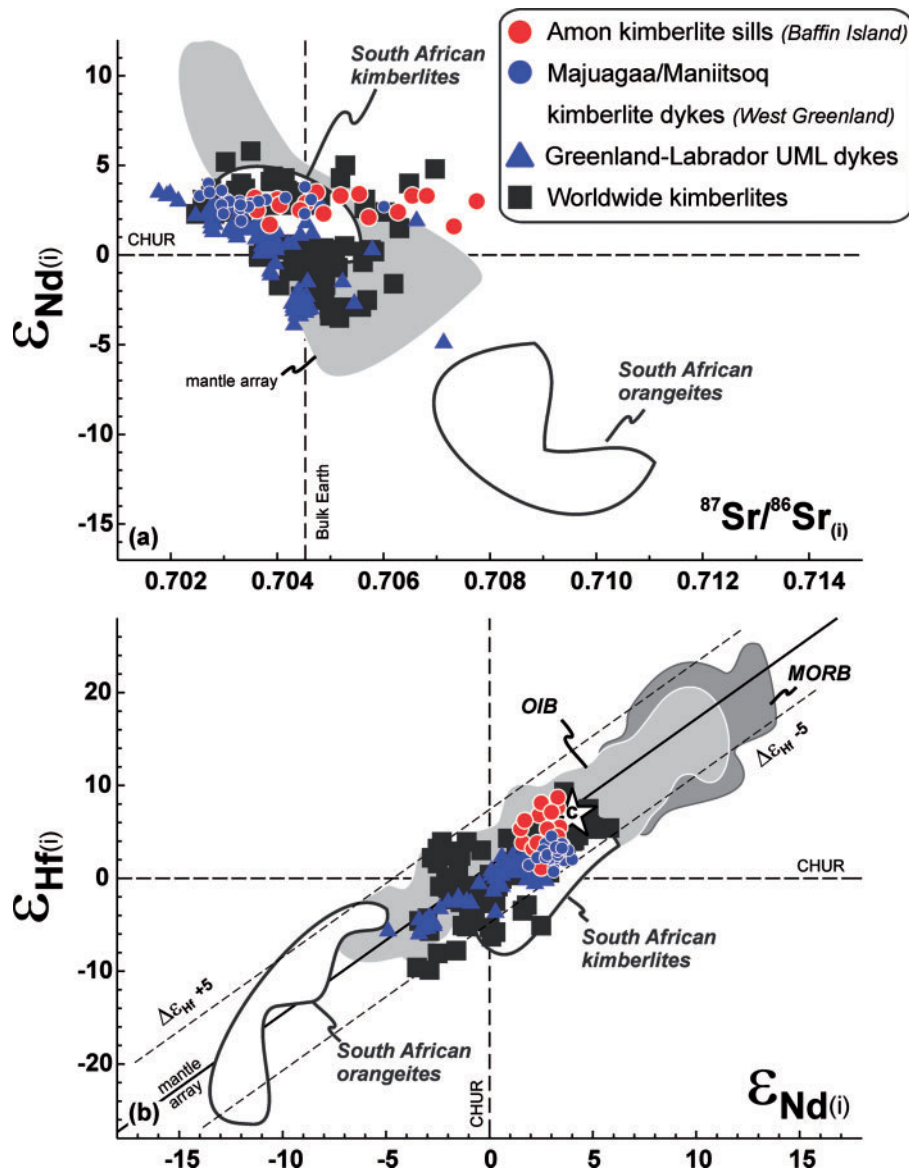


**Fig. 15.**  $\epsilon_{\text{Nd}(i)}$  vs  $^{87}\text{Sr}/^{86}\text{Sr}(i)$  (a) and  $\epsilon_{\text{Hf}(i)}$  vs  $\epsilon_{\text{Nd}(i)}$  (b) of the Amon kimberlite sills from north-central Baffin Island. Data for other Late Neoproterozoic kimberlites and UMLs from eastern Laurentia are shown in blue symbols (Majuagaa-Maniitsoq kimberlite dykes, Tappe *et al.*, 2011; Greenland-Labrador UML dykes, Tappe *et al.*, 2007, 2008, 2011). The worldwide compilation of Group-I kimberlites and their megacrysts encompasses data from Siberia (Carlson *et al.*, 2006), Greenland (Gaffney *et al.*, 2007; Tappe *et al.*, 2011), India (Paton *et al.*, 2009), China (Yang *et al.*, 2009), Antarctica (Yaxley *et al.*, 2013), and the Slave craton of northwestern Canada (Kopylova *et al.*, 2009; Tappe *et al.*, 2013a). The open star symbol with 'c' represents the carbonate-rich depleted component of the Greenland-Labrador Diamond Province (Tappe *et al.*, 2011); this convecting upper mantle-derived component contributed significantly to the Amon kimberlite magmas. Fields for Mesozoic South African kimberlites and orangeites (Nowell *et al.*, 2004), as well as modern oceanic basalts (OIB and MORB) (compilation retrieved in January 2014 from <http://georoc.mpch-mainz.gwdg.de/georoc/>) are shown for comparison. Mantle array after Chauvel *et al.* (2008).

sills are widely scattered (Figs 11 and 16). The variation diagrams displayed in Fig. 11 show that the Amon kimberlites extend to the lower and upper ends of the compositional fields that are established estimates for parental kimberlite melts from worldwide localities (Le Roex *et al.*, 2003; Harris *et al.*, 2004; Becker & Le Roex, 2006; Kamenetsky *et al.*, 2007; Kopylova *et al.*, 2007; Kjarsgaard *et al.*, 2009;

Patterson *et al.*, 2009). The simplest explanation for this compositional spread across primitive kimberlite compositions is that a differentiation process or processes operated during sill emplacement. Bulk-rock major element mass-balance considerations indicate that this process efficiently fractionated 15–30 wt % olivine macrocrysts and, or, phenocrysts and other, minor early stage phases from a

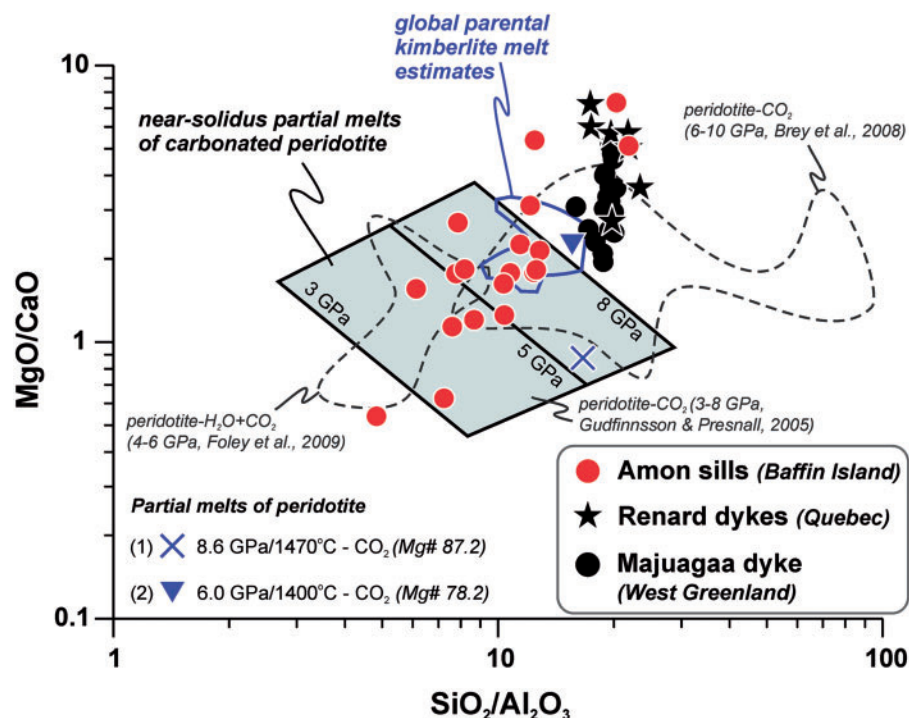


**Fig. 16.** MgO/CaO vs  $\text{SiO}_2/\text{Al}_2\text{O}_3$  for measured Amon kimberlite sill samples. The blue outline marks the compositional space occupied by reconstructed parental kimberlite melts from various cratons worldwide (data sources: Le Roex *et al.*, 2003; Harris *et al.*, 2004; Becker & Le Roex, 2006; Kamenetsky *et al.*, 2007; Kopylova *et al.*, 2007; Kjarsgaard *et al.*, 2009). The gray field represents experimentally produced melt compositions from synthetic carbonated peridotite between 3 and 8 GPa (Gudfinnsson & Presnall, 2005). The dashed gray outlines represent experimentally produced melt compositions from synthetic carbonated peridotite between 4 and 6 GPa (phlogopite present) (Foley *et al.*, 2009) and 6 and 10 GPa (phlogopite absent) (Brey *et al.*, 2008). Additional experimentally produced partial melt compositions of volatile-saturated peridotites are shown for reference and discussed in the main text: (1) Dasgupta *et al.* (2009); (2) Brey *et al.* (2008). Representative hypabyssal kimberlite compositions from the Renard (Birkett *et al.*, 2004) and Majuagaa (Nielsen *et al.*, 2009; Tappe *et al.*, 2011) occurrences are shown for comparison.

residual carbonate-rich melt; the latter locally pooled in segregations (Fig. 5b; Supplementary Data Appendix D). One such process may have been filter-pressing (Kjarsgaard, 2007), which is known to operate in kimberlitic dykes and sills (compare the variable groundmass proportions between Fig. 6b and 6c), as for example in the Wemindji sills of Quebec (Zurevinski & Mitchell, 2011) and in the inclined Snap Lake sheet of the Slave province (Gernon *et al.*, 2012). Although the relatively poor preservation of the Amon kimberlite sills does not allow for reliable reconstruction of the near-primary melt composition, we contend that the parental magma that fed the sill complex was compositionally akin to other worldwide Group-I kimberlites. This notion is supported by groundmass phlogopite and ilmenite compositions, which record typical kimberlite magma evolutionary trends (Figs 8 and 10).

### Magma formation

In an attempt to minimize the effects of magma differentiation at Amon, primarily olivine fractionation or accumulation, we use the bulk-rock  $\text{CO}_2/\text{K}_2\text{O}$  ratio as an approximation of the 'true' melt compositions of the sill samples (olivine is an effectively C-, K-, and Ti-free

phase). Figure 12a shows that the Amon kimberlites have high  $\text{CO}_2/\text{K}_2\text{O}$  ratios that approach experimentally produced near-solidus partial melts of carbonated peridotite at 6–10 GPa (Brey *et al.*, 2008). The residual 'melt' fraction of the Amon sills overlaps with the compositions of the Late Neoproterozoic Majuagaa–Maniitsoq calcite kimberlite dykes of West Greenland. Greenland–Labrador UML compositions have much lower  $\text{CO}_2/\text{K}_2\text{O}$  ratios and higher  $\text{TiO}_2$  than the experimentally produced kimberlitic melts of Brey *et al.* (2008), and they overlap only with the most evolved Amon kimberlite samples (Fig. 12a). This apparent gradation is inconsistent with either a primary kimberlite–UML or UML–kimberlite melting relationship of a common carbonated peridotite source, because the most  $\text{CO}_2$ -rich melts nearest the solidus should have the lowest MgO but highest  $\text{K}_2\text{O}$  and  $\text{TiO}_2$  contents (Foley *et al.*, 2009). On the contrary, we observe a pronounced increase in  $\text{TiO}_2$  (and  $\text{Al}_2\text{O}_3$ , not shown) with decreasing  $\text{CO}_2/\text{K}_2\text{O}$  from Majuagaa–Maniitsoq kimberlites through Amon kimberlites to the UMLs of the Greenland–Labrador Diamond Province (Fig. 12). This trend is unlikely to be a result of contamination with continental crustal material close to the Earth's surface, or

within the mantle source (Prelevic *et al.*, 2010), because the generally increasing K contents are accompanied by increasing La/Nb ratios (Fig. 14). Instead, this compositional trend approaches melt compositions that have been experimentally produced under diamond-stability field conditions from synthetic ultramafic MARID-type starting material (Konzett, 1997). Such K-rich metasomatic lithologies are inferred to be present in the form of veins within peridotite, in particular beneath the Paleoproterozoic mobile belts of cratonic eastern Laurentia (Peterson & LeCheminant, 1993; Cousens *et al.*, 2001; Larsen *et al.*, 2003; Larsen & Garrit, 2005; Tappe *et al.*, 2006, 2008, 2011).

In terms of MgO/CaO vs SiO<sub>2</sub>/Al<sub>2</sub>O<sub>3</sub> systematics, the Amon kimberlites also show wide scatter, with highly magnesian samples overlapping the compositions of olivine macrocrystic kimberlites from the Late Neoproterozoic Renard and Majuagaa occurrences (Fig. 16). In contrast, the more carbonate-rich kimberlite samples have MgO/CaO ratios below unity, approaching the compositions of carbonate-rich UMLs and their associated carbonatites (see Tappe *et al.*, 2012b, their fig. 6). It is apparent from Fig. 16 that neither the olivine-rich nor the carbonate-rich Amon kimberlite samples represent primary liquid compositions because they fall outside the compositional fields for experimentally derived near-solidus partial melts of carbonated peridotite between 5 and 10 GPa. However, a significant portion of the sample population overlaps the field for global parental kimberlite melt estimates, and these compositions resemble experimentally derived near-solidus partial melts of carbonated peridotite above 5 GPa (Gudfinnsson & Presnall, 2005; Brey *et al.*, 2008). Importantly, only a few Amon kimberlite samples straddle the compositional field for experimentally produced near-solidus partial melts of phlogopite-rich carbonated peridotite under diamond-stability field conditions (Foley *et al.*, 2009). This observation supports the widely held view that Group-I kimberlites, such as the Amon sills, are derived from the convecting upper mantle—outside the thermal stability field of phlogopite (Frost, 2006)—during volatile-fluxed melting of fertile peridotite beneath a thick cratonic lid (Smith, 1983; Le Roex *et al.*, 2003; Carlson *et al.*, 2006; Paton *et al.*, 2009; Tappe *et al.*, 2012b, 2013a; Yaxley *et al.*, 2013).

Incompatible trace element geochemistry, in particular that of the fluid-immobile elements, provides further constraints on magma formation in addition to the information obtained from phase equilibria studies. In contrast to the trace element inversion modelling that was performed by Le Roex and co-workers (Le Roex *et al.*, 2003; Becker & Le Roex, 2006) in an attempt to reconstruct the magma source for southern African kimberlites, we use experimentally determined ‘bulk’ peridotite/melt partition coefficients for forward modelling (Brey *et al.*, 2008;

Dasgupta *et al.*, 2009). This approach allows us to calculate trace element patterns for partial melts of carbonated peridotite between 6 and 10 GPa utilizing a batch partial melting model (Fig. 13b). For the sake of simplicity, the trace element concentrations of the source were set at primitive mantle values (Palme & O'Neill, 2003) and the degree of partial melting was held constant at 0.1% (McKenzie, 1985; Gudfinnsson & Presnall, 2005; Khazan & Fialko, 2005). To a first approximation, the obtained inter-element fractionations match remarkably well the trace element distribution patterns of the Amon kimberlites (Fig. 13b), especially for the REE and Zr–Hf. We note, however, that the incompatible trace element concentration levels of the calculated melts are mostly lower than in the Amon kimberlites. The difference is typically much less than an order of magnitude, and the choice of a more fertile starting composition and/or lowering of the degree of partial melting would further improve the match between model and nature.

The observations from our trace element forward modelling, together with the major element inferences discussed above, suggest that a significant component of the Amon kimberlites could have formed by low-degree partial melting of carbonated peridotite at convecting upper mantle conditions. Furthermore, the trace element modelling shows that some of the hallmark geochemical features of kimberlites, such as pronounced Zr–Hf depletions and extremely high LREE/HREE ratios, can be generated by low-degree partial melting of fertile peridotite in the presence of CO<sub>2</sub> within the convecting upper mantle beneath thick cratonic lithosphere. In other words, the creation of these trace element features neither requires involvement of metasomatic source components (e.g. Le Roex *et al.*, 2003) nor chromatographic enrichment during porous flow upon magma ascent (Khazan & Fialko, 2005). An exception may be the presence of residual apatite and/or its high-pressure phosphate breakdown product in the wider peridotite melt source region, because the Amon kimberlites have significantly elevated Th–U and much lower P concentrations compared with other worldwide Group-I kimberlites (Fig. 13). The thermal stability of apatite and its high-pressure phosphate breakdown product has recently been shown to correspond to the ambient mantle temperatures at the cratonic lithosphere–asthenosphere boundary (*c.* 1300°C, Konzett *et al.*, 2012), where this peculiar trace element signature may have been imprinted on ascending kimberlite magma during reactive melt transport (see Russell *et al.*, 2012).

### Constraints on the ultimate magma origin

The congruence of major and trace element data for the Amon kimberlites with experimental constraints and modelling results suggests that the ultimate kimberlite magma source is carbonated peridotite located beneath the cratonic lithosphere, in the convecting upper mantle. Tappe

*et al.* (2011) proposed that a common carbonate-rich end-member component contributed variably to each of the kimberlite and UML dyke swarms of the Late Neoproterozoic Greenland–Labrador Diamond Province. This suggestion was primarily based on the fact that Nd–Hf–(Sr) isotope data converge toward a focal area of moderately depleted isotope compositions (e.g.  $+4 \epsilon_{\text{Nd}}$  and  $+7 \epsilon_{\text{Hf}}$ ; Fig. 15b). This focal area falls within the field covered by the majority of worldwide carbonatites (Bizimis *et al.*, 2003, and references therein). Among the isotopically investigated Late Neoproterozoic kimberlites and UMLs of eastern Laurentia, the Amon kimberlites fall closest to this previously hypothesized depleted end-member, which is in good agreement with their generally carbonate-rich nature (Fig. 11). For example, in Fig. 12b it is clear that Amon kimberlite samples with high  $\text{CO}_2/\text{K}_2\text{O}$  have the most radiogenic Hf isotope compositions. Moreover, there exists a subtle positive correlation, which suggests that minute amounts of a more enriched component mixed with the more voluminous carbonate-rich proto-kimberlite melt. Provided that the isotopically enriched component has elevated  $\text{K}_2\text{O}$  (Fig. 12b), and partially overlaps the compositions of primitive Greenland–Labrador UMLs, it seems likely that it represents a K-rich cratonic mantle metasome of MARID affinity (Choukroun *et al.*, 2005; Larsen & Garrit, 2005; Tappe *et al.*, 2008, 2011). This interpretation is supported by the fact that Amon kimberlites with slightly elevated  $\text{K}_2\text{O}$  (and lower  $\text{CO}_2$ ) have elevated  $\text{TiO}_2$  concentrations approaching an experimental MARID-derived melt end-member composition (Fig. 12a).

In terms of Nd–Hf isotope space, the Amon kimberlites fall to either side of the terrestrial mantle regression line within the mantle array. Similar compositions have been observed for the Mesozoic Jericho kimberlites and their megacrysts from the Slave craton, which were interpreted as crystallization products of asthenosphere-derived melts (Kopylova *et al.*, 2009). In the absence of any isotopic excursions, such as anomalously low and high  $\Delta\epsilon_{\text{Hf}}$  values ( $-5 < \Delta\epsilon_{\text{Hf}} < +5$ ), it is most plausible that the bulk of the kimberlite magma that fed the Amon sills was derived from volatile-fluxed convecting upper mantle. However, we do not rule out minor contributions from the cratonic mantle in the form of melt from K–(P)-rich metasomes (e.g. low  $\epsilon_{\text{Hf}}$ ; Choukroun *et al.*, 2005), as well as assimilated garnets and pyroxenes (e.g. low and high  $\epsilon_{\text{Hf}}$ ; Schmidberger *et al.*, 2002; Klein-BenDavid & Pearson, 2009; Aulbach *et al.*, 2013). Also, the relatively wide vertical spread in Nd–Hf isotope space for the Amon sills (Fig. 15b) does not preclude entrainment of components from ultra-deep, long-term isolated mantle reservoirs such as the Transition Zone (Nowell *et al.*, 2004). However, current understanding of the Nd–Hf isotope systematics of kimberlite magmatic systems suggests that such ultra-deep components would

amount to  $\ll 5\%$  in the Amon example (see Tappe *et al.*, 2013a).

## TECTONIC SIGNIFICANCE

### Neoproterozoic kimberlite magmatism along Laurentia's rifted margins

The c. 673 Ma Amon kimberlites in north-central Baffin Island appear to mark the onset of Late Neoproterozoic kimberlite and related magmatism (680–540 Ma), which occurred along the northern and eastern breakout margins of Laurentia (i.e. present-day cratonic North America and Greenland) from the Rodinia supercontinent (Figs 1 and 2). Our new petrological and geochemical data, including Sr–Nd–Hf isotope compositions, indicate that the Amon kimberlite magmas were derived from the convecting upper mantle by low-degree partial melting of volatile-fluxed fertile peridotite. Importantly, the carbonate-rich and isotopically depleted component of the Amon kimberlite magmas has also been identified in other Late Neoproterozoic kimberlites and carbonatites along the rifted margins of Laurentia (Tappe *et al.*, 2011, and references therein). Although some workers have argued that Late Neoproterozoic rifting processes in eastern Laurentia were initiated by plume impingement (Puffer, 2002; Tachibana *et al.*, 2006; Ernst & Bell, 2010), we do not find compelling geological evidence for the activity of a plume, such as a directly associated LIP (see Chalapathi-Rao & Lehmann, 2011). The only indication of plume activity may be the mafic dyke swarm of the 723–712 Ma Franklin LIP (Pehrsson & Buchan, 1999; Denyszyn *et al.*, 2009) that occurs in the vicinity of the Amon kimberlites. However, the inferred plume center is situated on Victoria Island more than 1000 km to the NW of Baffin Island (Ernst & Bleeker, 2010), and potential plume impingement occurred more than 30 Myr prior to the Late Neoproterozoic kimberlite and related magmatism in eastern Laurentia.

On a global scale, the kimberlite magmatic gap between 1000 and 850 Ma is significant, and appears to correlate with the maximum stability of Rodinia (Fig. 1), which is inferred from various lines of independent geological evidence (Li *et al.*, 2008, and references therein). One of the most frequently invoked reasons for supercontinent break-up is the thermal insulation effect beneath a giant continental lithospheric plate, resulting in destabilization and the onset of rifting (Anderson, 1982; Lowman & Jarvis, 1999; Yoshida & Santosh, 2014). However, some numerical and laboratory experiments (Lenardic *et al.*, 2005; Coltice *et al.*, 2007; O'Neill *et al.*, 2009; Rolf *et al.*, 2012) suggest that mantle temperatures beneath supercontinents are elevated by only 25–100°C, much less than the frequently suggested 200°C (Gurnis, 1988). Furthermore, there is little evidence that mantle temperatures beneath continents increase as a function of areal extent (Lenardic, 1998), with



some newer simulations actually suggesting that temperatures beneath supercontinents >6000 km in size (e.g. reconstructed Rodinia at *c.* 900 Ma; Li *et al.*, 2008) drop to below the upper mantle average owing to the development of small-scale upper mantle convection cells that allow cooling of the underlying mantle (Solomatov & Moresi, 2000; Lenardic *et al.*, 2005; O'Neill *et al.*, 2009). Hence, as far as mantle temperature is concerned, there seems to be no reason why low-degree, volatile-rich, kimberlite melt could not be produced beneath thick cratonic nuclei that form part of a stable supercontinent assembly (Wyllie, 1980).

Our preferred model to explain Late Neoproterozoic kimberlite and related magmatism along the rifted margins of eastern Laurentia does not rely on temperature-induced melting, but rather on a redox melting mechanism (Foley, 1988; Taylor & Green, 1988). The lower reaches of cratonic lithosphere and the underlying uppermost convecting mantle are predicted to exhibit strong contrasts in redox state (Foley, 2008). The upper mantle below *c.* 300 km depth has been suggested to be metal-saturated (Rohrbach & Schmidt, 2011), which implies that carbonate-bearing melts do not readily migrate and are locally restricted phenomena (Stagno & Frost, 2010). However, the fluxing of C–H–O volatile-rich fluids from the lower upper mantle into the region between 300 km depth and a craton base at *c.* 200 km depth allows production of CO<sub>2</sub>- and H<sub>2</sub>O-rich fluids, primarily through the oxidation of CH<sub>4</sub>-rich fluids that enter into this boundary layer (Foley, 1988; Taylor & Green, 1988; Taylor *et al.*, 1994). Progressive conversion of reduced CH<sub>4</sub>-rich fluids into more oxidized CO<sub>2</sub>-rich fluids plus H<sub>2</sub>O profoundly affects the solidus temperature of peridotite, dropping it by >200°C (Taylor & Green, 1988; Foley, 2011; Litasov *et al.*, 2014). In other words, CO<sub>2</sub>- and H<sub>2</sub>O-charged convecting upper mantle material that flows to a large degree laterally (Yoshida & Santosh, 2014) beneath the rugged underside of a supercontinent may start to produce carbonated silicate melt by a combination of redox and decompression melting (Tappe *et al.*, 2012*b*). Most importantly, however, when the effects of redox melting are taken into consideration, no anomalous mantle temperatures are required to explain the presence of such 'proto-kimberlitic' melt beneath a thick cratonic lid.

We suggest that one of the most important requirements for kimberlitic melts to cause surface magmatism is the creation of pathways in the deeper cratonic mantle. Along channelled pathways [kimberlite dykes at mantle depth according to Grégoire *et al.* (2006)], assimilation reactions between invading carbonate-rich proto-kimberlitic melts and peridotitic pyroxenes and garnets, which are in disequilibrium with carbonate-rich melts, can be facilitated (Canil & Fedortchouk, 1999; Pilbeam *et al.*, 2013). Consequently, increased assimilation-fuelled buoyancy of

kimberlitic magmas may enhance their ascent (Russell *et al.*, 2012).

We argue here that critical pathways are opened not only during supercontinent break-up but also during assembly (Fig. 1), mainly as a response to changing plate motion velocities and vectors (England & Houseman, 1984; Jelsma *et al.*, 2009), which altogether put the cratonic nuclei under tensile stress (Gurnis, 1988). Arguably, lack of trans-lithospheric extension during maximum supercontinent stability may simply prevent ubiquitous carbonated silicate melts in the convecting upper mantle (potentially segregated into mantle mush melt pockets of several kilometres width; Grégoire *et al.*, 2006) from successfully penetrating cratonic lithosphere (see Wyllie, 1980), as indicated by the prominent kimberlite magmatic gaps during Rodinia's and Gondwana's prime (Fig. 1). Evidence for the presence of carbonate-bearing melts beneath cratonic lithosphere during periods of supercontinent stability comes from deeply derived mantle peridotite xenolith suites from all major cratons worldwide, and rare cratonic diamonds. The majority of the xenolith suites record interaction with carbonate-bearing melts (i.e. modal and/or cryptic metasomatism), and age constraints on the timing of metasomatism, as well as on diamond growth, include the periods of maximum tectonic stability (e.g. Simon *et al.*, 2007; Aulbach *et al.*, 2013; Smit *et al.*, 2014).

### Plate-tectonic origin for kimberlites within supercontinent cycles?

Compilation of comprehensive geochronology databases for kimberlite and related magmatism has shown an apparent episodicity of deep-seated melting processes (Jelsma *et al.*, 2004; Kumar *et al.*, 2007; Moore *et al.*, 2008), and it has been suggested that this magmatism is related to particular stages in the life cycle of supercontinents (Jelsma *et al.*, 2009). Jelsma *et al.* (2004) demonstrated that during the Phanerozoic narrow kimberlite emplacement windows correspond to periods of major plate reorganization that were associated with the assembly and break-up of the Gondwana supercontinent (see also Torsvik & Cocks, 2013). In this study, we argue that Proterozoic kimberlite and related magmatism was also a response to fundamental plate reorganization—in a very similar way to the Gondwana scenario. We demonstrate that the kimberlitic magmas that formed along the breakout margins of eastern Laurentia from the Rodinia supercontinent are best explained as low-degree partial melting products of CO<sub>2</sub>- and H<sub>2</sub>O-fluxed 'normal' fertile peridotite under convecting upper mantle conditions. Although it has been argued that supercontinents have a strong influence on deep mantle flow (Gurnis, 1988; Phillips & Bunge, 2007), there are detailed numerical modelling studies with Earth-like viscosity structures that indicate that the thermal state of the convecting upper mantle may be little affected by the 'stagnant lid effect' (Lenardic *et al.*, 2005;



O'Neill *et al.*, 2009; Rolf *et al.*, 2012). In other words, the thermal conditions beneath the thick stable continental lithosphere of a supercontinent are not hot enough to allow major melting, such as the generation of flood basalt magmas (O'Neill *et al.*, 2009). However, low-degree volatile-rich melts akin to proto-kimberlite and carbonatite magmas would almost certainly be permanently present beneath thick cratonic roots (Wyllie, 1980; Foley, 2008; Tappe *et al.*, 2012b), where they could pool into pockets of several kilometres width owing to mantle compaction processes (Grégoire *et al.*, 2006). Such small melt volumes can only be efficiently tapped when supercontinents are under tensile stress, which would be strongest during fast and changing plate motions that precede (i.e. assembly) and succeed (i.e. break-up) times of maximum supercontinent stability (Fig. 1). It follows that kimberlite and related magmatism appears to be more strongly controlled by plate-tectonic processes than the prominent magmatism that creates continental LIPs, which are generally believed to be a manifestation of strong mantle plumes that more randomly disrupt supercontinent cycles (Phillips & Bunge, 2007; Burke *et al.*, 2008).

Lastly, we speculate further back in time and evaluate the implications that low-volume kimberlitic and carbonatitic magmatism may have for the geodynamic processes that operated during the Archean. In our view, important prerequisites for kimberlite magmatism are the presence of thick lithosphere to suppress major melting, the abundant availability of C–H–O volatiles in oxidized speciation to allow melting at ambient mantle temperatures, and dynamic plate motions to create the pathways for low-volume melts to migrate to the Earth's surface. All these basic conditions were met since at least the Mesoarchean (Pearson, 1999; Shirey *et al.*, 2008; Foley, 2011), and it seems likely that the inception of low-volume, volatile-rich, mantle-derived magmatism is directly linked to the beginning of modern-style plate tectonics at *c.* 3.0–3.2 Ga (Shirey & Richardson, 2011; Dhuime *et al.*, 2012; Naeraa *et al.*, 2012). This inference is supported by the fact that detrital mantle-derived diamonds have been recovered from Late Archean sedimentary successions (Stachel *et al.*, 2006; Gurney *et al.*, 2010; Kopylova *et al.*, 2011), suggesting that kimberlitic magmatism *sensu lato* occurred as early as the Mesoarchean. As a corollary, the dearth of kimberlite and related rocks in the geological record between *c.* 3.0 and 2.0 Ga (Fig. 1) may be a strong function of preservation (Veizer *et al.*, 1992; Brown & Valentine, 2013). Alternatively, the apparent increase in the intensity of kimberlite magmatic episodes through time, with a global peak between *c.* 150 and 80 Ma, may reflect a combination of enhanced volatile cycling (Tappe *et al.*, 2013b), a continuously increasing upper mantle redox budget owing to net subduction addition of oxidizing species (Evans, 2012), and secular cooling of the Earth's mantle (Herzberg *et al.*, 2010).

## SUMMARY AND CONCLUSIONS

- (1) The newly discovered Amon kimberlites of north-central Baffin Island form a subhorizontal sill complex of Late Neoproterozoic age. The weighted average  $^{206}\text{Pb}/^{238}\text{U}$  rutile age of  $672.7 \pm 10.6$  Ma provides the current best estimate of kimberlite magma emplacement in the northern domain of the Rae craton in eastern Laurentia. The U–Pb rutile age is in good agreement with a  $^{40}\text{Ar}/^{39}\text{Ar}$  phlogopite age of  $660.1 \pm 8.6$  Ma that was determined for a kimberlite boulder from the area.
- (2) The petrography, mineralogy, and geochemistry of the Amon sills suggest that these rocks formed from bona fide Group-I kimberlite magma. However, appreciable magma differentiation occurred during sill emplacement, which created olivine-enriched portions at one end and highly carbonate-enriched portions at the other end of the observed compositional spectrum within the magmatic body. Some samples, however, appear to represent near-primary kimberlite magma compositions, and they resemble experimentally derived near-solidus partial melts of carbonated peridotite produced between 5 and 10 GPa (i.e. 150–300 km depths).
- (3) The Sr–Nd–Hf isotope compositions of the most pristine Amon kimberlite samples indicate magma derivation from a long-term depleted mantle reservoir, and in the absence of any significant isotopic anomalies it seems most plausible that the melt source region was located within the convecting upper mantle. The Amon kimberlite Nd–Hf isotope compositions closely match a hypothetical common carbonate-rich end-member component that has previously been identified in other Late Neoproterozoic kimberlites and carbonatites from eastern Laurentia.
- (4) Our preferred tectonomagmatic model for Late Neoproterozoic kimberlite and related magmatism along the rifted margins of Laurentia involves a combination of redox- and decompression-related low-degree partial melting of convecting upper mantle material that flows beneath the rugged underside of thick continental lithosphere. We argue that proto-kimberlitic melt is likely to be permanently present beneath the cratonic roots of supercontinents, but that it can be extracted only during fast and changing plate motions that occur during the assembly and break-up of supercontinents. This idea is supported by the known kimberlite emplacement patterns of the Gondwana–Pangea (510 Ma–Recent) and Rodinia (1300–550 Ma) supercontinent cycles, but it is difficult to test for older kimberlites and related rocks dating back to *c.* 3 Ga.

- (5) The episodicity of global kimberlite magmatism, and its clear relationship to the dynamic loops of super-continent cycles, suggests that kimberlites have a plate-tectonic origin and they do not require melting of anomalously hot, randomly upwelling mantle as advocated in plume scenarios. Whereas vast outpourings of continental and oceanic flood basalt magmas may signal the arrival of strong mantle plumes that are probably sourced from the core–mantle boundary, low-volume kimberlitic magmas provide a glimpse of the thermal and compositional state of the upper mantle beneath thick continental lithosphere.

## ACKNOWLEDGEMENTS

Julie Kong of De Beers Canada Inc. is gratefully acknowledged for her support and the permission to publish this study. We are grateful to Graham Pearson, Tony Simonetti, Sergei Matveev, Larry Heaman, Andy DuFrane, and Rob Creaser for their advice and support during the early stages of this project. Hielke Jelsma, Katie Smart, Andreas Stracke, Erik Scherer, Arno Rohrbach, and Khaled Ali are thanked for helpful discussions that ensued during preparation of the paper. Special thanks are given to Khaled Ali and Jason Adam, who prepared the map and the geological GOCAD<sup>TM</sup> model that are presented in Figs 3 and 4. We are indebted to Troels Nielsen, Sonja Aulbach, and Dejan Prelevic for their constructive criticism on this paper, as well as to Marjorie Wilson for consummate editorial handling.

## FUNDING

Sebastian Tappe acknowledges financial support from the Humboldt Foundation Feodor Lynen Scholarship Programme. Financial support for this study was received from the Gem Programme of the Geological Survey of Canada.

## SUPPLEMENTARY DATA

Supplementary data for this paper are available at *Journal of Petrology* online.

## REFERENCES

- Anderson, D. L. (1982). Hotspots, polar wander, Mesozoic convection and the geoid. *Nature* **297**, 391–393.
- Andronikov, A. V. & Foley, S. F. (2001). Trace element and Nd–Sr isotopic composition of ultramafic lamprophyres from the East Antarctic Beaver Lake area. *Chemical Geology* **175**, 291–305.
- Armstrong, J., Stubble, M. & Chang, F. (2008). Geology and exploration history of the Aviat kimberlite cluster, northern Rae craton, Melville Peninsula, Nunavut, Canada. In: *Extended Abstracts, 9th International Kimberlite Conference, 9IKC-A-00266*. Frankfurt, Germany.
- Arndt, N. (2003). Komatiites, kimberlites, and boninites. *Journal of Geophysical Research* **108**, 2293–2304.
- Aulbach, S., Stachel, T., Creaser, R. A., Heaman, L. M., Shirey, S. B., Muehlenbachs, K., Eichenberg, D. & Harris, J. W. (2009). Sulphide survival and diamond genesis during formation and evolution of Archaean subcontinental lithosphere: A comparison between the Slave and Kaapvaal cratons. *Lithos* **112**, 747–757.
- Aulbach, S., Griffin, W. L., Pearson, N. J. & O'Reilly, S. Y. (2013). Nature and timing of metasomatism in the stratified mantle lithosphere beneath the central Slave craton (Canada). *Chemical Geology* **352**, 153–169.
- Becker, M. & Le Roex, A. P. (2006). Geochemistry of South African on- and off-craton, Group I and Group II kimberlites: Petrogenesis and source region evolution. *Journal of Petrology* **47**, 673–703.
- Berman, R. G., Pehrsson, S., Davis, W. J., Ryan, J. J., Qui, H. & Ashton, K. E. (2013). The Arrowsmith orogeny: Geochronological and thermobarometric constraints on its extent and tectonic setting in the Rae craton, with implications for pre-Nuna supercontinent reconstruction. *Precambrian Research* **232**, 44–69.
- Beyer, C., Berndt, J., Tappe, S. & Klemme, S. (2013). Trace element partitioning between perovskite and kimberlite to carbonatite melt: New experimental constraints. *Chemical Geology* **353**, 132–139.
- Birkett, T. C., McCandless, T. E. & Hood, C. T. (2004). Petrology of the Renard igneous bodies: host rocks for diamond in the northern Otish Mountains region, Quebec. *Lithos* **76**, 475–490.
- Bizimis, M., Salters, V. J. M. & Dawson, J. B. (2003). The brevity of carbonatite sources in the mantle: Evidence from Hf isotopes. *Contributions to Mineralogy and Petrology* **145**, 281–300.
- Bizzarro, M., Simonetti, A., Stevenson, R. K. & David, J. (2002). Hf isotope evidence for a hidden mantle reservoir. *Geology* **30**, 771–774.
- Blichert-Toft, J., Chauvel, C. & Albarède, F. (1997). Separation of Hf and Lu for high-precision isotope analysis of rock samples by magnetic sector–multiple collector ICP-MS. *Contributions to Mineralogy and Petrology* **127**, 248–260.
- Bocor, N. Z. & Boyd, F. R. (1981). Oxide minerals in a layered kimberlite–carbonate sill from Benfontein, South Africa. *Contributions to Mineralogy and Petrology* **76**, 253–259.
- Bouvier, A., Vervoort, J. D. & Patchett, P. J. (2008). The Lu–Hf and Sm–Nd isotopic composition of CHUR: constraints from unequilibrated chondrites and implications for the bulk composition of terrestrial planets. *Earth and Planetary Science Letters* **273**, 48–57.
- Brey, G. P., Bulatov, V. K., Gurnis, A. V. & Lahaye, Y. (2008). Experimental melting of carbonated peridotite at 6–10 GPa. *Journal of Petrology* **49**, 797–821.
- Brooker, R. A. & Kjarsgaard, B. A. (2011). Silicate–carbonate liquid immiscibility and phase relations in the system SiO<sub>2</sub>–Na<sub>2</sub>O–Al<sub>2</sub>O<sub>3</sub>–CaO–CO<sub>2</sub> at 0.1 and 2.5 GPa with applications to carbonatite genesis. *Journal of Petrology* **52**, 1281–1305.
- Brown, R. J. & Valentine, G. A. (2013). Physical characteristics of kimberlite and basaltic intraplate volcanism and implications of a biased kimberlite record. *Geological Society of America Bulletin* **125**, 1224–1238.
- Burke, K., Steinberger, B., Torsvik, T. H. & Smethurst, M. A. (2008). Plume generation zones at the margins of large low shear velocity provinces on the core–mantle boundary. *Earth and Planetary Science Letters* **265**, 49–60.
- Canil, D. & Fedortchouk, Y. (1999). Garnet dissolution and the emplacement of kimberlites. *Earth and Planetary Science Letters* **167**, 227–237.
- Carlson, R. W., Czamanske, G., Fedorenko, V. & Ilupin, I. (2006). A comparison of Siberian meimechites and kimberlites: implications

- for the source of high-Mg alkalic magmas and flood basalts. *Geochemistry, Geophysics, Geosystems* **7**, Q11014.
- Chalapathi-Rao, N. V. & Lehmann, B. (2011). Kimberlites, flood basalts and mantle plumes: new insights from the Deccan large igneous province. *Earth-Science Reviews* **107**, 315–324.
- Chauvel, C., Lewin, E., Carpentier, M., Arndt, N. T. & Marini, J. C. (2008). Role of recycled oceanic basalt and sediment in generating the Hf–Nd mantle array. *Nature Geoscience* **1**, 64–67.
- Choukroun, M., O'Reilly, S. Y., Griffin, W. L., Pearson, N. J. & Dawson, J. B. (2005). Hf isotopes of MARID (mica–amphibole–rutile–ilmenite–diopside) rutile trace metasomatic processes in the lithospheric mantle. *Geology* **33**, 45–48.
- Clement, C. R. (1982). A comparative geological study of some major kimberlite pipes in the Northern Cape and Orange Free State. PhD thesis, University of Cape Town, 728 p.
- Clement, C. R., Skinner, E. M. W. & Scott Smith, B. H. (1984). Kimberlite redefined. *Journal of Geology* **92**, 223–228.
- Collerson, K. D., Williams, Q., Ewart, A. E. & Murphy, D. T. (2010). Origin of HIMU and EM-I domains sampled by ocean island basalts, kimberlites and carbonatites: The role of CO<sub>2</sub>-fluxed lower mantle melting in thermochemical upwellings. *Physics of the Earth and Planetary Interiors* **181**, 112–131.
- Coltice, N., Phillips, B. R., Bertrand, H., Ricard, Y. & Rey, P. (2007). Global warming of the mantle at the origin of flood basalts over supercontinents. *Geology* **35**, 391–394.
- Corrigan, D., Pehrsson, S., Wodicka, N. & de Kemp, E. (2009). The Palaeoproterozoic Trans-Hudson Orogen: a prototype of modern accretionary processes. In: Murphy, J. B., Keppie, J. D. & Hynes, A. J. (eds) *Ancient Orogens and Modern Analogues. Geological Society, London, Special Publications* **327**, 457–479.
- Cousens, B. L., Aspler, L. B., Chiarenzelli, J. R., Donaldson, J. A., Sandeman, H., Peterson, T. D. & LeCheminant, A. N. (2001). Enriched Archean lithospheric mantle beneath western Churchill Province tapped during Paleoproterozoic orogenesis. *Geology* **29**, 827–830.
- Crough, S. T., Morgan, W. J. & Hargraves, R. B. (1980). Kimberlites: their relation to mantle hotspots. *Earth and Planetary Science Letters* **50**, 260–274.
- Dasgupta, R., Hirschmann, M. M., McDonough, W. F., Spiegelman, M. & Withers, A. C. (2009). Trace element partitioning between garnet lherzolite and carbonatite at 6.6 and 8.6 GPa with applications to the geochemistry of the mantle and of mantle-derived melts. *Chemical Geology* **262**, 57–77.
- Davidson, A. (2008). Late Paleoproterozoic to mid-Neoproterozoic history of northern Laurentia: An overview of central Rodinia. *Precambrian Research* **160**, 5–22.
- Davis, W. J. (1997). U–Pb zircon and rutile ages from granulite xenoliths in the Slave province: evidence for mafic magmatism in the lower crust coincident with Proterozoic dike swarms. *Geology* **25**, 343–346.
- Dawson, J. B. & Hawthorne, J. B. (1973). Magmatic sedimentation and carbonatitic differentiation in kimberlite sills at Benfontein, South Africa. *Journal of the Geological Society, London* **129**, 61–85.
- Denyszyn, S. W., Halls, H. C., Davis, D. W. & Evans, D. A. D. (2009). Paleomagnetism and U–Pb geochronology of Franklin dykes in High Arctic Canada and Greenland: a revised age and paleomagnetic pole constraining block rotations in the Nares Strait region. *Canadian Journal of Earth Sciences* **46**, 689–705.
- Dhuime, B., Hawkesworth, C. J., Cawood, P. A. & Storey, C. D. (2012). A change in the geodynamics of continental growth 3 billion years ago. *Science* **335**, 1334–1336.
- England, P. & Houseman, G. (1984). On the geodynamic setting of kimberlite genesis. *Earth and Planetary Science Letters* **67**, 109–122.
- Ernst, R. E. & Bell, K. (2010). Large igneous provinces (LIPs) and carbonatites. *Mineralogy and Petrology* **98**, 55–76.
- Ernst, R. E. & Bleeker, W. (2010). Large igneous provinces (LIPs), giant dyke swarms, and mantle plumes: significance for breakup events within Canada and adjacent regions from 2.5 Ga to the Present. *Canadian Journal of Earth Sciences* **47**, 695–739.
- Ernst, R. E., Bleeker, W., Soderlund, U. & Kerr, A. C. (2013). Large Igneous Provinces and supercontinents: Toward completing the plate tectonic revolution. *Lithos* **174**, 1–14.
- Evans, D. A. D. & Mitchell, R. N. (2011). Assembly and breakup of the core of Paleoproterozoic–Mesoproterozoic supercontinent Nuna. *Geology* **39**, 443–446.
- Evans, K. A. (2012). The redox budget of subduction zones. *Earth-Science Reviews* **113**, 11–32.
- Foley, S. F. (1988). The genesis of continental basic alkaline magmas: an interpretation in terms of redox melting. *Journal of Petrology, Special Lithosphere Issue*, 139–161.
- Foley, S. F. (2008). Rejuvenation and erosion of the cratonic lithosphere. *Nature Geoscience* **1**, 503–510.
- Foley, S. F. (2011). A reappraisal of redox melting in the Earth's mantle as a function of tectonic setting and time. *Journal of Petrology* **52**, 1363–1391.
- Foley, S. F., Yaxley, G. M., Rosenthal, A., Buhre, S., Kiseeva, E. S., Rapp, R. P. & Jacob, D. E. (2009). The composition of near-solidus melts of peridotite in the presence of CO<sub>2</sub> and H<sub>2</sub>O between 40 and 60 kbar. *Lithos* **112**, 274–283.
- Frost, D. J. (2006). The stability of hydrous mantle phases. In: Keppler, H. & Smyth, J. R. (eds) *Water in Nominally Anhydrous Minerals. Mineralogical Society of America and Geochemical Society, Reviews in Mineralogy and Geochemistry* **62**, 243–271.
- Gaffney, A. M., Blichert-Toft, J., Nelson, B. K., Bizzarro, M., Rosing, M. & Albareda, F. (2007). Constraints on source-forming processes of West Greenland kimberlites inferred from Hf–Nd isotope systematics. *Geochimica et Cosmochimica Acta* **71**, 2820–2836.
- Gaspar, J. C. & Wyllie, P. J. (1984). The alleged kimberlite–carbonatite relationship: evidence from ilmenite and spinel from Premier and Wesselton mines and the Benfontein Sill, South Africa. *Contributions to Mineralogy and Petrology* **85**, 133–140.
- Gernon, T. M., Field, M. & Sparks, R. S. J. (2012). Geology of the Snap Lake kimberlite intrusion, Northwest Territories, Canada: Field observations and their interpretation. *Journal of the Geological Society, London* **169**, 1–16.
- Grégoire, M., Rabinowicz, M. & Janse, A. J. A. (2006). Mantle mush compaction: A key to understand the mechanisms of concentration of kimberlite melts and initiation of swarms of kimberlite dykes. *Journal of Petrology* **47**, 631–646.
- Gudfinnsson, G. H. & Presnall, D. C. (2005). Continuous gradations among primary carbonatitic, kimberlitic, melilititic, basaltic, picritic, and komatiitic melts in equilibrium with garnet lherzolite at 3–8 GPa. *Journal of Petrology* **46**, 1645–1659.
- Gurney, J. J., Helmstaedt, H. H., Richardson, S. H. & Shirey, S. B. (2010). Diamonds through time. *Economic Geology* **105**, 689–712.
- Gurnis, M. (1988). Large-scale mantle convection and the aggregation and dispersal of supercontinents. *Nature* **332**, 699–695.
- Harris, M., Le Roex, A. P. & Class, C. (2004). Geochemistry of the Uintjesberg kimberlite, South Africa: petrogenesis of an off-craton Group I kimberlite. *Lithos* **74**, 149–165.
- Heaman, L. M. & Kjarsgaard, B. A. (2000). Timing of eastern North American kimberlite magmatism: continental extension of the Great Meteor hotspot track? *Earth and Planetary Science Letters* **178**, 253–268.
- Heaman, L. M., Kjarsgaard, B. A. & Creaser, R. A. (2004). The temporal evolution of North American kimberlites. *Lithos* **76**, 377–397.

- Herzberg, C., Condie, K. & Korenaga, J. (2010). Thermal history of the Earth and its petrological expression. *Earth and Planetary Science Letters* **292**, 79–88.
- Hoffman, P. F. (1988). United plates of America, the birth of a craton: early Proterozoic assembly and growth of Laurentia. *Annual Review of Earth and Planetary Sciences* **16**, 543–603.
- Hofmann, A. W., Jochum, K. P., Seufert, M. & White, W. M. (1986). Nb and Pb in oceanic basalts: new constraints on mantle evolution. *Earth and Planetary Science Letters* **79**, 33–45.
- Irvine, G. J., Pearson, D. G., Kjarsgaard, B. A., Carlson, R. W., Kopylova, M. G. & Dreibus, G. (2003). A Re–Os isotope and PGE study of kimberlite-derived peridotite xenoliths from Somerset Island and a comparison to the Slave and Kaapvaal cratons. *Lithos* **71**, 461–488.
- Jelsma, H., Barnett, W., Richards, S. & Lister, G. (2009). Tectonic setting of kimberlites. *Lithos* **112**, 155–165.
- Jelsma, H. A., de Wit, M. J., Thiar, C., Dirks, P. H. G. M., Viola, G., Basson, I. J. & Anckar, E. (2004). Preferential distribution along transcontinental corridors of kimberlites and related rocks of Southern Africa. *South African Journal of Geology* **107**, 301–324.
- Johnson, C. M. & Beard, B. L. (1993). Evidence from hafnium isotopes for ancient sub-oceanic mantle beneath the Rio Grande rift. *Nature* **362**, 441–444.
- Kamenetsky, V. S., Kamenetsky, M. B., Sharygin, V. V., Faure, K. & Golovin, A. V. (2007). Chloride and carbonate immiscible liquids at the closure of the kimberlite magma evolution (Udachnaya-East kimberlite, Siberia). *Chemical Geology* **237**, 384–400.
- Khazan, Y. & Fialko, Y. (2005). Why do kimberlites from different provinces have similar trace element patterns? *Geochemistry, Geophysics, Geosystems* **6**, Q10002.
- Kjarsgaard, B. A. (2007). Kimberlite diamond deposits. In: Goodfellow, W. D. (ed.) *Mineral Deposits of Canada*. Geological Association of Canada, pp. 245–272.
- Kjarsgaard, B. A., Pearson, D. G., Tappe, S., Nowell, G. M. & Dowall, D. (2009). Geochemistry of hypabyssal kimberlites from Lac de Gras, Canada: comparisons to a global database and applications to the parent magma problem. *Lithos* **112**, 236–248.
- Klein-BenDavid, O. & Pearson, D. G. (2009). Origins of subcalic garnets and their relation to diamond forming fluids: Case studies from Ekati (NWT-Canada) and Murowa (Zimbabwe). *Geochimica et Cosmochimica Acta* **73**, 837–855.
- Klemme, S., Prowatke, S., Hametner, K. & Günther, D. (2005). Partitioning of trace elements between rutile and silicate melts: implications for subduction zones. *Geochimica et Cosmochimica Acta* **69**, 2361–2371.
- Konzett, J. (1997). Phase relations and chemistry of Ti-rich K-rich-ite-bearing mantle assemblages: an experimental study to 8.0 GPa in a Ti-KNCMASH system. *Contributions to Mineralogy and Petrology* **128**, 385–404.
- Konzett, J., Rhede, D. & Frost, D. J. (2012). The high *PT* stability of apatite and Cl partitioning between apatite and hydrous potassic phases in peridotite: an experimental study to 19 GPa with implications for the transport of P, Cl and K in the upper mantle. *Contributions to Mineralogy and Petrology* **163**, 277–296.
- Kopylova, M. G., Matveev, S. & Raudsepp, M. (2007). Searching for parental kimberlite melt. *Geochimica et Cosmochimica Acta* **71**, 3616–3629.
- Kopylova, M. G., Nowell, G. M., Pearson, D. G. & Markovic, G. (2009). Crystallization of megacrysts from protokimberlitic fluids: geochemical evidence from high-Cr megacrysts in the Jericho kimberlite. *Lithos* **112**, 284–295.
- Kopylova, M. G., Afanasiev, V. P., Bruce, L. F., Thurston, P. C. & Ryder, J. (2011). Metaconglomerate preserves evidence for kimberlite, diamondiferous root and medium grade terrane of a pre-2.7 Ga Southern Superior protocraton. *Earth and Planetary Science Letters* **312**, 213–225.
- Kretz, R. (1983). Symbols for rock-forming minerals. *American Mineralogist* **68**, 277–279.
- Kumar, A., Heaman, L. M. & Manikyamba, C. (2007). Mesoproterozoic kimberlites in south India: A possible link to 1.1 Ga global magmatism. *Precambrian Research* **154**, 192–204.
- Larsen, L. M. & Garrit, D. (2005). Mapping of the lithosphere beneath the Archaean craton and Proterozoic mobile belt in West Greenland. *Report—Geological Survey of Denmark and Greenland* **68**, 55–56.
- Larsen, L. M., Pedersen, A. K., Sundvoll, B. & Frei, R. (2003). Alkali picrites formed by melting of old metasomatized lithospheric mantle: Manitlat Member, Vaigat Formation, Palaeocene of West Greenland. *Journal of Petrology* **44**, 3–38.
- Le Roex, A. P. (1986). Geochemical correlation between southern African kimberlites and South Atlantic hotspots. *Nature* **324**, 243–245.
- Le Roex, A. P., Bell, D. R. & Davis, P. (2003). Petrogenesis of Group I kimberlites from Kimberley, South Africa: evidence from bulk-rock geochemistry. *Journal of Petrology* **44**, 2261–2286.
- Lenardic, A. (1998). On the partitioning of mantle heat loss below oceans and continents over time and its relationship to the Archaean paradox. *Geophysical Journal International* **134**, 706–720.
- Lenardic, A., Moresi, L. N., Jellinek, A. M. & Manga, M. (2005). Continental insulation, mantle cooling, and the surface area of oceans and continents. *Earth and Planetary Science Letters* **234**, 317–333.
- Li, Q. L., Li, S. G., Zheng, Y. F., Li, H. M., Massonne, H. J. & Wang, Q. C. (2003). A high-precision U–Pb age of metamorphic rutile in coesite-bearing eclogite from the Dabie Mountains in central China: A new constraint on the cooling history. *Chemical Geology* **200**, 255–265.
- Li, Z. X., Bogdanova, S. V., Collins, A. S., Davidson, A., De Waele, B., Ernst, R. E., Fitzsimons, I. C. W., Fuck, R. A., Gladkochub, D. P., Jacobs, J., Karlstrom, K. E., Lu, S., Natapov, L. M., Pease, V., Pisarevsky, S. A., Thrane, K. & Vernikovsky, V. (2008). Assembly, configuration, and break-up history of Rodinia: A synthesis. *Precambrian Research* **160**, 179–210.
- Litasov, K. D., Shatskiy, A. & Ohtani, E. (2014). Melting and subsolidus phase relations in peridotite and eclogite systems with reduced C–O–H fluid at 3–16 GPa. *Earth and Planetary Science Letters* **391**, 87–99.
- Lowman, J. P. & Jarvis, G. T. (1999). Effects of mantle heat source distribution on supercontinent stability. *Journal of Geophysical Research* **104**, 12733–12746.
- Ludwig, K. R. (2000). *Isoplot/Ex version 2.2. A geochronological toolkit for Microsoft Excel*. Berkeley Geochronology Center Special Publication **1a**.
- Lugmair, G. W. & Marti, K. (1978). Lunar initial  $^{143}\text{Nd}/^{144}\text{Nd}$ : differential evolution of the lunar crust and mantle. *Earth and Planetary Science Letters* **39**, 349–357.
- Malarkey, J., Pearson, D. G., Kjarsgaard, B. A., Davidson, J. P., Nowell, G. M., Ottley, C. J. & Stammer, J. (2010). From source to crust: tracing magmatic evolution in a kimberlite and a melilitite using microsample geochemistry. *Earth and Planetary Science Letters* **299**, 80–90.
- Marsh, J. S. (1973). Relationships between transform directions and alkaline igneous rock lineaments in Africa and South America. *Earth and Planetary Science Letters* **18**, 317–323.
- McKenzie, D. (1985). The extraction of magma from the crust and mantle. *Earth and Planetary Science Letters* **74**, 81–91.



- Mitchell, R. H. (1986). *Kimberlites: Mineralogy, Geochemistry and Petrology*. Plenum.
- Mitchell, R. H. (1995). *Kimberlites, Orangeites, and Related Rocks*. Plenum.
- Mitchell, R. H. & Chakhmouradian, A. R. (1998). Instability of perovskite in a CO<sub>2</sub>-rich environment: examples from carbonatite and kimberlite. *Canadian Mineralogist* **36**, 939–952.
- Moore, A., Blenkinsop, T. & Cotterill, F. (2008). Controls on post-Gondwana alkaline volcanism in Southern Africa. *Earth and Planetary Science Letters* **268**, 151–164.
- Naeraa, T., Schersten, A., Rosing, M. T., Kemp, A. I. S., Hoffmann, J. E., Kokfelt, T. F. & Whitehouse, M. J. (2012). Hafnium isotope evidence for a transition in the dynamics of continental growth 3.2 Gyr ago. *Nature* **485**, 627–631.
- Nielsen, T. F. D. & Sand, K. K. (2008). The Majuagaa kimberlite dike, Maniitsoq region, West Greenland: constraints on an Mg-rich silicocarbonatitic melt composition from groundmass mineralogy and bulk compositions. *Canadian Mineralogist* **46**, 1043–1061.
- Nielsen, T. F. D., Jensen, S. M., Secher, K. & Sand, K. K. (2009). Distribution of kimberlite and aillikite in the Diamond Province of southern West Greenland: a regional perspective based on groundmass mineral chemistry and bulk compositions. *Lithos* **112**, 358–371.
- Nowell, G. M., Pearson, D. G., Bell, D. R., Carlson, R. W., Smith, C. B., Kempton, P. D. & Noble, S. R. (2004). Hf isotope systematics of kimberlites and their megacrysts: New constraints on their source regions. *Journal of Petrology* **45**, 1583–1612.
- O'Neill, C., Lenardic, A., Jellinek, A. M. & Moresi, L. (2009). Influence of supercontinents on deep mantle flow. *Gondwana Research* **15**, 276–287.
- Palme, H. & O'Neill, H. S. C. (2003). Cosmochemical estimates of mantle composition. In: Carlson, R. W. (ed.) *Treatise on Geochemistry*. Elsevier, pp. 1–38.
- Paton, C., Hergt, J. M., Woodhead, J. D., Phillips, D. & Shee, S. R. (2009). Identifying the asthenospheric component of kimberlite magmas from the Dharwar craton, India. *Lithos* **112**, 296–310.
- Patterson, M., Francis, D. & McCandless, T. (2009). Kimberlites: magmas or mixtures? *Lithos* **112**, 191–200.
- Pearson, D. G. (1999). The age of continental roots. *Lithos* **48**, 71–194.
- Peats, J., Stachel, T., Stern, R. A., Muehlenbachs, K. & Armstrong, J. (2012). Aviat diamonds: A window into the deep lithospheric mantle beneath the northern Churchill Province, Melville Peninsula, Canada. *Canadian Mineralogist* **50**, 611–624.
- Pehrsson, S. J. & Buchan, K. L. (1999). Borden dykes of Baffin Island, Northwest Territories: a Franklin U–Pb baddeleyite age and a paleomagnetic reinterpretation. *Canadian Journal of Earth Sciences* **36**, 65–73.
- Pehrsson, S. J., Berman, R. G., Eglington, B. & Rainbird, R. (2013). Two Neoproterozoic supercontinents revisited: The case for a Rae family of cratons. *Precambrian Research* **232**, 27–43.
- Peterson, T. D. & LeCheminant, A. N. (1993). Glimmerite xenoliths in early Proterozoic ultrapotassic rocks from the Churchill Province. *Canadian Mineralogist* **31**, 801–819.
- Petts, D. C., Davis, W. J., Moser, D. E. & Longstaffe, F. J. (2014). Age and evolution of the lower crust beneath the western Churchill Province: U–Pb zircon geochronology of kimberlite-hosted granulite xenoliths, Nunavut, Canada. *Precambrian Research* **241**, 129–145.
- Phillips, B. R. & Bunge, H. P. (2007). Supercontinent cycles disrupted by strong mantle plumes. *Geology* **35**, 847–850.
- Phillips, D. & Harris, J. W. (2009). Diamond provenance studies from <sup>40</sup>Ar/<sup>39</sup>Ar dating of clinopyroxene inclusions: An example from the west coast of Namibia. *Lithos* **112**, 793–805.
- Pilbeam, L. H., Nielsen, T. F. D. & Waight, T. E. (2013). Digestion fractional crystallization (DFC): An important process in the genesis of kimberlites. Evidence from olivine in the Majuagaa kimberlite, southern West Greenland. *Journal of Petrology* **54**, 1399–1425.
- Prelevic, D., Foley, S. F., Romer, R. L. & Conticelli, S. (2008). Mediterranean Tertiary lamproites derived from multiple source components in postcollisional geodynamics. *Geochimica et Cosmochimica Acta* **72**, 2125–2156.
- Prelevic, D., Stracke, A., Foley, S. F., Romer, R. L. & Conticelli, S. (2010). Hf isotope compositions of Mediterranean lamproites: Mixing of melts from asthenosphere and crustally contaminated mantle lithosphere. *Lithos* **119**, 297–312.
- Puffer, J. H. (2002). A late Neoproterozoic eastern Laurentian superplume: location, size, chemical composition, and environmental impact. *American Journal of Science* **302**, 1–27.
- Rainbird, R. H., Davis, W. J., Pehrsson, S. J., Wodicka, N., Rayner, N. & Skulski, T. (2010). Early Paleoproterozoic supracrustal assemblages of the Rae domain, Nunavut, Canada: Intracratonic basin development during supercontinent break-up and assembly. *Precambrian Research* **181**, 167–186.
- Renne, P. R., Swisher, C. C., Deino, A. L., Karner, D. B., Owens, T. L. & DePaolo, D. J. (1998). Intercalibration of standards, absolute ages and uncertainties in <sup>40</sup>Ar–<sup>39</sup>Ar dating. *Chemical Geology* **145**, 117–152.
- Renne, P. R., Mundil, R., Balco, G., Min, K. W. & Ludwig, K. R. (2010). Joint determination of <sup>40</sup>K decay constants and <sup>40</sup>Ar/<sup>40</sup>K for the Fish Canyon sanidine standard, and improved accuracy for <sup>40</sup>Ar/<sup>39</sup>Ar geochronology. *Geochimica et Cosmochimica Acta* **74**, 5349–5367.
- Renne, P. R., Balco, G., Ludwig, K. R., Mundil, R. & Min, K. (2011). Response to the comment by W. H. Schwarz *et al.* on 'Joint determination of <sup>40</sup>K decay constants and <sup>40</sup>Ar/<sup>40</sup>K for the Fish Canyon sanidine standard, and improved accuracy for <sup>40</sup>Ar/<sup>39</sup>Ar geochronology' by P. R. Renne *et al.* (2010). *Geochimica et Cosmochimica Acta* **75**, 5097–5100.
- Roberts, N. M. W. (2013). The boring billion? Lid tectonics, continental growth and environmental change associated with the Columbia supercontinent. *Geoscience Frontiers* **4**, 681–691.
- Roeder, P. L. & Schulze, D. J. (2008). Crystallization of groundmass spinel in kimberlite. *Journal of Petrology* **49**, 1473–1495.
- Rohrbach, A. & Schmidt, M. W. (2011). Redox freezing and melting in the Earth's deep mantle resulting from carbon–iron redox coupling. *Nature* **472**, 209–212.
- Rolf, T., Coltice, N. & Tackley, P. J. (2012). Linking continental drift, plate tectonics and the thermal state of the Earth's mantle. *Earth and Planetary Science Letters* **351**, 134–146.
- Russell, J. K., Porritt, L. A., Lavalley, Y. & Dingwell, D. B. (2012). Kimberlite ascent by assimilation-fuelled buoyancy. *Nature* **481**, 352–357.
- Scherer, E., Münker, C. & Mezger, K. (2001). Calibration of the lutetium–hafnium clock. *Science* **293**, 683–687.
- Schmidberger, S. S., Simonetti, A., Francis, D. & Gariépy, C. (2002). Probing Archean lithosphere using the Lu–Hf isotope systematics of peridotite xenoliths from Somerset Island kimberlites, Canada. *Earth and Planetary Science Letters* **197**, 245–259.
- Schmidberger, S. S., Simonetti, A., Heaman, L. M., Creaser, R. A. & Whiteford, S. (2007). Lu–Hf, *in-situ* Sr and Pb isotope and trace element systematics for mantle eclogites from the Diavik diamond mine: Evidence for Paleoproterozoic subduction beneath the Slave craton, Canada. *Earth and Planetary Science Letters* **254**, 55–68.
- Shirey, S. B. & Richardson, S. H. (2011). Start of the Wilson Cycle at 3 Ga shown by diamonds from subcontinental mantle. *Science* **333**, 434–436.
- Shirey, S. B., Kamber, B. S., Whitehouse, M. J., Mueller, P. A. & Basu, A. R. (2008). A review of the isotopic and trace element

- evidence for mantle and crustal processes in the Hadean and Archean: Implications for the onset of plate tectonic subduction. In: Condie, K. C. & Pease, V. (eds) *When Did Plate Tectonics Begin on Planet Earth? Geological Society of America, Special Papers* **440**, 1–29.
- Simon, N. S. C., Carlson, R. W., Pearson, D. G. & Davies, G. R. (2007). The origin and evolution of the Kaapvaal cratonic lithospheric mantle. *Journal of Petrology* **48**, 589–625.
- Smit, K. V., Stachel, T. & Stern, R. A. (2014). Diamonds in the Attawapiskat area of the Superior craton (Canada): Evidence for a major diamond-forming event younger than 1.1 Ga. *Contributions to Mineralogy and Petrology* **167**, 962–978.
- Smith, C. B. (1983). Pb, Sr and Nd isotopic evidence for sources of southern African Cretaceous kimberlites. *Nature* **304**, 51–54.
- Smith, C. B., Gurney, J. J., Skinner, E. M. W., Clement, C. R. & Ebrahim, N. (1985). Geochemical character of Southern African kimberlites: A new approach based on isotopic constraints. *Transactions of the Geological Society of South Africa* **88**, 267–280.
- Snyder, D. B. & Grütter, H. S. (2010). Lithoprobe's impact on the Canadian diamond-exploration industry. *Canadian Journal of Earth Sciences* **47**, 783–800.
- Snyder, D. B., Berman, R. G., Kendall, J. M. & Sanborn-Barrie, M. (2013). Seismic anisotropy and mantle structure of the Rae craton, central Canada, from joint interpretation of SKS splitting and receiver functions. *Precambrian Research* **232**, 189–208.
- Solomatov, V. S. & Moresi, L. N. (2000). Scaling of time-dependent stagnant lid convection: Application to small-scale convection on Earth and other terrestrial planets. *Journal of Geophysical Research* **105**, 21795–21817.
- St-Onge, M. R., van Gool, J. A. M., Garde, A. A. & Scott, D. J. (2009). Correlation of Archaean and Palaeoproterozoic units between northeastern Canada and western Greenland: constraining the pre-collisional upper plate accretionary history of the Trans-Hudson Orogen. In: Cawood, P. A. & Kröner, A. (eds) *Earth Accretionary Systems in Space and Time. Geological Society, London, Special Publications* **318**, 193–235.
- Stacey, J. S. & Kramers, J. D. (1975). Approximation of terrestrial lead isotope evolution by a two-stage model. *Earth and Planetary Science Letters* **26**, 207–221.
- Stachel, T., Banas, A., Muehlenbachs, K., Kurszlaukis, S. & Walker, E. C. (2006). Archean diamonds from Wawa (Canada): samples from deep cratonic roots predating cratonization of the Superior Province. *Contributions to Mineralogy and Petrology* **151**, 737–750.
- Stagno, V. & Frost, D. J. (2010). Carbon speciation in the asthenosphere: Experimental measurements of the redox conditions at which carbonate-bearing melts coexist with graphite or diamond in peridotite assemblages. *Earth and Planetary Science Letters* **300**, 72–84.
- Steiger, R. H. & Jäger, E. (1977). Subcommittee on geochronology: convention on the use of decay constants in geo- and cosmochemistry. *Earth and Planetary Science Letters* **36**, 359–362.
- Tachibana, Y., Kaneoka, I., Gaffney, A. & Upton, B. G. J. (2006). Ocean-island basalt-like source of kimberlite magmas from West Greenland revealed by high  $^3\text{He}/^4\text{He}$  ratios. *Geology* **34**, 273–276.
- Tanaka, T., Togashi, S., Kamioka, H., Amakawa, H., Kagami, H., Hamamoto, T., Yuhara, M., Orihashi, Y., Yoneda, S., Shimizu, H., Kunimaru, T., Takahashi, K., Yanagi, T., Nakano, T., Fujimaki, H., Shinjo, R., Asahara, Y., Tanimizu, M. & Dragusanu, C. (2000). JNdi-1: a neodymium isotopic reference in consistency with La Jolla neodymium. *Chemical Geology* **168**, 279–281.
- Tappe, S. & Simonetti, A. (2012). Combined U–Pb geochronology and Sr–Nd isotope analysis of the Ice River perovskite standard, with implications for kimberlite and alkaline rock petrogenesis. *Chemical Geology* **304–305**, 10–17.
- Tappe, S., Jenner, G. A., Foley, S. F., Heaman, L. M., Besserer, D., Kjarsgaard, B. A. & Ryan, B. (2004). Torngat ultramafic lamprophyres and their relation to the North Atlantic Alkaline Province. *Lithos* **76**, 491–518.
- Tappe, S., Foley, S. F., Jenner, G. A. & Kjarsgaard, B. A. (2005). Integrating ultramafic lamprophyres into the IUGS classification of igneous rocks: rationale and implications. *Journal of Petrology* **46**, 1893–1900.
- Tappe, S., Foley, S. F., Jenner, G. A., Heaman, L. M., Kjarsgaard, B. A., Romer, R. L., Stracke, A., Joyce, N. & Hoefs, J. (2006). Genesis of ultramafic lamprophyres and carbonatites at Aillik Bay, Labrador: a consequence of incipient lithospheric thinning beneath the North Atlantic craton. *Journal of Petrology* **47**, 1261–1315.
- Tappe, S., Foley, S. F., Stracke, A., Romer, R. L., Kjarsgaard, B. A., Heaman, L. M. & Joyce, N. (2007). Craton reactivation on the Labrador Sea margins:  $^{40}\text{Ar}/^{39}\text{Ar}$  age and Sr–Nd–Hf–Pb isotope constraints from alkaline and carbonatite intrusives. *Earth and Planetary Science Letters* **256**, 433–454.
- Tappe, S., Foley, S. F., Kjarsgaard, B. A., Romer, R. L., Heaman, L. M., Stracke, A. & Jenner, G. A. (2008). Between carbonatite and lamproite—diamondiferous Torngat ultramafic lamprophyres formed by carbonate-fluxed melting of cratonic MARID-type metasomes. *Geochimica et Cosmochimica Acta* **72**, 3258–3286.
- Tappe, S., Steinfeld, A., Heaman, L. M. & Simonetti, A. (2009). The newly discovered Jurassic Tikiusaaq carbonatite–aillikite occurrence, West Greenland, and some remarks on carbonatite–kimberlite relationships. *Lithos* **112**, 385–399.
- Tappe, S., Pearson, D. G., Nowell, G. M., Nielsen, T. F. D., Milstead, P. & Muehlenbachs, K. (2011). A fresh isotopic look at Greenland kimberlites: cratonic mantle lithosphere imprint on deep source signal. *Earth and Planetary Science Letters* **305**, 235–248.
- Tappe, S., Nowell, G. M., Kurszlaukis, S. & Kjarsgaard, B. A. (2012a). Large igneous provinces and kimberlites? Origin of the diamondiferous Amon kimberlites, Baffin Island, Arctic Canada. In: *Extended Abstracts, 10th International Kimberlite Conference, 10IKC-A-0047. Bangalore, India.*
- Tappe, S., Steinfeld, A. & Nielsen, T. F. N. (2012b). Asthenospheric source of Neoproterozoic and Mesozoic kimberlites from the North Atlantic craton, West Greenland: new high-precision U–Pb and Sr–Nd isotope data on perovskite. *Chemical Geology* **320–321**, 113–127.
- Tappe, S., Pearson, D. G., Kjarsgaard, B. A., Nowell, G. M. & Dowall, D. (2013a). Mantle transition zone input to kimberlite magmatism near a subduction zone: Origin of anomalous Nd–Hf isotope systematics at Lac de Gras, Canada. *Earth and Planetary Science Letters* **371–372**, 235–251.
- Tappe, S., Pearson, D. G. & Prelevic, D. (2013b). Kimberlite, carbonatite, and potassic magmatism as part of the geochemical cycle. *Chemical Geology* **353**, 1–3.
- Taylor, W. R. & Green, D. H. (1988). Measurement of reduced peridotite–C–O–H solidus and implications for redox melting of the mantle. *Nature* **332**, 349–352.
- Taylor, W. R., Tompkins, L. A. & Haggerty, S. E. (1994). Comparative geochemistry of West African kimberlites: evidence for a micaceous kimberlite endmember of sublithospheric origin. *Geochimica et Cosmochimica Acta* **58**, 4017–4037.
- Thirlwall, M. F. (1991). Long-term reproducibility of multicollector Sr and Nd isotope ratio analysis. *Chemical Geology* **94**, 85–104.
- Torsvik, T. H. (2003). The Rodinia jigsaw puzzle. *Science* **300**, 1379–1381.

- Torsvik, T. H. & Cocks, L. R. M. (2013). Gondwana from top to base in space and time. *Gondwana Research* **24**, 999–1030.
- Torsvik, T. H., Burke, K., Steinberger, B., Webb, S. J. & Ashwal, L. D. (2010). Diamonds sampled by plumes from the core–mantle boundary. *Nature* **466**, 352–355.
- Veizer, J., Bell, K. & Jansen, S. L. (1992). Temporal distribution of carbonatites. *Geology* **20**, 1147–1149.
- Wittig, N., Webb, M., Pearson, D. G., Dale, C. W., Ottley, C. J., Hutchison, M., Jensen, S. M. & Luguët, A. (2010). Formation of the North Atlantic craton: timing and mechanisms constrained from Re–Os isotope and PGE data of peridotite xenoliths from SW Greenland. *Chemical Geology* **276**, 166–187.
- Woodhead, J., Hergt, J., Phillips, D. & Paton, C. (2009). African kimberlites revisited: *In situ* Sr-isotope analysis of groundmass perovskite. *Lithos* **112**, 311–317.
- Wu, F. Y., Yang, Y. H., Mitchell, R. H., Li, Q. L., Yang, J. H. & Zhang, Y. B. (2010). *In situ* U–Pb age determination and Nd isotopic analysis of perovskites from kimberlites in southern Africa and Somerset Island, Canada. *Lithos* **115**, 205–222.
- Wyatt, B. A., Baumgartner, M., Anckar, E. & Grütter, H. S. (2004). Compositional classification of ‘kimberlitic’ and ‘non-kimberlitic’ ilmenite. *Lithos* **77**, 819–840.
- Wyllie, P. J. (1980). The origin of kimberlite. *Journal of Geophysical Research* **85**, 6902–6910.
- Yang, Y. H., Wu, F. Y., Wilde, S. A., Liu, X. M., Zhang, Y. B., Xie, L. W. & Yang, J. H. (2009). *In situ* perovskite Sr–Nd isotopic constraints on the petrogenesis of the Ordovician Mengyin kimberlites in the North China Craton. *Chemical Geology* **264**, 24–42.
- Yaxley, G. M., Kamenetsky, V. S., Nichols, G. T., Maas, R., Belousova, E., Rosenthal, A. & Norman, M. (2013). The discovery of kimberlites in Antarctica extends the vast Gondwanan Cretaceous province. *Nature Communications* **4**, 1–7.
- Yoshida, M. & Santosh, M. (2014). Mantle convection modeling of the supercontinent cycle: Introversion, extroversion, or a combination? *Geoscience Frontiers* **5**, 77–81.
- Zack, T., Stockli, D. F., Luvizotto, G. L., Barth, M. G., Belousova, E., Wolfe, M. R. & Hinton, R. W. (2011). *In situ* U–Pb rutile dating by LA-ICP-MS: <sup>208</sup>Pb correction and prospects for geological applications. *Contributions to Mineralogy and Petrology* **162**, 515–530.
- Zurevinski, S. E. & Mitchell, R. H. (2011). Highly evolved hypabyssal kimberlite sills from Wemindji, Quebec, Canada: insights into the process of flow differentiation in kimberlite magmas. *Contributions to Mineralogy and Petrology* **161**, 765–776.